MECHANICAL CONSTRAINTS ON THE STRENGTH OF THE LITHOSPHERE AND PLATE-BOUNDING FAULTS

A DISSERTATION
SUBMITTED TO THE DEPARTMENT OF GEOPHYSICS
AND THE COMMITTEE ON GRADUATE STUDIES
OF STANFORD UNIVERSITY
IN PARTIAL FULFILLMENT OF THE REQUIREMENTS
FOR THE DEGREE OF
DOCTOR OF PHILOSOPHY

John Townend
January 2003

I certify that I have read this dissertation and that, in my opinion, it is fully adequate in scope and quality as a dissertation for the degree of Doctor of Philosophy.

Mark D. Zoback
(Principal Adviser)

I certify that I have read this dissertation and that, in my opinion, it is fully adequate in scope and quality as a dissertation for the degree of Doctor of Philosophy.

Gregory C. Beroza

I certify that I have read this dissertation and that, in my opinion, it is fully adequate in scope and quality as a dissertation for the degree of Doctor of Philosophy.

Paul Segall

Approved for the University Committee on Graduate Studies:

Abstract

This thesis addresses the state of stress in continental lithosphere, the mechanisms by which it is maintained, and its implications for the mechanical behavior of plate-bounding faults and the accommodation of tectonic deformation.

Measured stress magnitudes in intraplate brittle crust are consistent with the Coulomb frictional-failure criterion and coefficients of friction similar to those determined in laboratory experiments, implying that the upper crust is in a state of frictional equilibrium. If the lower portions of the lithosphere deform ductilely, then the lithosphere as a whole is in a state of failure and its strength must equal the magnitude of any applied tectonic forces. We use this inference to consider the vertical distribution of lithospheric strength and the bounds this places on intraplate strain rates.

Using earthquake focal mechanism stress inversions, we have mapped the horizontal stress field in central and southern California and verified previous suggestions that the San Andreas fault (SAF) slips in response to lower levels of shear stress than anticipated on the basis of the intraplate or laboratory observations. By comparing the stress results with geodetic data and dynamic modeling results, we further show that while crustal velocities adjacent to the SAF are consistent with localized plate kinematics, crustal stresses seem to be controlled by relatively far-field processes.

Finally, by amalgamating data from three independent seismographic networks, we have produced an improved Japanese focal mechanism catalog with which to investigate the stresses associated with subduction and crustal collision. The axis of maximum horizontal compressive stress in central and southwestern Japan is found to be approximately parallel to the axis of maximum contractional strain rate once deformation associated with an elastic model of subduction thrust locking has been subtracted from the original strain

rate observations. This suggests that the state of stress in the Japanese arc is related more to long-term relative plate motions than to interseismic strain accumulation and seismogenic release on the subduction thrusts.

Acknowledgments

It has been a privilege to study under the supervision of Prof. Mark Zoback, whose knowledge of geophysics and enthusiasm for science and scientific pizzazz are exemplary. Thank you very much, Mark, for providing such a stimulating and friendly environment in which to work, and for taking such a keen interest in what your graduate students are doing.

I have greatly appreciated Prof. George Thompson's ongoing support and interest in my work, and the thought-provoking comments of the members of my advisory committee, Assoc. Prof. Greg Beroza, Prof. Paul Segall, and Dr. Wayne Thatcher. I am grateful to Prof. Amos Nur for stimulating discussions and for kindly inviting me to take part in consecutive "Earthquakes and Archeology" field trips to Israel and Jordan, and Mexico. I also thank the benefactors of the Stanford Graduate Fellowship and the Lieberman Fellowship for their generous commitment to graduate education.

Lourdes Colmenares, Sigurjón Jónsson, Björn and Lena Lund, Jessica Murray, and Stephanie Prejean are the sorts of colleagues, Stefan Harmeling and Luis Sentis the sorts of flatmates, and *all* of them the sorts of friends that make a place like this so rewarding. Teresa and Jörn; your friendship during the last four years has been wonderful, and I am glad to have shared so many experiences. Thank you for the companionship, the tea, coffee and red wine, and for all our adventures. Erica, thanks for making the last few months so sunny.

Finally, I think that a lot of what scientists enjoy doing is trying to find (or make up) exactly the right expression to describe things: thanks Mum and Dad, Thomas, Andrew, and Oliver for your encouragement and for helping me play around with words.

Contents

List of Tables

List of Figures

Chapter 1

Introduction

There's a fraction too much friction

Tim Finn

FRACTION TOO MUCH FRICTION

1.1 Overview and Aims

In recent years, dramatic improvements in geodetic measurement techniques have produced an abundance of data illustrating the lithosphere's kinematic behavior at various length and time scales. The corresponding *kinetics* of the lithosphere — the sources and actions of forces acting on the plates — have received somewhat less attention, perhaps because of the relative difficulty in quantifying tectonic stresses. Nevertheless, what evidence exists strongly suggests that both the magnitudes (McGarr and Gay, 1978; Zoback and Harjes, 1997) and orientations (Zoback and Healy, 1984; Zoback et al., 1987; Zoback and Zoback, 1991; Zoback, 1992) of stresses within the earth exhibit highly coherent spatial patterns (Figure 1.1) that can, in principle, be related to fundamental tectonic driving mechanisms (Forsyth and Uyeda, 1975; Fleitout and Froidevaux, 1982; Turcotte and Schubert, 1982; Bott and Kusznir, 1984; Kusznir, 1991; Jones et al., 1996).

The ascendency of plate tectonic theory since the 1960s has led to an overwhelming focus on the interactions between plates at their mutual boundaries — where most of the geologic action is taking place — at the expense of the plates' interiors. It is important, however, in the context of understanding the lithosphere's mechanical configuration in general and this thesis in particular to consider both the intrinsic strength of the plates themselves and the strength of the boundaries they share. Consequently, the approach taken here is to first investigate separately the stress fields in intraplate and plate boundary regions, and to then use the former to interpret the latter in light of several motivating questions:

1. What is the state of tectonic stress in intraplate lithosphere, and how is it maintained? (Chapters 2–3)

2. What does the tectonic stress field look like in central and southern California, how reliable is our image, and what role does the San Andreas fault play in modulating the stress field? (Chapter 4)

3. How can intraplate and plate boundary stress observations be linked? Alternatively, where does "intraplate" end and "plate boundary" begin? (Chapter 5)

4. What do subduction zone and upper plate stress orientations in Japan imply about the frictional characteristics of subduction thrusts, and the overall mechanism of stress transmission across a tectonically complex plate boundary? (Chapter 6)

First, I demonstrate the applicability of simple empirical relationships (Coulomb frictional faulting theory and Byerlee's law) to intraplate stress magnitude data and the compatibility of these relationships with observations of crustal permeability and internal deformation of the lithosphere. This establishes a conceptual model of the mechanism by which the lithosphere maintains its strength in response to applied forces.

Second, I describe the construction of a detailed image of the tectonic stress field adjacent to an archetypal plate boundary, namely the San Andreas fault system. The stress orientation data obtained in this phase of the work indicate that at least some, and perhaps all, major plate-bounding faults are weak in both an absolute sense (slipping in response to levels of shear traction of $\sim$10–20 MPa) and the obvious relative sense (being necessarily weaker than the crust in which they are embedded).

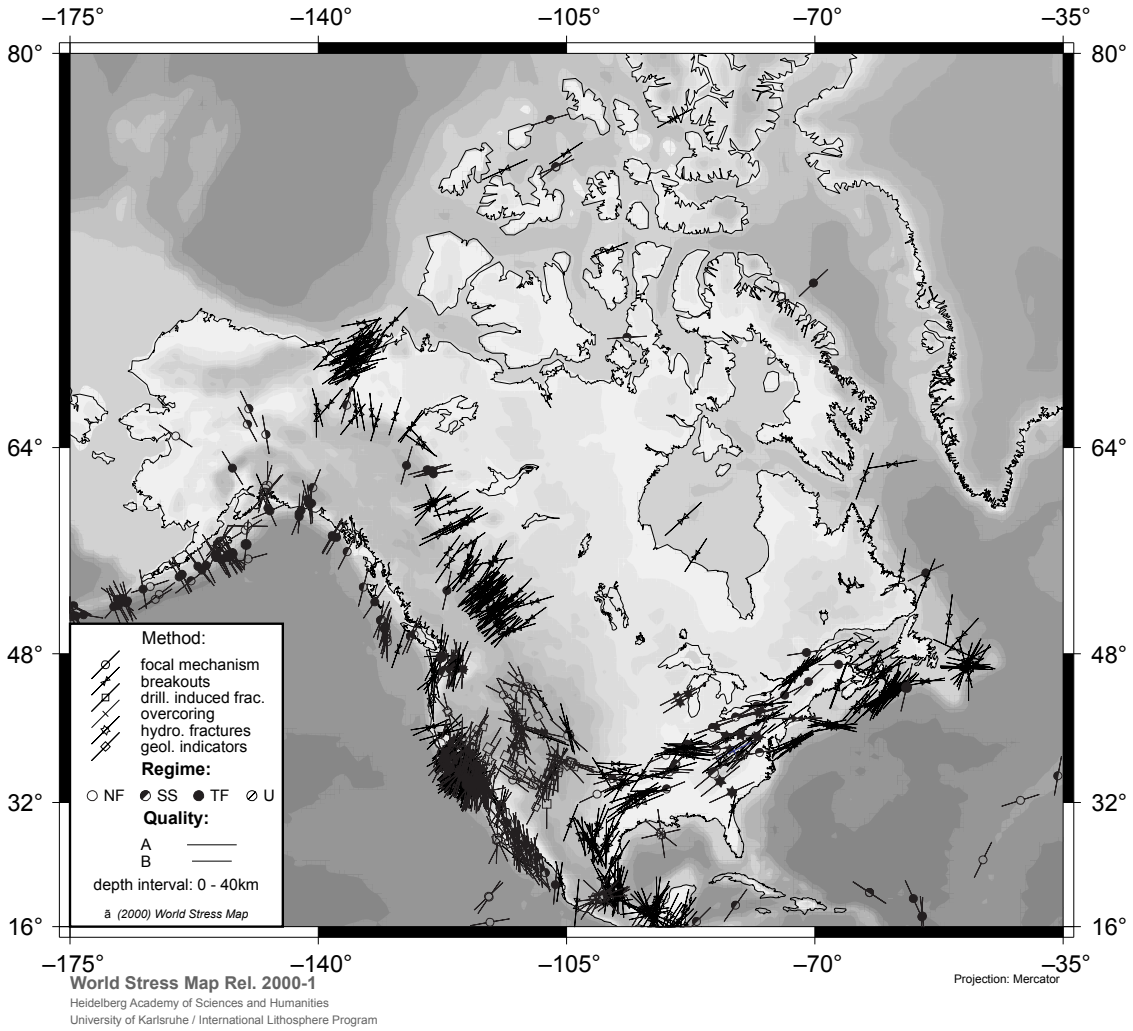

Figure 1.1: Maximum horizontal compressive stress directions in North America, demonstrating the coherent spatial patterns characteristic of the tectonic stress field. These data are from the World Stress Map database, maintained by the Heidelberg Academy of Sciences.

The third step is to interpret the plate boundary stress orientation data in terms of likely sources of tectonic stress. Specifically, the observed stress field in central and southern California can be compared with the results of dynamical modeling to try to distinguish a component of the tectonic stress field associated with the existence of the San Andreas fault from those related to longer wavelength lithospheric buoyancy and distributed intraplate

deformation. I then consider whether the model of intraplate lithospheric strength can be used to address strain localization in an active plate boundary zone in terms of lateral heat flow variations.

Finally, I turn to a geometrically and tectonically more complicated region, Japan, and consider whether the general approach used to interpret the mechanics of a transpressive strike-slip plate boundary can be useful in analyzing patterns of stress and strain localization in a subduction setting.

1.2 Thesis Outline

In addition to this Introduction, this thesis contains five self-contained but complementary chapters that are intended to constitute a heuristic sequence of steps in terms of understanding lithospheric and plate boundary mechanics. Chapters 2, 3, and 4 have each been published in their entirety, and Chapter 5 contains some material that has been published as part of a separate paper. Each chapter addresses a distinct component of the research, and effort has been made to avoid unnecessary duplication; there nevertheless remains a minor and unavoidable amount of overlap between certain sections.

1.2.1 How Faulting Keeps the Crust Strong

In Chapter 2 we demonstrate that critically stressed faults maintain high crustal permeability, near-hydrostatic pore pressures, and high crustal strength. Several lines of evidence suggest that intraplate crust is generally in a state of frictional failure equilibrium, or yield, in which differential stresses are maintained at values equivalent to the frictional strength of the rock. This state of stress is analogous to that existing in a pile of sand. The shape of the pile is maintained by a dynamic equilibrium at the angle of repose, which is a direct function of the sand's frictional characteristics. The corresponding state of stress within the sand pile is "critical" in the sense that it is controlled by a myriad of frictional contacts between sand grains that are incipiently failing. The empirical relationship underlying this

behavior, and in fact the bulk of this thesis, is the Coulomb frictional failure criterion

$$\tau = \mu(S_n - P_f) \tag{1.1}$$

which relates the shear (τ) and normal (S_n) tractions acting on a potential failure surface via the coefficient of friction (μ) and the ambient fluid pressure (P_f).

As far as Chapter 2 is concerned, the key term in equation 1.1 is $-P_f$: for a given normal traction, the higher the fluid pressure, the lower the shear traction a potential failure surface can sustain before failing. Data from several deep boreholes reveal that differential stress increases with depth at a rate highly consistent with that expected for critically stressed faults, that fluid pressures are hydrostatic, and that it is the critically stressed faults that maintain the low fluid pressures. The tongue-in-cheek chapter title, "How faulting keeps the crust strong", alludes to the fact that the low fluid pressures enable critically stressed faults to support higher shear tractions and therefore differential stresses than would be the case if critically stressed fractures did not provide high hydraulic conductivity and fluid pressures were correspondingly higher.

1.2.2 Lithospheric Failure Equilibrium and Intraplate Deformation

Chapter 3 outlines the implications of frictional failure equilibrium in the brittle crust for the strength of the lithosphere as a whole. The frictional behavior of the upper crust is expected to yield to a ductile, temperature-dependent mode of deformation at a depth within the crust below which ductile flow takes place at lower differential stresses than required to deform rock brittley. Experimental results suggest that the constitutive relation describing the rheology of the lower crust and mantle is a power-law relationship between strain rate ($\dot{\varepsilon}$) and differential stress (ΔS) of the form

$$\dot{\varepsilon} \propto \Delta S^n \tag{1.2}$$

where n is a positive number. This relationship implies that rock will flow in response to any differential stress, although perhaps at negligibly small strain rates. While ostensibly rigid on everyday time scales, intraplate lithosphere is nevertheless observed to deform at

nonzero strain rates. Short-term observations using very long baseline interferometry, as well as extremely long-term estimates provided by the observed similarities of the coastlines of Africa and South America, for example, both provide an upper bound on intraplate strain rates of $\sim 10^{-17}$ s^{-1}.

Hence, both the brittle and ductile regimes of the lithosphere are in a state of failure. Given, however, that the lithosphere supports the loads imposed on it by various plate tectonic processes, its strength must be equal to the magnitude of those loads. In the absence of basal tractions, the lithosphere's total strength (S_L) is equal to the integral over the thickness of the lithosphere (D) of the differential stress, or

$$S_L = \int_0^D \Delta S dz \tag{1.3}$$

We can use this result as constraint on valid lithospheric strength envelopes, namely that the integral of the differential stress–depth profile is finite and known to be approximately 3×10^{12} N m^{-1}. With this approach, we have investigated the mechanical significance of the brittle crust in terms of the lithosphere's total strength. In contrast to the negligible brittle strength often assumed in thin viscous sheet models of continental deformation, we find that the brittle crust — by means of the mechanisms described in Chapter 2 — provides about half the total strength of intraplate lithosphere in other than extremely low heat flow regions.

1.2.3 Tectonic Stress Orientations in Southern California

In contrast to the previous two chapters, which addressed crustal mechanics in intraplate regions in terms of the magnitudes of the principal stresses, Chapter 3 focuses on the principal stresses' orientations in the vicinity of an active plate boundary. California has been the vanguard of seismology and tectonophysics since the 1906 San Francisco earthquake, and the San Andreas fault in particular has received more geophysical attention than perhaps any other geological structure on Earth. Ironically, however, while the mechanics of small intraplate faults are reasonably well understood (as discussed in Chapter 2), those of the intensively studied San Andreas remain enigmatic. Specifically, two lines of evidence suggest that the San Andreas fault is much weaker than either laboratory friction

data or intraplate stress data imply. First, heat flow data from throughout California fail to reveal a thermal anomaly of the magnitude expected for a high-friction fault slipping at the observed rate of 2–3 cm yr^{-1}; on the contrary, the heat flow data suggest that the fault's frictional resistance is 20–25% that expected on the basis of typical frictional coefficients. Second, the SAF appears to slip in response to very low driving stresses, as indicated by the uniformly high angle ($>60^\circ$, and locally $>80^\circ$) between the axis of greatest horizontal stress and the San Andreas fault plane.

Prompted by a recent paper (Hardebeck and Hauksson, 1999) that suggested that the horizontal stress field rotates within 20 km of the San Andreas fault in southern California to angles consistent with a stronger fault than previously thought, we computed stress orientations throughout the region based on a recursive spatial gridding of focal mechanism data. This approach provides a high resolution image of stress orientations in areas of dense seismicity, and a correspondingly low resolution image where focal mechanisms are sparse. Our results confirm those of most earlier workers, and substantiated the heat flow data, in indicating that the San Andreas fault slips in response to low levels of shear traction.

1.2.4 Crustal Dynamics of the San Andreas Fault System

In Chapter 5 we investigate the state of stress in central and southern California based on a detailed comparison of the results from Chapter 4 with independently obtained borehole data, stress directions calculated using a dynamical model of the lithosphere, and the geodetically determined crustal velocity field. The focal mechanism stress inversion results, borehole data, and calculated stress fields exhibit a remarkably similar NNE–SSW regional orientation of the axis of maximum horizontal compression, S_{Hmax}, and suggest that the orientation of the regional stress field is primarily controlled by long-wavelength lithospheric buoyancy and far-field interplate tractions. Close to the San Andreas fault, however, S_{Hmax} is consistently oriented at a much higher angle to the fault than expected on the basis of Byerlee friction ($68\pm7^\circ$ in southern California, and as much as 85° in central California), irrespective of variations in the fault's strike. This suggests that the geometry of the stress field is *locally* controlled by the geometry of the San Andreas fault, despite

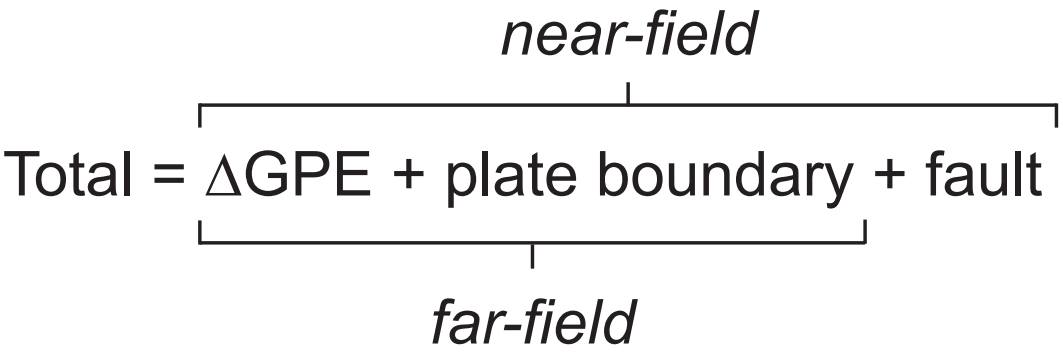

Figure 1.2: Components of the tectonic stress field. This schematic figure illustrates the hypothesis that the stress field adjacent to the San Andreas contains a near-field component related to the presence of the fault itself, superimposed upon the more regional gravitational potential energy (lithospheric buoyancy) and plate boundary components. By comparing near- and far-field estimates of the stress field, the effect of this fault-related component may be detectable (see Chapter 5).

its low frictional strength. We can therefore consider the stress field in the plate boundary zone to comprise three components (Figure 1.2), two of which are represented throughout the area, but the third of which is limited to the immediate vicinity of the San Andreas fault.

Applying the conceptual model of the entire lithosphere being in a state of dynamic failure described in Chapter 3 to central California enables us to consider the question of what mechanism controls the localization of strain within a relatively uniform and transpressive stress field. In the context of this "force-limited plate tectonic" framework, we propose that the focussing of relative plate motion onto the San Andreas fault system in central California is a consequence of higher heat flow in the Coast Ranges than in the adjacent Central Valley. In these terms, the localization of strain reflects the modulation of a uniform stress field by a laterally varying thermal structure.

1.2.5 The Contemporary Tectonic Stress Field in Japan

If the San Andreas fault is the world's most intensively studied strike-slip plate boundary, then its unequivocal dip-slip counterpart is the Nankai Trough. In Chapter 6 we describe the state of horizontal stress throughout Japan based on inversion of a newly acquired focal

mechanism data set. This data set has been constructed by merging the phase data (P and S arrival times, and P polarities) recorded by three independent monitoring networks. We demonstrate that this results in a much larger data set than provided by any single network alone with equal or better hypocenter and focal mechanism qualities.

We have obtained preliminary results illustrating the state of tectonic stress throughout Japan, and in central and southwestern Japan in particular. As in California, the existence of high-quality geodetic data enables us to address the source of the observed stress field. In this case, similarities between the axis of greatest horizontal compressive stress and the axis of greatest contractional strain rate once the effects of interseismic subduction thrust locking have been removed from the observed deformation field suggest that the stress field in central and southwestern Japan is associated primarily with deformation accompanying crustal collision in the upper plate rather than with transient locking and release of the subduction thrusts.

1.3 Summary and Outlook

The questions motivating this thesis and its layout can be paraphrased as “What do plate interiors look like, what do plate boundaries look like, and how are the two related?”. To this, we have provided the following contributions:

1. A self-consistent mechanical explanation of high crustal strength (the “critically stressed crust”)

    (a) Verification of the general applicability of Byerlee’s law to intraplate faulting

    (b) Elaboration of the role played by critically stressed faults in maintaining high crustal permeability

2. A heuristic explanation of the mechanism by which the strength of tectonic plates is maintained (“force-limited plate tectonics”)

    (a) Demonstration of the importance of the brittle crust in providing lithospheric strength

   (b) Explanation of observed intraplate strain rates in terms of the requirements of force-limited strength profiles

3. A better understanding of the state of crustal stress in southern and central California, and its relationship to far-field tectonic forces and the frictional characteristics of the San Andreas fault system

   (a) Reevaluation of the state of stress in southern California

   (b) Verification of the regional validity of a dynamical model of tectonic stress

   (c) Demonstration of the weakness of the San Andreas fault

4. An integrated seismicity and focal mechanism data set for Japan, and a preliminary estimate of the state of tectonic stress throughout the region

   (a) Compilation of three seismicity catalogs into a single consolidated data set

   (b) Construction of a nationwide horizontal stress map

   (c) Calculation of stress orientations in the Nankai Trough and Japan Trench subduction zones

   (d) Comparison of upper plate stress orientations with the geodetically estimated deformation field

A promising area for future research is the comparison of crustal stress data with geodetic and geological estimates of strain and relative plate motions. As described in Chapters 5 and 6, the abundance of high-quality geodetic data in California and Japan has proven useful for interpreting stress orientations and enabled us to evaluate the stress field's characteristics in terms of specific tectonic processes. In California, a comparison of crustal velocity and stress orientation data reveals that strain may be highly localized within a relatively uniform tectonic stress field. In contrast, comparing stress and apparent inelastic strain rate data in central Japan reveals that horizontal stresses in the upper plate likely reflect the collision of the Amurian plate with northeast Honshu, rather than strain accumulation and release on the subduction thrust. Further comparisons of crustal stress and deformation data in these locations and elsewhere (such as Taiwan or New Zealand) are

likely to provide useful insight into the mechanisms by which far-field relative plate motions are locally accommodated within plate boundary regions.

Chapter 2

How Faulting Keeps the Crust Strong[1]

2.1 Abstract

Deep drilling and induced seismicity experiments at several locations worldwide indicate that, in general, the brittle crust in intraplate regions is critically stressed, pore pressures are close to hydrostatic, and in situ bulk permeability is $\sim 10^{-17}$ to 10^{-16} m^2. This high permeability, three or four orders of magnitude higher than that measured on core samples, appears to be maintained by critically stressed faults and greatly facilitates fluid movement through the brittle crust. We demonstrate that such high permeabilities can maintain approximately hydrostatic fluid pressures at depths comparable to the thickness of the seismogenic crust. This leads to the counterintuitive result that faulting keeps intraplate crust inherently strong by preventing pore pressures greater than hydrostatic from persisting at depth.

2.2 Introduction

Three independent lines of evidence indicate that intraplate continental crust is in a state of failure equilibrium: (1) the widespread occurrence of seismicity induced by either reservoir impoundment (Simpson et al., 1988; Roeloffs, 1996) or fluid injection (Raleigh et al., 1972; Pine et al., 1983; Zoback and Harjes, 1997), (2) earthquakes triggered by other earthquakes

[1] Previously published by Townend and Zoback (2000).

(Stein et al., 1992, 1997), and (3) in situ stress measurements in deep wells and boreholes (Zoback and Healy, 1992; Brudy et al., 1997). The in situ stress measurements further show that Coulomb frictional-failure theory incorporating laboratory-derived frictional coefficients, μ, of 0.6–1.0 (Byerlee, 1978) gives predictions that are consistent with measured stress states in the upper crust. For instance, at virtually all locations where deep stress levels have been measured, the ratio of the maximum differential stress, ΔS, to the effective mean stress, $\bar{S} - P_f$ (where $\bar{S}$ is the mean stress and P_f is the pore pressure), agrees well with that predicted using Coulomb frictional-failure theory, namely

$$\frac{\Delta S}{S - P_f} = \frac{2\mu}{\sqrt{\mu^2 + 1}} \tag{2.1}$$

This is illustrated in Figure 2.1; it can be clearly seen that at each of the six locations illustrated, the effective stress data are consistent with values of μ between approximately 0.6 and 1.0. These data support the hypothesis that the crust contains critically stressed faults that limit its strength.

However, because the frictional strength of a faulted rock mass depends on pore pressure (Hubbert and Rubey, 1959), estimates of the frictional strength of the brittle crust depend on the pore pressure at depth (Sibson, 1974; Brace and Kohlstedt, 1980). In particular, combining Coulomb faulting theory with laboratory-derived coefficients of friction leads to the conclusion that the crust's brittle strength is quite high (hundreds of megapascals) under conditions of hydrostatic pore pressure.

2.3 Crustal Permeability and its Scale Dependence

The high permeability of upper crustal crystalline rocks was first noted by Brace (1980), who observed that, even given the relatively limited number of permeability measurements available at the time, the crust was unlikely to be able to sustain pore pressures much greater than hydrostatic. Recently acquired in situ permeability data support this observation, and furthermore suggest a gross scale-dependence in which permeability increases with increasing scale (Clauser, 1991). This relationship is particularly well illustrated by

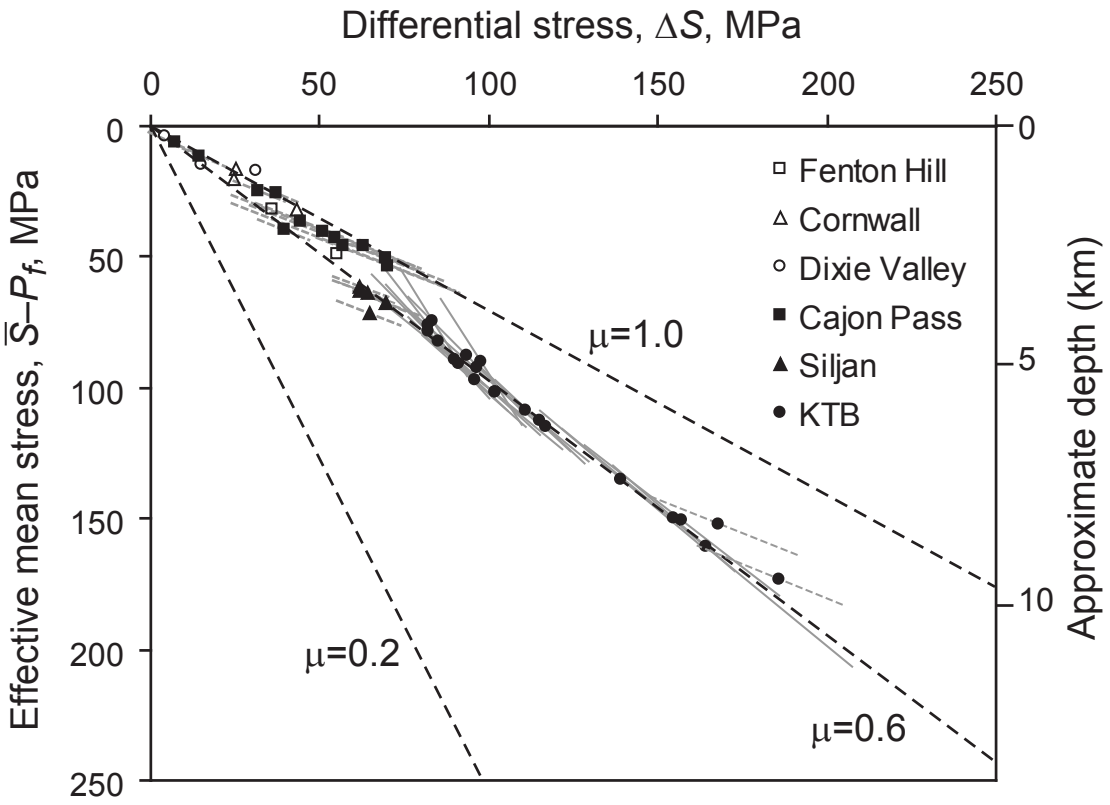

Figure 2.1: Differential (ΔS) and effective mean stress ($\bar{S}$) data from six locations at which deep stress measurements have been made. The dashed grey uncertainties are based on a single S_3 value and two corresponding S_1 values and the solid grey uncertainties on two separate pairs (minimum and maximum) of S_1 and S_3 values; see the Appendix for details. The dashed black lines illustrate the relationships predicted using Coulomb frictional-failure theory for various coefficients of friction, μ. References: Fenton Hill, Barton et al. (1988); Cornwall, Pine et al. (1983) and Batchelor and Pine (1986); Dixie Valley, Hickman et al. (1997); Cajon Pass, Zoback and Healy (1992); Siljan, Lund and Zoback (1999); KTB, Brudy et al. (1997).

hydraulic tests made in the German Continental Deep Drilling Program (KTB; Kontinentales Tiefbohrprogramm der Bundesrepublik Deutschland) pilot and main holes at depths as great as 9.1 km (Huenges et al., 1997, Figure 2.2). During these tests, an interval of the borehole was mechanically isolated, and fluid was pumped into it. The test intervals used for these experiments varied between a few tens of meters and almost 3.5 km, providing estimates of the gross vertical permeability of kilometer-scale sections of the upper crust.

Data from the most reliable experiments — 7 low-volume buildup drill stem tests and 12 open-hole buildup tests — indicated permeabilities of between 10^{-20} and $>10^{-16}$ m^2: the majority of the most reliable measurements consistently gave permeabilities of $>10^{-17}$ m^2. In comparison, laboratory measurements made under estimated in situ pressure and temperature conditions on centimeter-scale core samples obtained in the 0–7.5 km depth range indicated permeability of between 10^{-20} and 10^{-18} m^2 (Huenges et al., 1997). A three to four order of magnitude discrepancy existed therefore between the large-scale and small-scale permeabilities of rocks tested under approximately the same effective confining pressures (Figure 2.2).

At the same location, Shapiro et al. (1997) concluded that progressive hypocentral migration over distances of >1 km during an induced seismicity experiment performed at the bottom of the KTB main hole (Zoback and Harjes, 1997) indicated bulk permeability of $\sim 10^{-17}$ to 10^{-16} m^2. Analogous experiments at the Fenton Hill (Nevada), Soultz (Alsace, France), and Hijori (Yamagata, Japan) hot dry rock sites gave similar permeabilities of 10^{-17} to 10^{-16} m^2 at depths of 3.0–3.9 km, 2.8–3.4 km, and 1.7–1.9 km, respectively (Shapiro et al., 1999; Sasaki, 1998). Slightly higher permeabilities (10^{-16} to 10^{-15} m^2) were estimated from hydraulic tests and induced seismicity diffusion at the Monticello Reservoir, South Carolina, at very shallow depths (<1 km; Zoback and Hickman, 1982).

A similar result was obtained in experiments made at the Cajon Pass borehole in southern California. Morrow and Byerlee (1988, 1992) obtained permeabilities of 10^{-22} to 10^{-19} m^2 from core samples retrieved from 0.5 to 2.1 km depth (which also exhibited a systematic one order of magnitude decrease per kilometer) whereas Coyle and Zoback (1988) measured a permeability of $\sim 10^{-18}$ m^2 over 100 m and 300 m hydraulic test intervals.

Core measurements at in situ confining pressures (for hydrostatic fluid pressures) on samples from the 12-km-deep Kola Peninsula superdeep well consistently show extremely low permeability values of less than 10^{-20} m^2 (Lockner et al., 1991; Morrow et al., 1994). Unfortunately, hydraulic testing was not performed on the Kola borehole, so no large-scale permeability data were obtained directly. However, thermal models of borehole temperature data constrain the kilometer-scale permeability of the 0–2 km and 6–8 km intervals to 10^{-14} m^2 and 10^{-17} m^2, respectively (Kukkonen and Clauser, 1994).

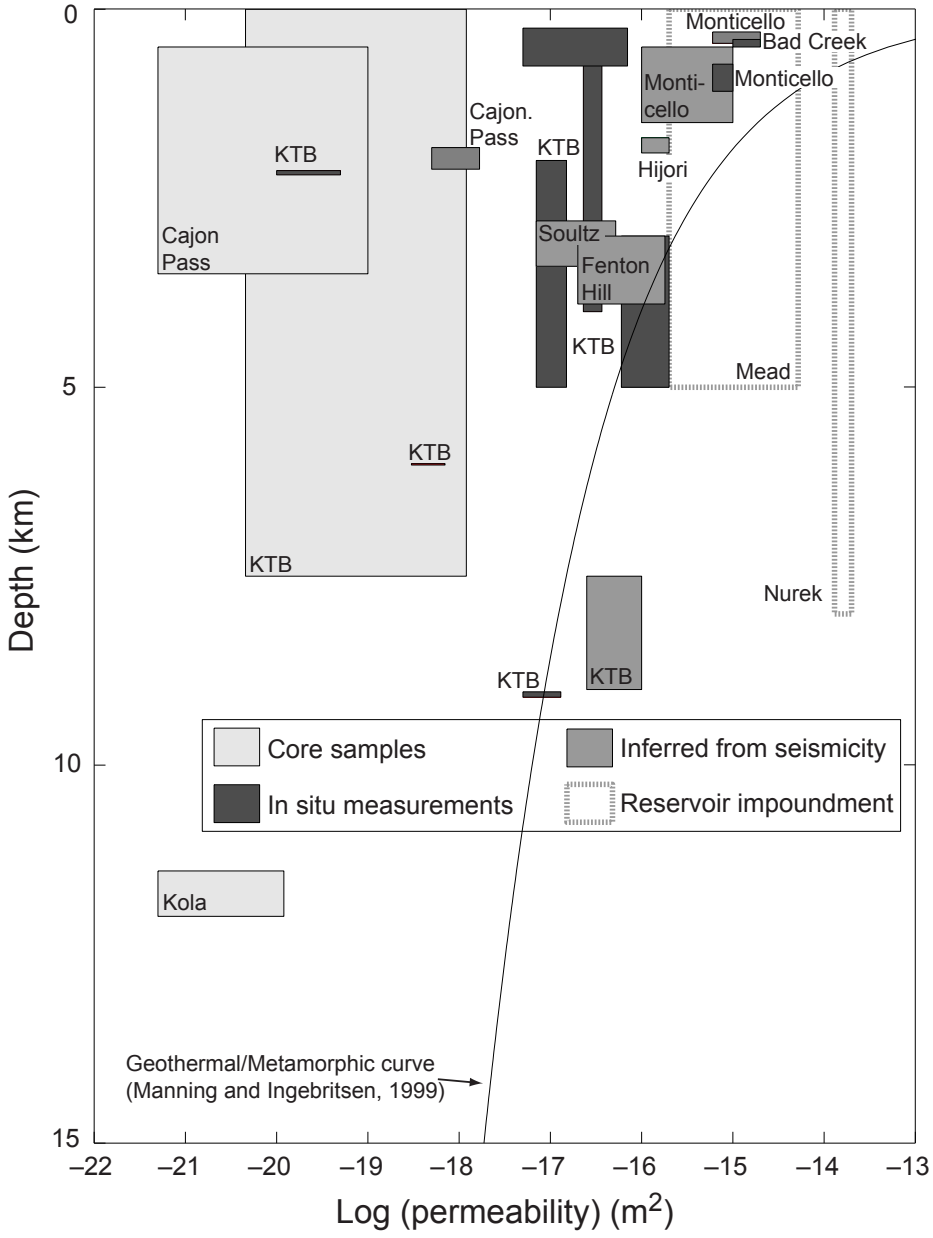

Figure 2.2: Deep crustal permeability data acquired from core samples, in situ hydraulic tests, and induced seismicity. References: core samples, Huenges et al. (1997), Lockner et al. (1991), Morrow and Byerlee (1988), Morrow and Byerlee (1992), and Morrow et al. (1994); in situ measurements, Coyle and Zoback (1988) and Huenges et al. (1997); seismicity data, Sasaki (1998), Shapiro et al. (1997), Shapiro et al. (1999), and Zoback and Hickman (1982); reservoir impoundment data, Roeloffs (1988) and Talwani et al. (1999); geothermal/metamorphic curve, Manning and Ingebritsen (1999).

Reservoir impoundment provides another means of inducing seismicity and has been used by several authors to estimate kilometer-scale permeability. Roeloffs (1988) used seismicity occurring beneath the Mead (Arizona–Nevada) and Nurek (Tadjikistan) Reservoirs following peak impoundment to estimate hydraulic diffusivity. When transformed into equivalent permeabilities, Roeloffs' data suggest permeabilities of 10^{-16} to 10^{-15} m^2 between 0 and 5 km beneath the Mead Reservoir and $\sim 10^{-14}$ m^2 between the surface and 8 km beneath the Nurek Reservoir. Both these results are an order of magnitude higher than those obtained from direct fluid-injection results. The hydraulic response of a 250 m-long shear zone to fluctuations in reservoir level at the Bad Creek Reservoir (South Carolina) was used by Talwani et al. (1999) to calculate permeability, giving a result of 10^{-15} m^2.

Manning and Ingebritsen (1999) recently compiled and interpreted geothermal and metamorphic data to provide crustal permeability estimates at depths greater than observable in boreholes (>10 km). The permeability threshold above which fluid advection transports heat more effectively than conduction appears to be approximately 10^{-16} m^2, whereas the corresponding threshold for advective solute transport is only 10^{-20} m^2. Similarly, time-integrated fluid fluxes during metamorphism — manifested geochemically, petrologically, and isotopically in both metamorphic protoliths and the associated fluids — indicate permeabilities during regional metamorphism of 10^{-19} to 10^{-18} m^2. Manning and Ingebritsen (1999) also demonstrated that crustal permeability (k) obeys a power-law decrease with depth (z) according to the relationship (Figure 2.2)

$$\log k = -3.2 \log z - 14 \tag{2.2}$$

where k and z are measured in meters squared (m^2) and kilometers, respectively.

Figure 2.2 clearly illustrates that with the exception of laboratory measurements on cores, different methods of estimating in situ permeability give relatively consistent results. Core measurements, even when made under in situ pressure and temperature conditions, give very low permeabilities that vary substantially owing to local heterogeneities. Consequently, although the core measurements determine the intrinsic permeability of the rock

mass, they are not indicative of the effective permeability controlling large-scale upper-crust hydraulics. In contrast, borehole measurements and experimentally and reservoir-induced seismicity at a number of locations give almost uniformly high permeabilities of $>10^{-17}$ m^2. Furthermore, these permeabilities agree extremely well with independent estimates based on geochemical and geothermal considerations. We conclude that the permeability of the upper crust is $\sim 10^{-17}$ to 10^{-16} m^2 over 1 to 10 km scales.

2.4 Deep Crustal Pore Pressure and Stress Measurements

Fluid pressures at depths of several kilometers have been measured using several independent techniques in deep boreholes drilled into crystalline basement and have been consistently found to be approximately hydrostatic. Table 2.1 lists the deepest of these boreholes, in each of which fluid pressures were unequivocally near-hydrostatic. Stress magnitudes at each of these locations (except the Kola borehole, where stress measurements were not performed) are consistent with Coulomb frictional-failure theory for coefficients of friction of 0.6–1.0 such as are measured experimentally in laboratory settings (Byerlee, 1978; Brace and Kohlstedt, 1980, Figure 2.1), and seismicity was induced by fluid injection at a number of these sites.

By using borehole televiewer images and high-resolution temperature logs from the Cajon Pass, Long Valley (California) and Yucca Mountain USW-G1 (Nevada) boreholes, Barton et al. (1995) showed that critically stressed faults — that is, faults with ratios of resolved shear to normal tractions of 0.6–1.0 — are hydraulically conductive, whereas those that are not critically stressed are not hydraulically conductive. Figure 2.3 presents these data in a somewhat different form from that shown by Barton et al. (1995), and it is clear that the hydraulically conductive fractures are critically stressed according to the Coulomb frictional-failure criterion. Hickman et al. (1997) and Barton et al. (1998) subsequently obtained similar results in the Dixie Valley geothermal field adjacent to the Stillwater fault, a range-bounding normal fault in the Basin and Range province, Nevada, on which **M** 7.3 and **M** 6.8 earthquakes occurred in 1915 and 1954, respectively. In this case too, the critically stressed fractures, including the Stillwater fault, were found to be hydraulically conductive, whereas the non-critically stressed faults and fractures were not. Ito and Zoback

Well location	Depth (km)	Observation	Stress regime & Critical Stress
Cornwall HDR, England	2.5	DST	SS; stress magnitudes, induced seismicity
Fenton Hill HDR, New Mexico	3.0	SWC	N/SS; stress magnitudes
Dixie Valley, Nevada	2–3 5–7	DST, SG	N; stress magnitudes, prehistoric fault offsets
Cajon Pass, California	3.5	DST	SS; stress magnitudes, breakout rotations
Soultz HDR, France	5.0	DST	N/SS; stress magnitudes, induced seismicity
Siljan, Sweden	7.0	DST	SS; stress magnitudes
KTB, Germany	9.1	DST, SWC	SS; stress magnitudes, induced seismicity
Kola, Russia	12.2	SWC	?R; N.A.

Table 2.1: Locations exhibiting near-hydrostatic fluid pressures at depths of several kilometers. HDR — hot dry rock; DST — drill stem test; SWC — static water column; SG — silica geothermometry; N — normal stress regime; R — reverse stress regime; SS — strike-slip stress regime; N.A. — not available. Sources: Cornwall, Pine et al. (1983); Fenton Hill, Barton et al. (1988); Dixie Valley, Hickman et al. (1997); Cajon Pass, Coyle and Zoback (1988); Soultz, Baumgärtner et al. (1998); Siljan, Lund and Zoback (1999); KTB, Huenges et al. (1997) and Zoback and Harjes (1997); Kola, Borevsky et al. (1987).

(2000) have reported similar results using data from the KTB main borehole.

It seems clear from all of these in situ studies that, in general, the crust is in frictional failure equilibrium (even in relatively stable intraplate areas), near-hydrostatic pore pressures exist to great depth in crystalline intraplate crust, and that the faults that are critically stressed maintain the crust's high permeability.

2.5 Faults, Fluids, and Flow

Given that the upper crust's permeability, k, is $\sim 10^{-17}$ to 10^{-16} m^2, we may ask over what lengths of time appreciable hydraulic diffusion occurs. The characteristic diffusion time Ω for fluid of viscosity η and compressibility β_f to diffuse a distance L through a porous

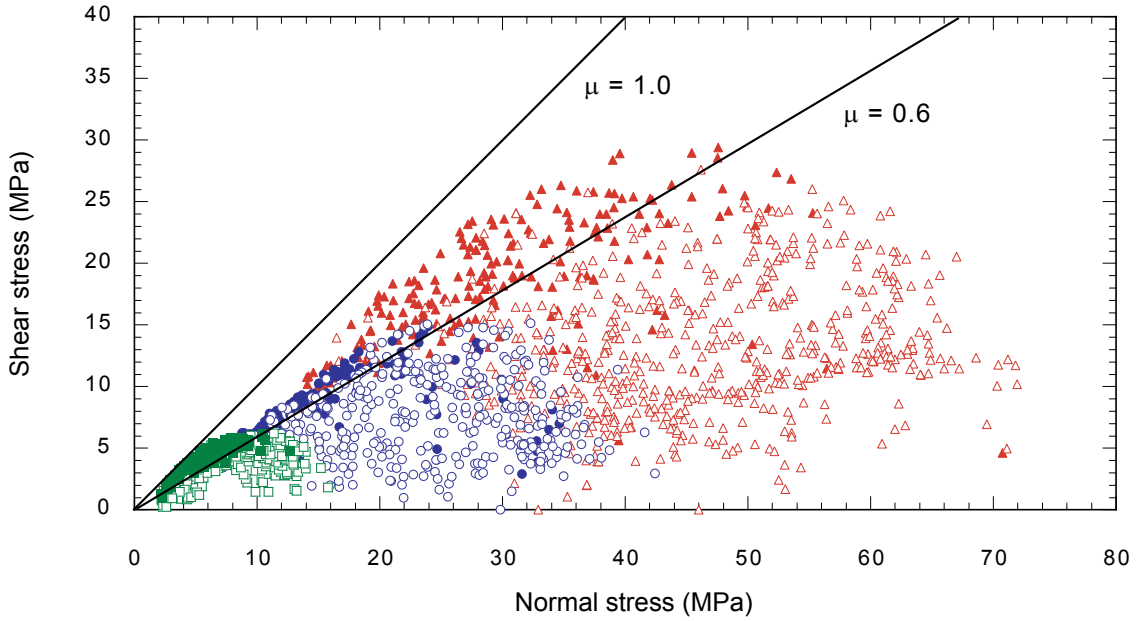

Figure 2.3: Shear and normal stresses on fractures identified with borehole imaging techniques in the Cajon Pass (triangles), Long Valley (circles), and Nevada Test Site (squares) boreholes. Filled symbols represent hydraulically conductive fractures and faults, and open symbols represent nonconductive fractures. Original data from Barton et al. (1995).

medium with porosity φ and compressibility β_r is

$$\Omega = \frac{L^2}{\kappa} \equiv \frac{(\varphi\beta_f + \beta_r)\eta L^2}{k} \tag{2.3}$$

where $\kappa \equiv k/(\varphi\beta_f + \beta_r)\eta$ is the hydraulic diffusivity. For low-porosity rocks (φ <0.02) at average temperatures of 150°C, $\beta_f = 4 \times 10^{-10}$ Pa^{-1}, $\beta_r = 2 \times 10^{-11}$ Pa^{-1}, and $\eta = 1.9 \times 10^{-4}$ Pa s, the previous equation gives

$$\log\Omega = 2\log L - \log k - 16 \tag{2.4}$$

where Ω and L are in years and kilometers, respectively.

This relationship is illustrated for various values of permeability in Figure 2.4. For crustal permeabilities of 10^{-17} to 10^{-16} m^2, the characteristic times for fluid transport over length scales of 1–10 km are of the order of only 10–1000 yr. Thus fluid pressures in the

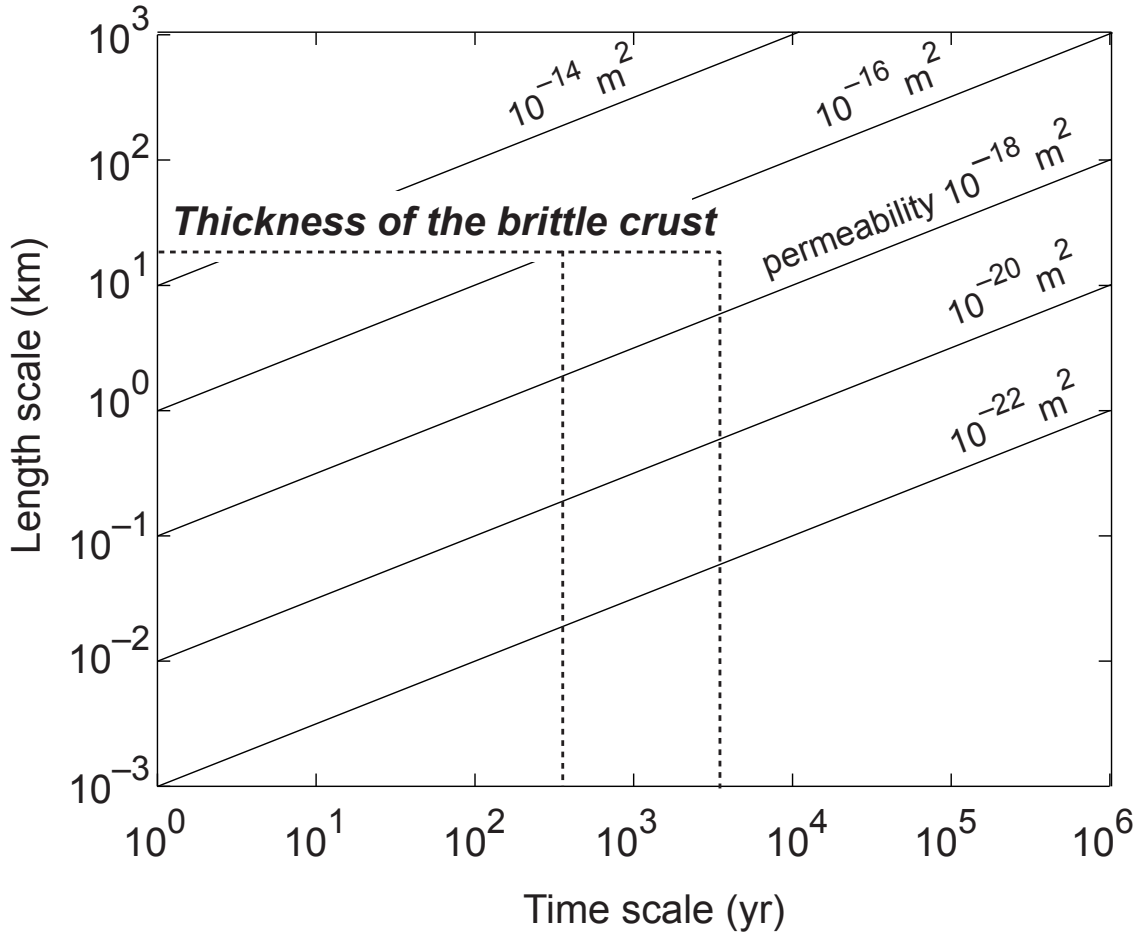

Figure 2.4: Length and time scales for diffusive fluid flow in rock masses of different permeabilities.

crust are expected to equilibrate over relatively short time scales, enabling hydrostatic fluid pressure regimes to be maintained to depths of 10 km or more.

We envisage brecciation associated with slip on critically stressed faults as countering fault-sealing mechanisms by incremental failure and thereby maintaining high permeability. Continual faulting at a small scale appears necessary to maintain high permeability and low fluid pressures. It appears, therefore, that “stable crust” is only a relative term: with respect to stress and faulting we argue that stable intraplate crust is subject to continual small-scale failure. With respect to deformation, however, it is clear that long-term intraplate strain rates must be extremely low.

2.6 Conclusions

The bulk permeability of the upper crust in intraplate regions is $\sim 10^{-17}$ to 10^{-16} m^2 over length scales of 1 to 10 km. Hence, the brittle crust is effectively permeable over time scales of 10 to 1000 yr and pore pressures can be maintained at hydrostatic values. We argue that this high permeability results from hydraulically conductive, critically stressed faults, presumably because brecciation associated with slip on active faults offsets permeability reductions associated with fault-zone sealing. Thus, intraplate crust is able to sustain higher differential stresses than would be possible if bulk permeability were sufficiently low to sustain fluid pressures higher than hydrostatic.

Acknowledgments

Götz Bokelmann, Norm Sleep, and George Thompson made useful comments regarding early versions of this manuscript, for which we thank them. Supported by the National Science Foundation (Award 96-14267) and an Arco Stanford Graduate Fellowship.

2.7 Appendix: Summary of Stress Magnitude Data

The stress magnitude data plotted in Figures 2.1 and Figure 3.1 are summarized in Table 2.2. For the Cajon Pass, Siljan and KTB boreholes, we list estimates of the minimum and maximum values of S_1 and S_3; the corresponding minimum and maximum values of ΔS and $\bar{S} - P_f$ were calculated in the same way as used by Zoback and Harjes (1997).

The uncertainties for the Cajon Pass, Siljan, and KTB data sets presented in Figure 1 of Townend and Zoback (2000) and Figure 1 of Zoback and Townend (2001) are misleading because they imply no correlation between the uncertainties in each of the stress parameters. This is not the case, since only certain pairs of values are realistic (as illustrated, for example, by Figure 10 of Brudy et al., 1997). Rather than reflecting random measurement errors, the ranges of allowable S_1 and S_3 values, or equivalently ΔS and $\bar{S} - P_f$ values, correspond to different assumptions about borehole conditions (such as whether thermal stresses or excess pumping pressure were necessary to initiate fractures).

A more appropriate way of illustrating the true bounds on the in situ stress is therefore to plot two points for each measurement depth, one corresponding to the minimum values of the two stress parameters and the other to the maximum values. Allowable stress states lie near the line joining these two points, which in the case of the three boreholes considered here is found at all depths to be oriented approximately parallel to the overall trend of the mean values in either differential and effective mean stress (Figure 2.1) or principal effective stress coordinates (Figure 3.1).

For the Cajon Pass and Siljan boreholes, and the two deepest measurements made in the KTB borehole, the illustrated uncertainties correspond to the single published estimate at each depth of the minimum compressive stress (S_3) and the largest and smallest values of the maximum compressive stress (S_1) with which it is compatible based on wellbore failure observations (Zoback and Healy, 1992; Lund and Zoback, 1999). Apart from the two deepest points, the KTB data set contains both upper and lower bounds on S_1 and S_3 (Brudy et al., 1997); the minimum and maximum differential and effective mean stresses listed in Table 2.2 and illustrated in Figures 2.1 and 3.1 have been calculated using the two minima and the two maxima respectively.

Table 2.2: Summary of the deep stress magnitude data.

Depth (km)	P_f (MPa)	S_1 (MPa)	S_3 (MPa)	$S_1 - P_f$ (MPa)	$S_3 - P_f$ (MPa)	ΔS (MPa)	$\bar{S} - P_f$ (MPa)
Fenton Hill (Data from Barton et al., 1988, Figure 4)							
3.0	30	80	44	50	14	36	32
4.6	45	122	67	77	22	55	49
Cornwall (Data from Pine et al., 1983; Batchelor and Pine, 1986)							
0.8	8	37	12	29	4	25	17
1.0	10	43	18	33	8	25	21
2.0	20	73	30	53	10	43	32
Dixie Valley (Data from Hickman et al., 1997)							
0.4	4	10	6	6	2	4	4
1.7	17	39	24	22	7	15	15
2.5	24	52	26	28	2	26	14
Cajon Pass (Data from Zoback and Healy, 1992, Table 1)							
0.92	9	12–27	12	3–18	3	0–15	3–10
0.93	9	20–36	14	10–27	4	6–22	7–16
2.05	20	72–87	40	52–67	20	32–47	36–43
2.65	26	59–74	35	33–48	9	24–40	21–29
2.66	26	62–78	33	36–51	7	30–34	22–29
2.71	27	72–98	41	45–71	14	31–57	30–43
2.80	28	66–120	42	39–93	15	24–78	27–54
2.80	28	88–122	42	60–94	15	46–80	38–55
2.97	29	97–131	45	68–102	16	52–86	42–59
2.98	29	74–124	45	45–95	16	29–79	30–55
3.40	33	75–141	51	42–108	18	24–90	30–63
3.51	34	102–144	53	68–110	19	49–91	43–64

continued on following page

continued from previous page

Depth (km)	P_f (MPa)	S_1 (MPa)	S_3 (MPa)	$S_1 - P_f$ (MPa)	$S_3 - P_f$ (MPa)	ΔS (MPa)	$\bar{S} - P_f$ (MPa)
Siljan (Data from Lund and Zoback, 1999, Figure 5)							
4.25	42	126–142	72	84–100	30	54–70	57–65
4.3	42	128–143	74	86–101	32	54–69	59–66
4.4	43	131–147	75	88–104	32	56–72	60–68
4.8	47	142–157	80	95–110	33	62–77	64–71
5.0	49	142–161	82	93–112	33	60–79	63–72
5.1	50	144–163	89	94–113	39	55–74	66–76
KTB (Data from Brudy et al., 1997, Figure 11)							
3.2	31	123–173	49–80	91–142	18–48	74–94	54–95
3.4	33	123–177	53–82	90–145	20–50	70–95	55–97
3.6	35	144–204	58–94	109–169	23–59	86–110	66–98
3.8	37	126–188	61–89	89–151	24–52	66–99	56–101
4.0	39	142–205	66–94	103–166	27–55	76–111	65–110
4.2	41	137–196	67–95	96–155	26–54	70–100	61–104
4.4	43	151–217	75–101	108–174	32–57	76–116	70–115
4.6	45	149–210	79–100	103–165	34–55	70–110	69–110
4.8	47	158–209	82–103	111–162	35–56	76–106	73–109
5.0	49	169–219	88–108	120–171	39–60	80–111	80–115
5.2	51	172–235	91–114	121–184	40–63	82–122	81–123
5.4	53	183–229	95–113	130–176	42–61	88–115	86–118
5.6	55	196–242	99–117	141–187	44–62	98–124	92–124
5.8	57	204–250	103–121	148–193	46–65	102–128	97–129
6.0	58	212–251	108–121	154–193	49–63	104–130	102–128
6.2	60	227–303	112–140	166–243	51–79	115–163	109–161
6.4	62	239–372	117–165	176–310	54–103	122–207	115–206

continued on following page

continued from previous page

Depth (km)	P_f (MPa)	S_1 (MPa)	S_3 (MPa)	$S_1 - P_f$ (MPa)	$S_3 - P_f$ (MPa)	ΔS (MPa)	$\bar{S} - P_f$ (MPa)
6.6	64	251–336	122–150	186–272	58–86	128–186	122–179
6.8	66	264–323	127–150	198–257	61–84	137–173	129–170
7.0	69	284–332	134	215–263	65	150–198	141–164
7.7	75	325–364	152	250–289	77	173–212	164–183

Chapter 3

Lithospheric Failure Equilibrium and Intraplate Deformation[1]

3.1 Abstract

As discussed in Chapter 2, observations from deep boreholes at several locations worldwide indicate that (i) hydrostatic pore pressures persist to depths of as much as 12 km in the upper crust, (ii) the brittle crust is in a state of failure equilibrium according to Coulomb frictional-failure theory, and (iii) bulk permeability is high (10^{-17} to 10^{-16} m^2) apparently due to fluid flow along critically stressed faults. As a result of these factors, the brittle crust is stronger than it would be under near-lithostatic pore pressure conditions.

This result provides a constraint on models of intraplate deformation. Postulating that the upper and lower crust and lithospheric mantle are totally coupled in intraplate regions and that the total strength of the lithosphere is equal to the magnitude of tectonic driving forces ($\sim 3 \times 10^{12}$ N m^{-1}), we have calculated lithospheric strain rates under representative thermal and rheological conditions such that the integrated differential stress over the entire thickness of the lithosphere equals the plate driving force. For a strike-slip stress state and surface heat flow of 60 ± 6 mW m^{-2}, average strain rates are approximately 10^{-18} s^{-1} under hydrostatic upper crustal pore pressure conditions, and approximately 10^{-15} s^{-1} under near-lithostatic pore pressures. The latter strain rates are higher than either observed

[1] Previously published by Zoback and Townend (2001).

geodetically using very long baseline interferometry (VLBI), or estimated on the basis of plate tectonic reconstructions. Hence we argue that hydrostatic upper crustal pore pressures enable lithospheric plates to behave rigidly over time scales of tens to hundreds of millions of years.

3.2 Introduction

From a purely theoretical perspective, the estimated strength of intraplate continental crust varies widely. Analyses of lithospheric flexure indicate that the strength is high (McNutt, 1984) and that the crust can support differential stresses of several hundred megapascals. In contrast, modeling of lithospheric deformation using thin viscous sheet models suggests that the strength of the crust may be quite low over geological time periods (Houseman and England, 1996; England and Houseman, 1986). In this chapter we investigate upper crustal strength and its relation to intraplate deformation.

It is well known that the frictional strength of the crust depends not only on the intrinsic frictional strength of faulted rock, but also on the pore pressure at depth (Hubbert and Rubey, 1959). As pointed out by numerous authors, combining Coulomb frictional-failure theory (Jaeger and Cook, 1979) with laboratory-derived coefficients of friction (e.g., Byerlee, 1978) leads to the conclusion that the brittle strength of the crust is of the order of several hundred megapascals under hydrostatic pore pressure conditions and vanishingly small as pore pressures approach lithostatic values (Sibson, 1974; Brace and Kohlstedt, 1980).

The cumulative strength of the lithosphere is the sum of the brittle strength of the upper crust and the viscous strength of the lower crust and upper mantle. From considerations of tectonic driving forces (slab pull and ridge push), thrust zone topography, and elastic plate deformation, several authors have estimated the total force available to drive lithospheric deformation to be approximately $1\text{–}4\times10^{12}$ N m^{-1} (Forsyth and Uyeda, 1975; Bott and Kusznir, 1984; Kusznir, 1991).

In this chapter we investigate the effects of crustal pore pressure regimes on estimated lithospheric strain rates, subject to the constraint that the total force acting on the lithosphere is 3×10^{12} N m^{-1}. As discussed by Liu and Zoback (1997), maximum intraplate

lithospheric strain rates can be estimated using the constraint that the cumulative strength of the lithosphere in the absence of basal tractions (England and Houseman, 1986),

$$S_L = \int_0^D \Delta S dz \tag{3.1}$$

is equal to the available plate driving force, where D is the thickness of the lithosphere and ΔS is the differential stress. The manner in which the plate driving force is related to lithospheric deformation can be investigated using strength envelopes, incorporating appropriate rheologies to represent the ductile behavior of the lower crust and lithospheric mantle. A test of such models is that the estimated intraplate lithospheric strain rate not exceed approximately 10^{-17} s^{-1}, in order to be consistent with plate tectonic reconstructions (J. Morgan, unpublished). For example, throughout the $\sim$100 Ma duration of the Atlantic Ocean's opening, no more than approximately 100 km of shortening has taken place in the $\sim$10000 km-wide African or South American plates. Thus, the maximum intraplate strain rate is of the order of 100 km/(10000 km $\cdot$ 100 Ma) $\sim 10^{-17}$ s^{-1}. Additionally, VLBI measurements place an upper bound of 10^{-17} s^{-1} on strain rates within the North American plate (Gordon, 1998), and average seismic strain rates in the eastern United States are 10^{-19} to 10^{-18} s^{-1} (Anderson, 1986). We conclude from this that intraplate continental lithosphere does not deform more rapidly than at strain rates of $\sim 10^{-17}$ s^{-1} on geological time scales.

3.3 Coulomb Frictional-Failure Theory

Three independent lines of evidence, summarized in Chapter 2, suggest that a state of failure equilibrium exists within intraplate continental upper crust: (i) seismicity induced by fluid injection (e.g., Raleigh et al., 1972; Pine et al., 1983; Zoback and Harjes, 1997) or reservoir impoundment (Simpson et al., 1988; Roeloffs, 1996); (ii) earthquakes triggering other earthquakes (Stein et al., 1992, 1997), and; (iii) in situ stress measurements in deep boreholes (Zoback and Healy, 1992; Brudy et al., 1997). Additionally, measured stresses are consistently found to be approximately equal to the stresses predicted using Coulomb frictional-failure theory (e.g., Pine et al., 1983; Zoback and Healy, 1984, 1992;

Townend and Zoback, 2000) for laboratory-derived coefficients of friction of 0.6–1.0 (Byerlee, 1978).

The brittle crust's frictional strength can be quantified by considering a pre-existing, cohesionless fault whose normal is at an angle θ to the maximum compressive principal stress, S_1. The shear and effective normal stresses (tractions) on this fault are given, respectively, by

$$\tau = \frac{S_1 - S_3}{2} \sin 2\theta \tag{3.2}$$

$$= \frac{\Delta S_{\text{brittle}}}{2} \sin 2\theta \tag{3.3}$$

and

$$\sigma_n = \frac{S_1 + S_3 - 2P_f}{2} + \frac{S_1 - S_3}{2} \cos 2\theta \tag{3.4}$$

$$= \bar{S} - P_f + \frac{\Delta S_{\text{brittle}}}{2} \cos 2\theta \tag{3.5}$$

where S_3 is the minimum principal stress, P_f is the fluid pressure, and $\Delta S_{\text{brittle}}$ and $\bar{S}$ are the brittle differential stress and mean stress given by $S_1 - S_3$ and $(S_1 + S_3)/2$ respectively (Jaeger and Cook, 1979).

If the fault plane under consideration is critically stressed, then

$$\tau = \mu\sigma_n = \sigma_n \tan\phi \tag{3.6}$$

This is referred to as the Coulomb frictional-failure criterion, in which $\mu = \tan\phi$ is the coefficient of friction and ϕ is referred to as the angle of friction. At failure, $\phi = 2\theta - \pi/2$ and the plane is referred to as "optimally oriented". Combining equations 3.3, 3.5 and 3.6 gives the following, equivalent, results:

$$\frac{S_1 - P_f}{S_3 - P_f} = \left(\sqrt{\mu^2 + 1} + \mu\right)^2 \equiv F \tag{3.7}$$

(Jaeger and Cook, 1979), and

$$\Delta S_{\text{brittle}} = \frac{2\mu}{\sqrt{\mu^2+1}}\left(\bar{S} - P_f\right) \tag{3.8}$$

Derivations of these expressions are given in the appendix to this chapter.

Either of equations 3.7 and 3.8 can be used to predict differential stress as a function of depth in a crust in frictional equilibrium. Equation 3.8 implies that the maximum differential stress at failure, for a given mean stress, decreases with increasing fluid pressure. That is, under hydrostatic (low) fluid pressure conditions, the maximum differential stress withstandable before failure occurs is higher than under lithostatic (high) fluid pressures.

The three end-member stress configurations in which S_1, S_2, or S_3 is the vertical stress $S_v = \rho gz$, corresponding to normal, strike-slip and reverse faulting respectively, give rise to similar explicit relations between depth and maximum differential stress:

$$\Delta S_{\text{brittle}} = \rho gz(\lambda - 1)(1 - F)/F \tag{3.9}$$

$$\Delta S_{\text{brittle}} = 2\rho gz(\lambda - 1)(1 - F)/(1 + F) \tag{3.10}$$

$$\Delta S_{\text{brittle}} = \rho gz(\lambda - 1)(1 - F) \tag{3.11}$$

where F is defined by equation 3.7, and

$$\lambda = \frac{P_f}{S_v} = \frac{P_f}{\rho gz} \tag{3.12}$$

g is the gravitational acceleration, ρ is the mean rock density, and z is depth. Hence, for given stress and pore pressure regimes, we can estimate the maximum differential stress expected on the basis of the critical stress hypothesis, and compare this with observational data.

3.4 Stress and Pore Pressure in the Brittle Crust

In the preceding section it was noted that the brittle crust appears to be in a state of failure equilibrium. Here we briefly summarize data leading to this conclusion, and demonstrate

the manner in which critically stressed faults control not only differential stress levels, but also pore pressures.

Stress data collected at several locations worldwide since the early 1980s indicate almost without exception that differential stresses increase with depth at gradients consistent with equation 3.7 for laboratory-measured coefficients of friction of 0.6–1.0 (Figure 3.1). The dashed black lines are theoretical relationships representing equation 3.7 for various frictional coefficients: it is clear that the stress data from essentially each deep borehole display the interdependency expected for critically stressed crust with frictional coefficients similar to those measured in laboratory experiments (Byerlee, 1978). The data sets presented in Figure 3.1 are augmented by data from shallow depths in the crust ($<$3 km), which also substantiate the observation that the upper crust is critically stressed according to Coulomb frictional-failure theory (McGarr and Gay, 1978; Zoback and Healy, 1984, 1992).

Large-scale hydraulic tests and induced seismicity behavior at these and other locations at depths as great as 9 km demonstrate convincingly that upper crustal permeability is generally 10^{-17} to 10^{-16} m^2 over length scales of 10 to 1000 m (Figure 2.2) and that the associated pore pressures are very close to hydrostatic levels (Table 2.1). Geothermal and metamorphic data also suggest that the permeability of the upper crust exceeds 10^{-18} m^2 throughout the brittle crust (Manning and Ingebritsen, 1999).

Using data from the Cajon Pass, Long Valley and Yucca Mountain USW-G1 boreholes, Barton et al. (1995) demonstrated that optimally oriented planes are hydraulically conductive, whereas non-optimally oriented planes are non-conductive. That is, the faults that limit the crust's strength to that predicted using Coulomb frictional-failure theory are also responsible for limiting pore pressures to hydrostatic values. The authors mapped fracture orientations over the length of each borehole, and tested the hypothesis that optimally oriented faults are associated with localized thermal anomalies, and, by inference, with localized fluid flow. The results (Figure 3.2) clearly indicate that critically stressed faults act as fluid conduits and control large scale permeability (Townend and Zoback, 2000). This conclusion is supported by data collected subsequently from boreholes in Dixie Valley, Nevada (Hickman et al., 1997; Barton et al., 1998) and the Continental Deep Drilling Program (KTB; Kontinentales Tiefbohrprogramm der Bundesrepublik Deutschland) main

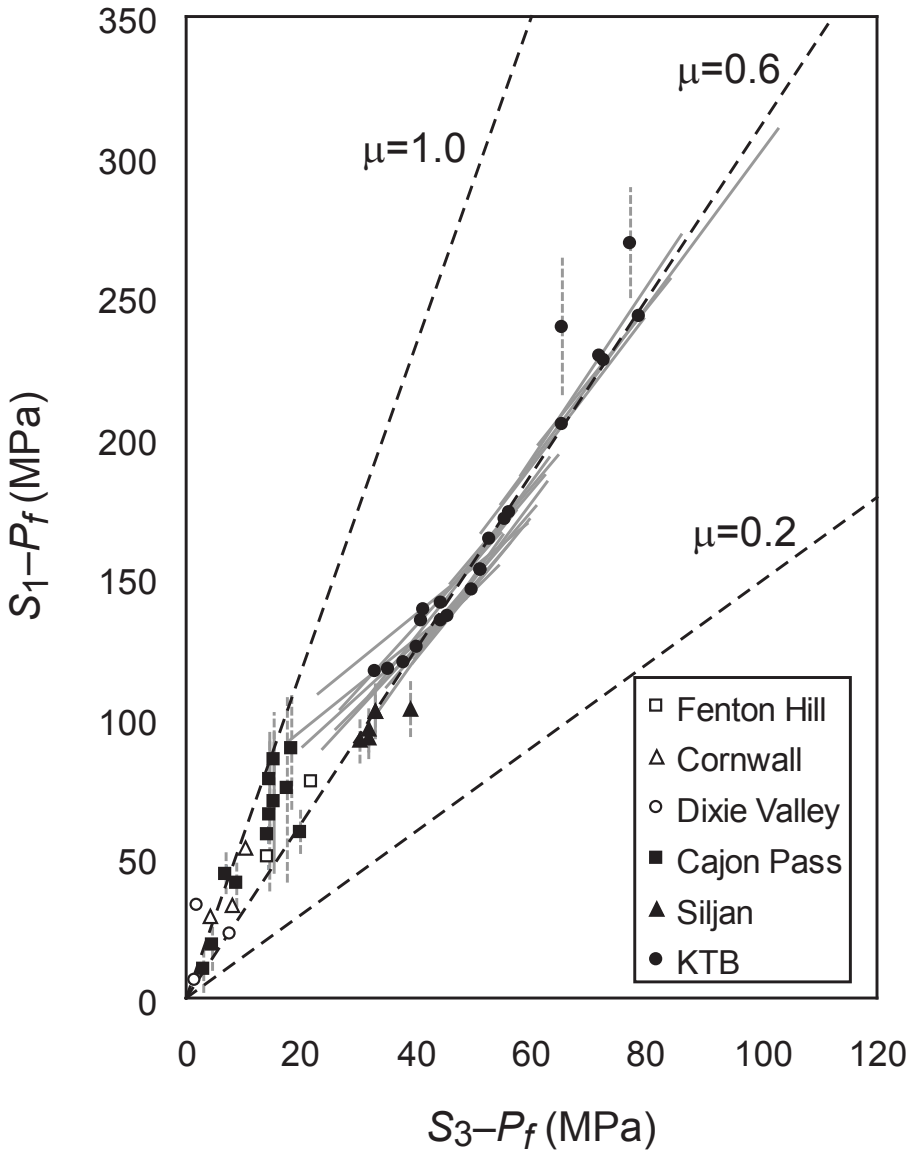

Figure 3.1: Stress data from six of the boreholes listed in Table 2.1 illustrating that the upper crust is in a stress state consistent with that predicted using Coulomb frictional-failure theory (equation 3.7) incorporating frictional coefficients of approximately 0.6–1.0. The uncertainties indicated with dashed grey lines are estimated using a single S_3 measurement and two corresponding S_1 measurements, while those shown with solid grey lines are based on two pairs of S_1 and S_3 values. See Appendix 2.7 for details. Uncertainties have not been plotted for the smaller data sets for the sake of clarity. Sources: Pine et al. (1983), Barton et al. (1988), Zoback and Healy (1992), Hickman et al. (1997), Brudy et al. (1997), and Lund and Zoback (1999).

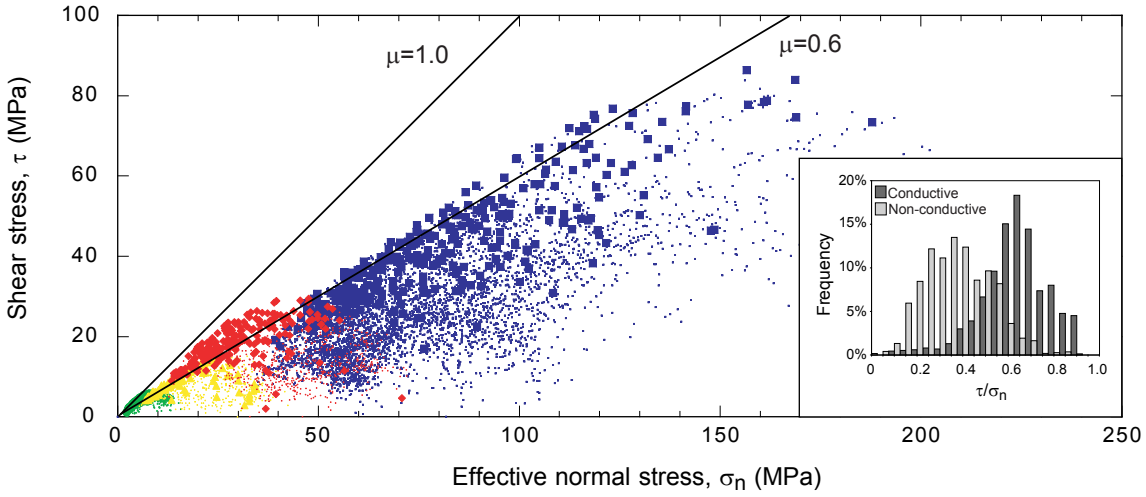

Figure 3.2: Shear and effective normal stresses on fractures identified using borehole imaging techniques in the Cajon Pass (red diamonds and dots), Long Valley (yellow triangles and dots), Nevada Test Site (green circles and dots), and KTB boreholes (blue squares and dots). The larger, filled symbols represent hydraulically conductive fractures and faults, and the dots represent non-conductive fractures. The inset figure illustrates the range in shear to normal stress ratio for all four data sets combined. The number of data in each data set is normalized so that each data set has equal weight. Original data from Barton et al. (1995) and Ito and Zoback (2000).

borehole (Ito and Zoback, 2000). The inset in Figure 3.2 illustrates the combined data sets in terms of the ratio of shear stress to effective normal stress. It is apparent that the mean of this ratio is approximately 0.6 for the conductive fractures (consistent with Coulomb frictional-failure on well-oriented faults), and only ∼0.3 for the non-conductive fractures (indicating that the fractures are not well oriented).

The characteristic diffusion time Ω for fluid of viscosity η and compressibility β_f to diffuse a distance L through a porous medium with porosity φ and compressibility β_r is

$$\Omega = \frac{L^2}{\kappa} \equiv \frac{(\varphi\beta_f + \beta_r)\eta L^2}{k} \tag{3.13}$$

where $\kappa \equiv k/(\varphi\beta_f + \beta_r)\eta$ is the hydraulic diffusivity. For low-porosity rocks (φ <0.02) at average temperatures of 150°C, $\beta_f = 4 \times 10^{-10}$ Pa^{-1}, $\beta_r = 2 \times 10^{-11}$ Pa^{-1}, and $\eta = 1.9 \times 10^{-4}$ Pa s, giving diffusion times of Ω=10–1000 years over distances of 1–10 km,

comparable to the thickness of the brittle crust (Townend and Zoback, 2000). The implication is therefore that, over these intervals of time, pore pressures equilibrate, the crust is effectively permeable, and deep crustal pore pressures are predominantly hydrostatic.

The resulting hydrostatic pore pressures enable faults to withstand high differential stresses before failure, as implied by equation 3.8, making the brittle crust stronger than it would be if pore pressures were higher. In the following section we investigate what effect this high strength has on intraplate lithospheric deformation.

3.5 The Mechanical State of Intraplate Lithosphere

There is a relatively straightforward and intuitive reason why the brittle crust is in failure equilibrium. A force applied to the lithosphere causes the lower crust and upper mantle to undergo ductile deformation. Ongoing ductile creep loads the upper crust, eventually to the point of failure (Figure 3.3). The amount of force that can be sustained by the upper crust is limited to its brittle strength, and any remaining force is available to cause ductile deformation of the lower crust and upper mantle. Hence, stress levels in the upper crust are controlled by its frictional strength, and lithospheric strain rates are controlled by the remaining force and the rheological parameters of the ductile lithosphere. If the brittle and ductile layers of intraplate lithosphere are coupled, then the entire lithosphere deforms at the same strain rate (Liu and Zoback, 1997).

We wish to investigate the roles played by upper crustal critical stress states and hydrostatic pore pressures in controlling the distribution of strength (integrated differential stress, equation 3.1) in intraplate lithosphere and the rates at which intraplate lithosphere deforms. Equations 3.9–3.11 enable us to estimate how differential stress increases with depth in the brittle crust based on the critical stress hypothesis. As is well known, at mid-crustal depths, however, the temperature is sufficiently high that ductile failure mechanisms are active at lower differential stress levels than required for brittle faulting (Sibson, 1983; Chen and Molnar, 1983; Kohlstedt et al., 1995). Following previous authors, we model the rheologies of the ductile crust and lithospheric mantle using power-law creep relationships (Brace and Kohlstedt, 1980). In this case the ductile strain rate $\dot{\varepsilon}$ is given in terms of the

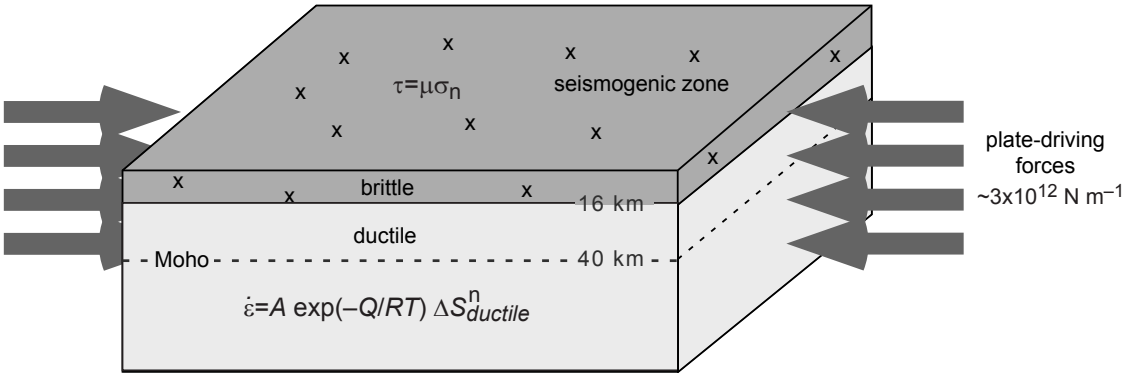

Figure 3.3: Schematic illustration of the layered mechanical structure of continental lithosphere assumed for the strain rate calculations.

differential stress by

$$\dot{\varepsilon} = A \exp\left(-\frac{Q}{RT}\right) \Delta S^n_{\text{ductile}} \tag{3.14}$$

so that

$$\Delta S_{\text{ductile}} = \sqrt[n]{\frac{\dot{\varepsilon}}{A} \exp\left(\frac{Q}{RT}\right)} \tag{3.15}$$

Here A, n and Q are material parameters (the flow parameter, stress exponent and activation energy respectively), R is the gas constant and T is the absolute temperature (Ranalli and Murphy, 1987). This is a uniaxial, isotropic model in the sense that the orientation of the stress tensor, or equivalently the direction in which the lithosphere is induced to yield, is neglected.

At any depth in the crust, we postulate that the rock deforms by whichever mechanism requires the lower differential stress, in which case

$$\Delta S = \min\left(S_{\text{brittle}}, S_{\text{ductile}}\right) \tag{3.16}$$

$\dot{\varepsilon}$ is nonzero for any nonzero differential stress, and therefore even in the brittle regime

a strain rate exists such that the rock deforms ductilely at a lower differential stress than required for brittle failure. However, by invoking the constraint that the total lithospheric force be 3×10^{12} N m^{-1} and assuming that the upper crust, lower crust and lithospheric mantle are fully coupled, a single strain rate for the whole lithosphere can be found.

3.6 Modeling Procedure

Our basic modeling procedure consists of first calculating the differential stresses required for brittle and ductile deformation separately, as functions of depth, and then combining the two profiles according to equation 3.16 to produce a composite differential stress profile. Integrating this profile over the thickness of the lithosphere gives the cumulative strength, which must equal 3×10^{12} N m^{-1}. Note that this technique differs fundamentally from those of several other authors (e.g., Sibson, 1983; Ranalli and Murphy, 1987; Kohlstedt et al., 1995) in so far as that the lithospheric strain rate is a dependent variable and not a free parameter.

A generalized lithospheric structure composed of a 16 km-thick felsic upper crust (with rheological properties of dry Adirondack granulite), 24 km-thick mafic lower crust (dry Pikwitonei granulite), and 60 km-thick lithospheric mantle (wet Aheim dunite) is assumed, based on the composite velocity-depth model obtained by Christensen and Mooney (1995), and rheological coefficients from Carter and Tsenn (1987) and Wilks and Carter (1990). In a semi-infinite layered half-space with zero temperature at the surface, the steady-state temperature profile is given by

$$T(z) = \sum_{i=1}^{N} \left[\frac{q_{i-1}\Delta z_i}{K_i} - \frac{H_i \Delta z_i^2}{2K_i} \right] \tag{3.17}$$

The volumetric heat production, thermal conductivity, thickness and basal heat flow of the ith layer are H_i, $K_i(T)$, Δz_i and $q_i = q_{i-1} - H_i \Delta z_i$, respectively. We have incorporated a very simple heat productivity model, in which the heat productivities of the upper crust, lower crust and lithospheric mantle are constant (cf. Pollack and Chapman, 1977; Chapman and Furlong, 1992), and equal to 1.1 W m^{-3}, 0.40 W m^{-3} and 0.02 W m^{-3} respectively (Jaupart et al., 1998; Rudnick et al., 1998). We assume thermal conductivity to be a function of both

temperature and depth, according to relations presented by Chapman and Furlong (1992) and Schatz and Simmons (1972).

Continental-scale stress mapping (Zoback and Zoback, 1980, 1989, 1991; Zoback, 1992) indicates that stable continental lithosphere typically exhibits oblique strike-slip stress states (i.e. $S_2 = S_v$). We have incorporated a strike-slip stress state in the modeling, with the additional assumption that $S_2 = \bar{S}$. In this case, differential stress is given as a function of depth by equation 3.10.

We treat pore pressures in the lower crust as near-lithostatic, following the arguments presented by Nur and Walder (1990). At elevated temperatures, processes of permeability reduction by chemical precipitation and inelastic deformation are expected to occur at rates sufficient to preclude rapid fluid migration, and hence to favor high pore pressures. Specifically, the permeability of the lower crust probably does not exceed 10^{-19} m^2 at 30 km depth (Manning and Ingebritsen, 1999) implying long characteristic diffusion times ($> 10^5$ years) such that near-lithostatic pore pressures are likely to be maintained.

Given the temperature-depth profile and an initial estimate of the ductile strain rate, $\dot{\varepsilon}$, we can calculate differential stresses in the ductile portions of the upper and lower crust and lithospheric mantle using equation 3.15. However, the strain rate calculations involve several parameters whose values are non-unique (such as surface heat flow, conductivity, upper crustal heat productivity, the frictional coefficient, and the rheological parameters of each layer). We have investigated the effects of variations in each of these parameters using a Monte Carlo technique: 1000 estimates of each parameter are drawn at random from normal distributions and 1000 separate models constructed, so that the jth model is a function of $q_0(j)$, $K(j)$, (j), etc. Composite temperature–depth, differential stress–depth and strength–depth profiles are constructed by stacking the different models' results. The values of the modeling parameters are listed in Table 3.1.

To summarize, we wish to calculate a single lithospheric strain rate such that the integral of the differential stress profile is equal to the postulated strength of the lithosphere, namely 3×10^{12} N m^{-1}. To accommodate uncertainties in the input parameters, we perform 1000 Monte Carlo simulations: for each simulation, we iteratively adjust the strain rate until the strength criterion is met.

Parameter (symbol)	Value	Units
Density (ρ)	2800	kg m^{-3}
Coefficient of friction (μ)	0.8*	–
Thickness (z)		
Upper crust	16	km
Lower crust	24	km
Lithospheric mantle	60	km
Conductivity (K)		
Upper crust (nominal)	3.0*	W m^{-1} K^{-1}
Lower crust (nominal)	2.6*	W m^{-1} K^{-1}
Lithospheric mantle(nominal)	3.4	W m^{-1} K^{-1}
Heat productivity (H)		
Upper crust	1.1	μW m^{-3}
Lower crust	0.4	μW m^{-3}
Lithospheric mantle	0.02	μW m^{-3}
Flow parameter (A)		
Upper crust	0.08*	MPa^{-n} s^{-1}
Lower crust	12589*	MPa^{-n} s^{-1}
Lithospheric mantle	398	MPa^{-n} s^{-1}
Stress exponent (n)		
Upper crust	3.1*	–
Lower crust	4.2*	–
Lithospheric mantle	4.5*	–
Activation energy (Q)		
Upper crust	243*	kJ mol^{-1}
Lower crust	445*	kJ mol^{-1}
Lithospheric mantle	498*	kJ mol^{-1}

Table 3.1: Values of the parameters used in the lithospheric strength calculations. Asterisks (*) indicate those parameters that were varied in the Monte Carlo routine: each parameter was drawn at random from a specific normal distribution with the listed mean ($\bar{x}$) and standard deviation (σ) such that $3\sigma = 0.2\bar{x}$, giving approximately 20% variation.

3.6.1 Model Limitations

We have opted to treat the ductile behavior of the lithosphere as being dominated by dislocation (power-law) creep, and have not incorporated diffusion (linear) creep into the models. Karato and Wu (1993) suggested that diffusion creep may occur in the shallow asthenospheric mantle beneath continental lithosphere but noted that several parameters, particularly grain size and the dislocation creep activation volume, make it difficult to accurately determine the depths at which each mechanism dominates. We have consequently neglected diffusional effects in the interests of simplicity.

Additionally, we have used thermal parameters considered representative of stable continental crust, and a correspondingly representative lithospheric structure. However, the rheologies of the lower crust and mantle are poorly known. For example, if the mantle had the rheology of dry Aheim dunite — for which $A = 32000$ MPa^{-n} s^{-1}, $n = 3.6$, and $Q = 498$ kJ mol^{-1} (Carter and Tsenn, 1987) — rather than wet, it would deform much less rapidly for a given differential stress. Furthermore, the strength of the lower crust is modeled here assuming near-lithostatic pore pressures in the lower crust.

Our modeling procedure accommodates variation in several of the input parameters (as listed in Table 2) but we have not allowed the strength constraint to vary. 3×10^{12} N m^{-1} is an intermediate estimate of the strength of the lithosphere (Kusznir, 1991) and we have decided not to vary this value in order to facilitate interpretation of the differential stress and strength profiles.

3.7 Results

Figure 3.4 illustrates the modeling results corresponding to surface heat flow of 60 ± 6 mW m^{-2} (mean$\pm$10%), representative of stable continental heat flow (Pollack et al., 1993). The uppermost plots (a–c) display the model results assuming hydrostatic pore pressures in the upper crust (for which λ defined in equation 3.12 is approximately 0.4), and the three middle plots (d–f) display the corresponding results for near-lithostatic pore pressures (λ=0.9). Note that the temperature-depth profiles are the same in both cases. At the bottom of the figure is a histogram (g) illustrating the range of estimated strain rates under each pore

pressure condition: the strain rates are distributed log-normally about a geometric mean of approximately 10^{-18} s^{-1} under near-hydrostatic upper crustal pore pressure conditions. In comparison, under near-lithostatic pore pressures the average strain rate is approximately 10^{-15} s^{-1}.

Differences in the distribution of strength within the lithosphere can be clearly observed by comparing plots (c) and (f). For the strike-slip stress state and hydrostatic pore pressures, the 16 km-thick upper crust provides $\sim 1.5 \times 10^{12}$ N m^{-1} (1/2) of the total lithospheric strength, whereas it accounts for $\sim 0.5 \times 10^{12}$ N m^{-1} (1/6) under near-lithostatic pore pressures.

The significance of the strain rate results can be appreciated by comparing them with the value of 10^{-17} s^{-1} given above for the maximum intraplate strain rate. On the basis of our models, strain rates under near-hydrostatic upper crustal pore pressure conditions and stress and thermal regimes characteristic of intraplate regions are likely to be less than 10^{-17} s^{-1}, whereas they are likely to substantially exceed 10^{-17} s^{-1} under near-lithostatic pore pressure conditions. The latter rates are greater than those observed in stable continental lithosphere and it therefore appears that the lithosphere's rigidity may be controlled by upper crustal pore pressures. While we did not investigate the effects of variations in total lithospheric strength in great detail, repeating these calculations for a somewhat stronger lithosphere (total strength of 4×10^{12} N m^{-1}) gives similar results; average strain rates under hydrostatic and lithostatic upper crustal fluid pressure conditions are approximately 3×10^{-17} s^{-1} and 3×10^{-14} s^{-1}, respectively.

Note, however, that for lower surface heat flows of 50 ± 5 mW m^{-2} — such as are typical of Proterozoic and Archean cratonic crust (Pollack et al., 1993) — or for overall weaker lithosphere (with a total strength of $\sim 1 \times 10^{12}$ N m^{-1}, equivalent to the lowest published value quoted above), strain rates are lower than 10^{-20} s^{-1} under either pore pressure regime. We suggest, therefore, that in intraplate regions with other than very low heat flow or low applied forces, hydrostatic pore pressures in the upper crust give the lithosphere sufficient rigidity for plate tectonics to occur. In low heat-flow regions of stable continental crust, pore pressures do not seem to play a significant role in determining lithospheric strain rates.

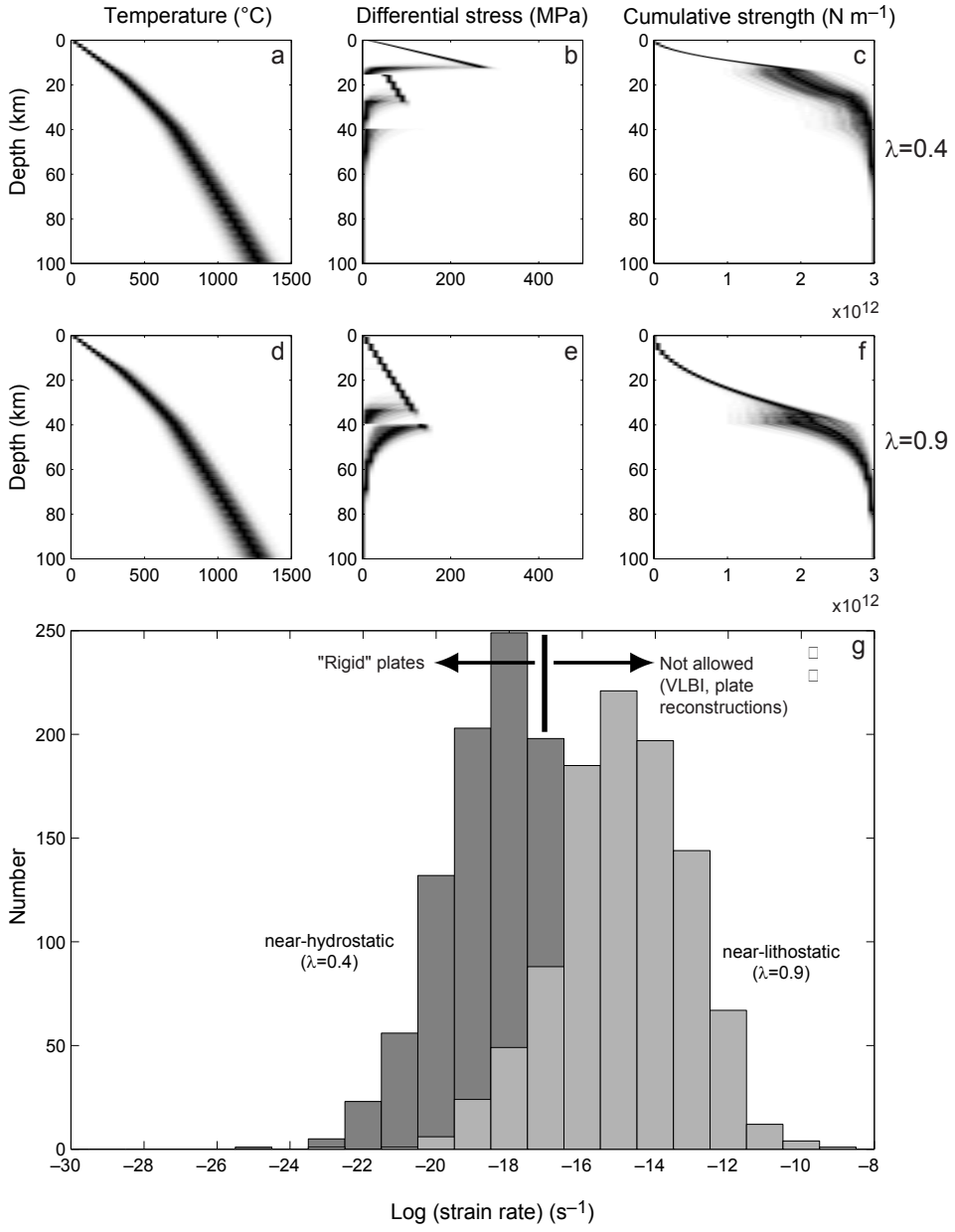

Figure 3.4: Results of 1000 Monte Carlo calculations for a strike-slip stress state and surface heat flow of 60±6 mW m^{-2}, subject to the constraint that the total strength of the lithosphere is 3×10^{12} N m^{-1}. (a), (b), and (c) are the temperature, differential stress, and cumulative strength profiles respectively under near-hydrostatic upper crustal pore pressure conditions (λ=0.4), and (d), (e), and (f) are the corresponding profiles under near-lithostatic conditions (λ=0.9). (g) illustrates the range of calculated lithospheric strain rates under each condition.

3.8 Conclusions

Numerous data obtained from deep boreholes worldwide reveal that upper crustal permeabilities are sufficiently high (10^{-17} to 10^{-16} m^2) that pore pressures attain hydrostatic values over geologically short periods of time (10 to 1000 years). These high permeabilities appear to be maintained by hydraulically conductive, critically stressed faults. Such faults limit the strength of the brittle crust and, since the ductile lithosphere is postulated to deform at any finite differential stress, the strength of the lithosphere as a whole. Given therefore that the crust is both critically stressed and capable of sustaining tectonic stresses of approximately 3×10^{12} N m^{-1}, the strength of intraplate lithosphere must equal the imposed plate tectonic stress.

We have used a total force constraint on models of lithospheric strength profiles to determine at what strain rates intraplate lithosphere deforms. We estimate that under strike slip stress regimes and thermal conditions representative of stable continental regions, hydrostatic upper crustal pore pressures are associated with strain rates of less than 10^{-17} s^{-1}, whereas lithostatic pore pressures produce unrealistically high strain rates: the lithosphere cannot deform more rapidly than approximately 10^{-17} s^{-1} or lithospheric plates would not be sufficiently rigid for plate tectonic processes to occur on time scales of millions of years. We conclude, therefore, that hydrostatic pore pressures in the upper crust are necessary in other than very low heat flow regions for the lithosphere to deform sufficiently slowly that plates behave as if rigid, and hence for plate reconstructions to be possible.

Acknowledgments

We thank Terry Engelder, Steve Miller, and Jean-Louis Vigneresse for their constructive reviews of this work. Financial support of the National Science Foundation (Award 96-14267) and an Arco Stanford Graduate Fellowship is gratefully acknowledged.

3.9 Appendix: Stress Profiles in Critically Stressed Crust

To obtain equation 3.7 we substitute equations 3.3 and 3.5 into the Coulomb frictional-failure criterion, equation 3.6:

$$\tau = \mu\sigma_n \tag{3.18}$$

$$\frac{S_1 - S_3}{2}\sin 2\theta = \mu\left[\frac{S_1 + S_3 - 2P_f}{2} + \frac{S_1 - S_3}{2}\cos 2\theta\right] \tag{3.19}$$

which we rearrange to give

$$\frac{S_1 - P_f}{S_3 - Pf} = \frac{\sin 2\theta + \mu(1 - \cos 2\theta)}{\sin 2\theta - \mu(1 + \cos 2\theta)} \tag{3.20}$$

$$= \frac{\cos\phi + \mu(1 + \sin\phi)}{\cos\phi - \mu(1 - \sin\phi)} \tag{3.21}$$

since $\phi = 2\theta - \pi/2$ for a critically stressed fault. Next, $\mu = \tan\phi$, so that $\sin\phi = \mu/\sqrt{\mu^2+1}$ and $\cos\phi = 1/\sqrt{\mu^2+1}$, in which case the relation simplifies to

$$\frac{S_1 - P_f}{S_3 - Pf} = \frac{\sqrt{\mu^2+1} + \mu}{\sqrt{\mu^2+1} - \mu} = 1 + 2\mu^2 + 2\mu\sqrt{\mu^2+1} \tag{3.22}$$

$$= \left(\sqrt{\mu^2+1} + \mu\right)^2 \tag{3.23}$$

as required.

Likewise, we can obtain equation 3.8 by expressing equations 3.3 and 3.5 in terms of the differential and mean stresses,

$$\tau = \frac{\Delta S_{\text{brittle}}}{2}\sin 2\theta \tag{3.24}$$

and

$$\sigma_n = \bar{S} - P_f + \frac{\Delta S_{\text{brittle}}}{2}\cos 2\theta \tag{3.25}$$

On substituting τ and σ_n into equation 3.6 and simplifying we obtain

$$\Delta S_{\text{brittle}} = \frac{2\mu}{\sin 2\theta - \mu \cos 2\theta}(\bar{S} - P_f) \tag{3.26}$$

where, as above, we can rewrite the equations in terms of ϕ, and make use of the trigonometric relationships between ϕ and μ to give

$$\Delta S_{\text{brittle}} = \frac{2\mu}{\sqrt{\mu^2 + 1}}(\bar{S} - P_f) \tag{3.27}$$

Equations 3.9–3.11 can be obtained by simply substituting the appropriate expressions for S_1 and S_3 (listed below) into equation 3.7 and rearranging:

normal:	$S_1 = S_v = \rho g z$, $S_3 = \rho g z - \Delta S_{\text{brittle}}$
strike-slip:	$S_2 = S_v = \rho g z$, $S_1 = \rho g z + \Delta S_{\text{brittle}}/2$, $S_3 = \rho g z - \Delta S_{\text{brittle}}/2$
reverse:	$S_3 = S_v = \rho g z$, $S_1 = \rho g z + \Delta S_{\text{brittle}}$

Chapter 4

Tectonic Stress Orientations in Southern California[1]

4.1 Abstract

Analysis of stress orientation data from earthquake focal plane mechanisms adjacent to the San Andreas fault in the San Francisco bay area and throughout southern California indicates that the San Andreas fault has low frictional strength. In both regions, available stress orientation data indicate low levels of shear stress on planes parallel to the San Andreas. In the San Francisco Bay area, focal mechanisms from within 5 km of the San Andreas and Calaveras fault zones indicate a direction of maximum horizontal compression nearly orthogonal to both subvertical, right-lateral strike-slip faults, a result consistent with those obtained previously from studies of aftershocks of the 1989 Loma Prieta earthquake. In southern California, the direction of maximum horizontal stress near the San Andreas is nearly everywhere at a high angle to the fault, similarly indicating that the fault has low frictional strength. Thus, along these two major sections of the San Andreas fault (which produced great earthquakes in southern California in 1857 and central and northern California in 1906), the frictional strength of the fault is much lower than expected for virtually any common rock type if near-hydrostatic pore pressure exists at depth, and so low as to produce no discernible shear-heating anomaly.

[1] Previously published by Townend and Zoback (2001).

Our findings in southern California are in marked contrast to recent suggestions by Hardebeck and Hauksson (1999) that stress orientations rotate within ∼25 km of the fault, which prompted a high frictional strength model of the San Andreas fault (Scholz, 2000). As we utilize the same stress data and inversion methodology as Hardebeck and Hauksson (1999), we interpret the difference in our findings as being related to the way in which we group focal plane mechanisms to find the best-fitting stress tensor. We suggest that the Hardebeck and Hauksson (1999) gridding scheme may not be consistent with the requisite a priori assumption of stress homogeneity for each set of earthquakes.

Finally, we find no evidence of regional stress changes associated with the occurrence of the 1992 **M** 7.4 Landers earthquake, again in apparent contradiction with the findings of Hardebeck and Hauksson (1999).

4.2 Introduction

While it is well known that the San Andreas fault (SAF) system (Figure 4.1) has been the locus of prolonged, localized deformation in the lithosphere separating the Pacific and North American plates for several million years, the level of shear stress required to cause the major faults of the San Andreas system to slip in earthquakes in the seismogenic, upper ∼15 km of the crust remains controversial (Lachenbruch and McGarr, 1990). Specifically, while laboratory experiments systematically reveal coefficients of friction of between 0.6 and 1.0 (Byerlee, 1978) — consistent with stress levels measured to depths of several kilometers in intraplate regions (Chapter 2) — two lines of evidence suggest that coefficients of friction, μ, along the major faults of the San Andreas system are substantially lower. First, heat flow data reveal that the surface trace of the SAF is not associated with the marked, positive thermal anomaly expected if the coefficient of friction were any higher than 0.2 (Brune et al., 1969; Lachenbruch and McGarr, 1990; Lachenbruch and Sass, 1980, 1992). Second, measurements of principal stress directions along the SAF suggest that the angle between the greatest compressive stress direction and the fault plane almost invariably exceeds that expected for μ=0.6–1.0 ("hydrostatic Byerlee's law"; Brace and Kohlstedt, 1980; Townend and Zoback, 2000) and, in fact, locally exceeds 80° at several locations (Mount and Suppe, 1987; Zoback et al., 1987; Jones, 1988; Oppenheimer et al., 1988; Zoback and

Beroza, 1993). Such high angles of compression imply friction coefficients of less than 0.1 (Lachenbruch and Sass, 1992) or high fluid pressures within the fault zone (Rice, 1992).

Hardebeck and Hauksson (1999) recently suggested that while the far-field axis of greatest horizontal compression, S_{Hmax}, is at a high angle to the average strike of the SAF throughout much of southern California, the stress tensor rotates systematically adjacent to the fault so that the relevant near-field angle is $\sim 45^{\circ}$. The authors suggested that this behavior is particularly pronounced in the vicinity of the "Big Bend" area near Fort Tejon. This led Scholz (2000) to postulate a mechanical model of the SAF in which the fault is strong and stress rotation is a direct consequence of frictionless slip below the locked zone at depth.

In this paper we use well-located earthquake focal mechanisms to infer principal stress orientations in the vicinity of the San Andreas fault system in the San Francisco Bay area and in southern California (Figure 4.1). Our primary aim is to determine the orientation of S_{Hmax} "close" to the SAF and adjacent faults, where "close" denotes a distance less than the thickness of seismogenic crust ($\sim$10–15 km). In the San Francisco Bay area we have compiled previous workers' results and obtained an additional stress orientation result by focal mechanism inversion. With respect to southern California, our motivation is to repeat the analysis of Hardebeck and Hauksson (1999) with the specific objective of investigating the influence of their gridding scheme. In other words, we wish to address the method with which they grouped focal mechanism data to determine stress orientations.

The fundamental basis for inverting a group of fault slip observations or focal mechanisms to determine stress orientations is the assumption that slip in each event occurred within a uniform stress field (Angelier, 1979, 1984; Gephart and Forsyth, 1984; Michael, 1984, 1987). Hardebeck and Hauksson (1999) used rectangular boxes when selecting focal mechanisms for inversion to examine stress orientation as a function of distance from the San Andreas fault. The dimensions of these boxes varied greatly, from as little as 25 km and 2 km in the local strike-parallel and strike-perpendicular directions, respectively, to more than 150 km and 60 km. Along the Fort Tejon profile, on which the Scholz (2000) model was subsequently based, the strike-parallel length of the boxes is 80 km: consequently, focal mechanisms separated by as much as $\sim$80 km were combined into boxes for inversion. Given that the SAF exhibits a $\sim 25^{\circ}$ change of strike in the Fort Tejon area and intersects

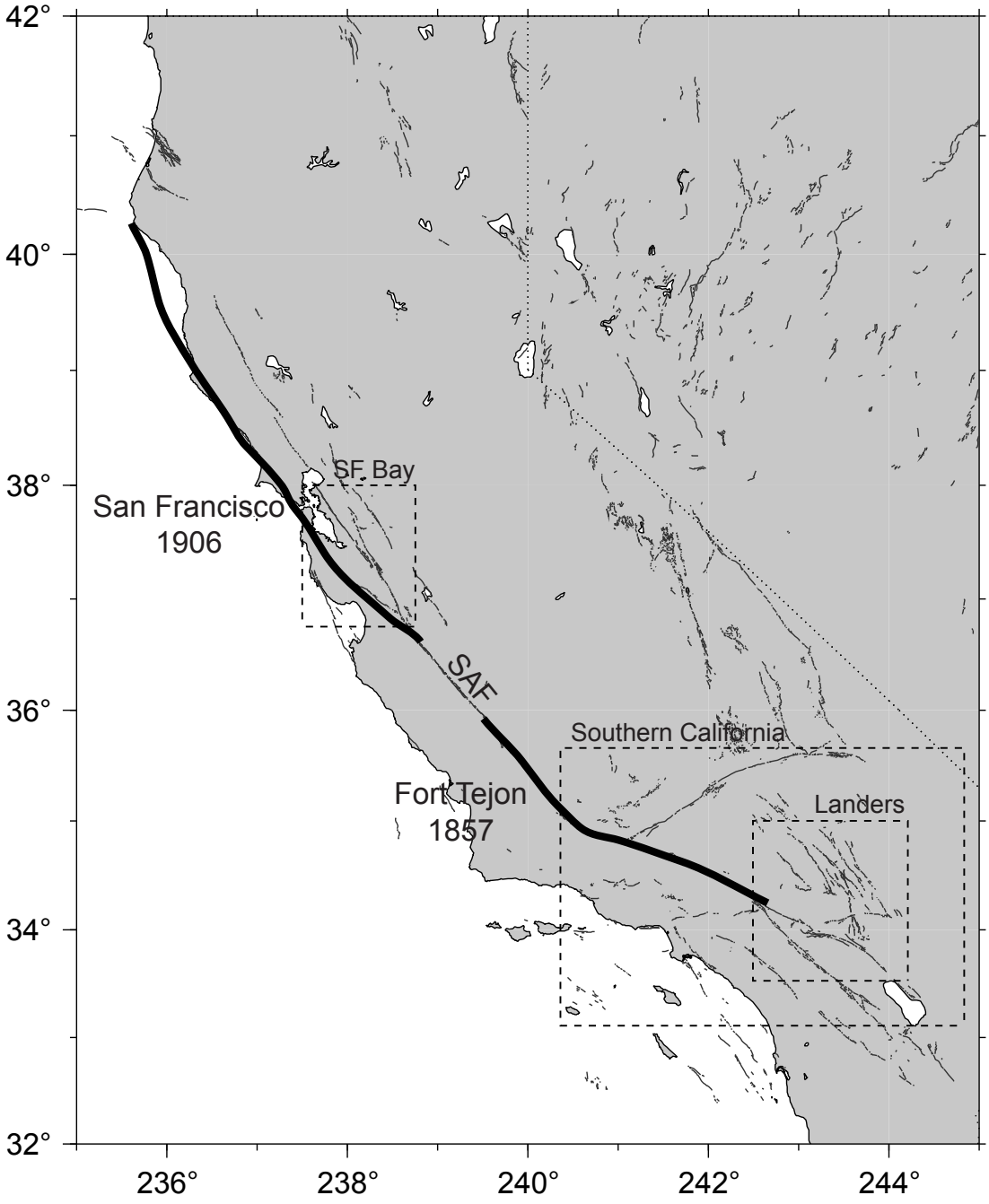

Figure 4.1: Map of California illustrating the San Andreas fault (SAF) and other major faults. The thick lines along sections of the San Andreas fault indicate those portions of the fault that ruptured during the 1857 Fort Tejon and 1906 San Francisco earthquakes. The areas corresponding to Figures 4.2, 4.4, and 4.6a are shown by the dashed boxes.

the left-lateral Garlock Fault, stress is unlikely to be homogeneous on 80 km scales, and it may be inappropriate to group such widely separated focal mechanisms. Simply put, that gridding scheme may not be consistent with the a priori assumption of stress homogeneity within each group of earthquakes.

Finally, using the southern California data set we wish to examine the possibility of stress changes induced by the 1992 Landers earthquake. Hardebeck and Hauksson (1999) reported an apparent clockwise stress rotation of as much as 40° caused by the 1992, **M** 7.4 Landers earthquake. If this were the case, it would indicate that the stress changes associated with these two earthquakes were of comparable magnitude to tectonic stress levels. As average earthquake stress drops (determined seismologically) of 1–10 MPa (Kanamori and Anderson, 1975) are quite small relative to crustal stress levels consistent with hydrostatic Byerlee's law, any such stress rotations would imply that the crust, as well as major faults, had low frictional strength.

4.3 Stress in the San Francisco Bay Area

Four major NNW-striking faults, the San Gregorio, San Andreas, Hayward and Calaveras faults (Figure 4.2), accommodate varying amounts of right-lateral slip and relative plate motion in the San Francisco Bay area. San Francisco Bay itself, bounded to the southwest and northeast by the San Francisco Peninsula Ranges and the Diablo Ranges/East Bay Hills respectively, is relatively aseismic, but microseismicity levels are high along each of the principal fault strands, and the region has experienced several major historic earthquakes. Notable 20th century events include the 1906 **M** 7.8 San Francisco and 1989 **M** 6.9 Loma Prieta earthquakes on the SAF, and the 1984 **M** 6.2 Morgan Hill earthquake on the Calaveras fault .

Previous studies using focal mechanisms of aftershocks following the Morgan Hill and Loma Prieta events have revealed stress orientations in which the angles between S_{Hmax} and the local fault strike are $\sim 70^\circ$ and $\sim 90^\circ$ (Oppenheimer et al., 1988; Zoback and Beroza, 1993). We have supplemented these two results with one other obtained for a suite of 28 earthquakes that occurred on the southern San Francisco Peninsula (the area encompassed by the box along the SAF west of San Jose in Figure 4.2) between 1970 and 1999 (Zoback

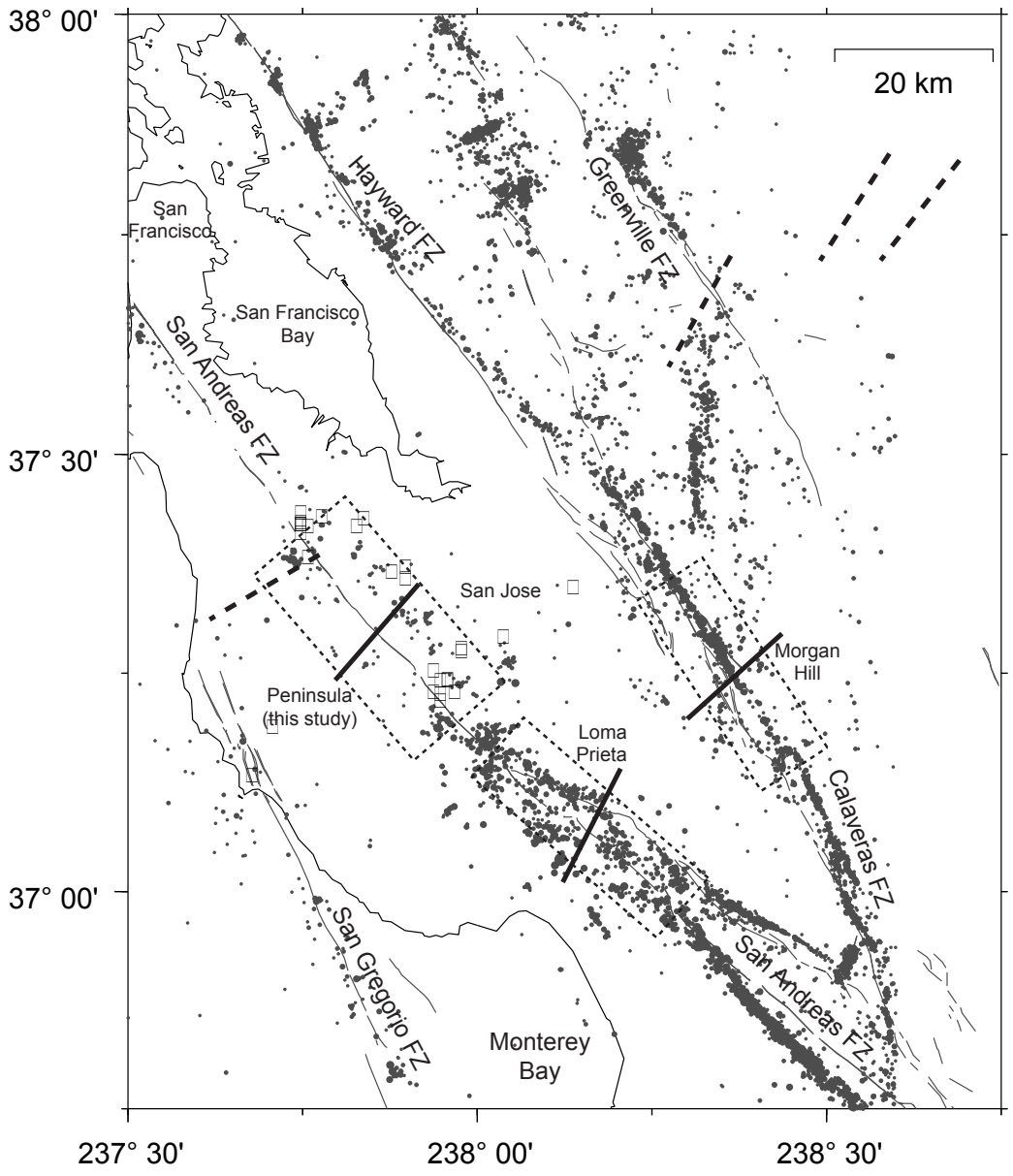

Figure 4.2: Map of the San Francisco Bay area showing the orientation of S_{Hmax} obtained by focal mechanism inversion (solid lines) and borehole breakout analysis (dashed lines). The dotted rectangles centered on the three focal mechanism results illustrate the spatial distribution of focal mechanisms used in the 1984 Morgan Hill (Oppenheimer et al., 1988), 1991 Loma Prieta (Zoback and Beroza, 1993), and southern San Francisco Peninsula stress inversions (this study). The dots indicate seismicity larger than **M** 2 between 1965 and 2000. Fault data courtesy of the California Department of Mines and Geology.

et al., 1999). These earthquakes are shown in cross section in Figure 4.3a: they occurred on either side of the quiescent SAF and exhibited a mixture of reverse and strike-slip focal mechanisms. We have used the inversion algorithm of Gephart and Forsyth (1984) and Gephart (1990a,b) to determine an optimal stress tensor that minimizes the L1-norm misfit between the observed and calculated shear tractions on either of the two nodal planes in each focal mechanism. Not unexpectedly, the inversion indicates a strike-slip/reverse faulting regime in which the intermediate and least principal stresses have approximately the same magnitude. The best-fitting solution is illustrated in Figure 4.3b: the trend and plunge of S_1,[2] which is S_{Hmax} in this case, are 221° and 6°, respectively. S_2 and S_3 (the vertical stress) trend 130° and 334°, and plunge 14° and 75° respectively. The average misfit of the optimal solution for the 28 focal mechanisms is 4.9°. It is clear from these results that near fault-normal compressive stress exists in the seismogenic crust immediately adjacent to the SAF.

This finding is similar to that of Oppenheimer et al. (1988) who studied aftershocks of the 1984 Morgan Hill earthquake. A precise relocation of these events is shown in Figure 4.3c (D. Schaff, pers. comm. to J. Townend, 2001; Schaff et al., 2002). Thrust events on planes parallel to the Calaveras fault and strike-slip events on N–S-trending faults are seen adjacent to the right-lateral, strike-slip Calaveras fault. As in the case of the events along the SAF, Oppenheimer et al. (1988) found a best-fitting stress tensor for which S_{Hmax} was essentially perpendicular to the trend of the Calaveras fault (Figure 4.3d). These results, combined with those of Zoback and Beroza (1993) for the diverse aftershock focal plane mechanisms of the Loma Prieta earthquake (Figure 4.2) provide convincing evidence that S_{Hmax} orientations are consistently at an angle of $>80°$ to the local strike of the San Andreas or Calaveras faults. Importantly, the stress orientation estimates in each case are indicative of conditions within 5–10 km of the respective faults, thus indicating fault-normal compressive stress within the crustal volumes adjacent to the seismogenic sections of the San Andreas and Calaveras faults.

Four S_{Hmax} estimates obtained from borehole breakout data and shown in Figure 4.2 reinforce the picture of fault-normal compression in the San Francisco Bay area. That

[2] In this and the following chapters, principal stress magnitudes and orientations are differentiated by the use of italics for magnitudes and plain fonts for orientations.

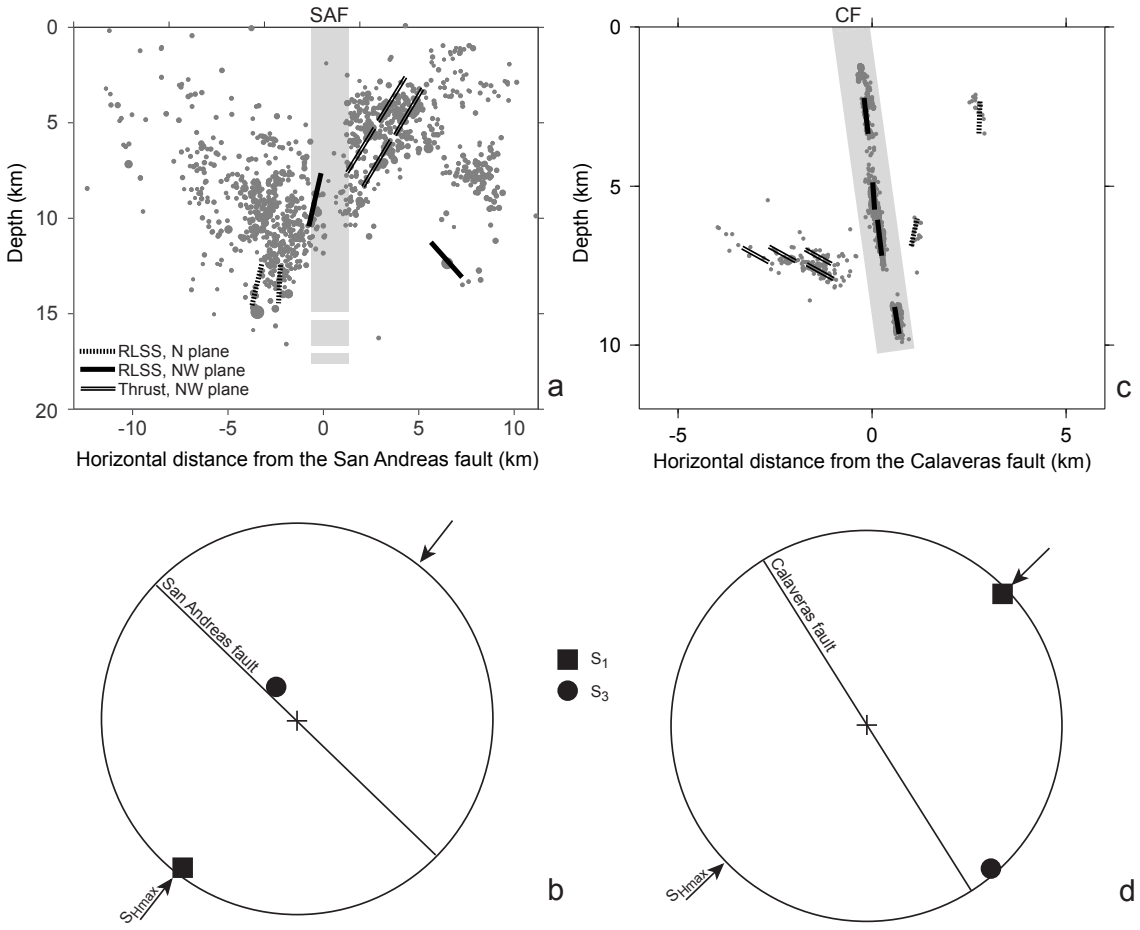

Figure 4.3: Cross-sections of seismicity and stress inversion results for the San Andreas fault on the southern San Francisco Peninsula and the Calaveras fault in the vicinity of the 1984 Morgan Hill Earthquake. See text for details. RLSS — right lateral strike-slip.

both the San Andreas and Calaveras faults are able to slip under near-field fault-normal compression indicates that they are very weak with respect to hydrostatic Byerlee's law.

4.4 Stress Inversions in Southern California

As alluded to above, Hardebeck and Hauksson's (1999) gridding method results in widely separated focal mechanisms being combined for stress inversion. The essential limitation of this method is that it takes no account of either structural trends (other than the average

strike of the SAF) or earthquake clustering. To determine whether Hardebeck and Hauksson's grid design adversely affects stress inversion results in southern California, we have opted to use a recursive quadtree algorithm to grid the data. Starting from a single square box encompassing all the earthquake locations, the algorithm operates by dividing the box into quarters and continuing recursively within each quarter until there are fewer than $n_{\max}$ earthquake locations in each box or the box reaches a minimum dimension of $x_{\min}$. The latter condition is a modification of the standard quadtree algorithm that we have incorporated to avoid boxes that are smaller than realistic errors in the earthquake locations. The resultant grid comprises an irregular mesh of square boxes that are smaller and more densely spaced in regions containing many earthquakes. In practice, we impose an additional condition that restricts the stress inversion to those boxes containing more than $n_{\min}$ events. We feel that this gridding scheme is geologically reasonable because it combines earthquakes within contiguous crustal volumes of limited extent.

In order to compare our results directly to those of Hardebeck and Hauksson (1999), we have used the same data set and stress inversion method. The data set contains first-motion focal mechanisms for approximately 49,000 earthquakes recorded by the southern California seismic network between 1981 and 1999 and relocated using a three-dimensional velocity model (Hardebeck and Hauksson, 1999; Hauksson, 2000). We use the Michael (1984, 1987) stress inversion method with equal weighting of both nodal planes.

Figure 4.4 illustrates the results for southern California obtained by inverting the entire data set after gridding with the parameters $n_{\min} = 30$, $n_{\max} = 100$, and $x_{\min} = 5$ km. Note that this procedure produces square boxes of $\sim$5.6 km width in regions of dense seismicity, such as the vicinities of the Northridge and Landers earthquakes (denoted by N and L respectively) and boxes of 5.6–22 km width along the SAF. Within the Mojave Desert, the triangular fault-bounded region in the middle of Figure 4.4, the average box size is $\sim$44 km, reflecting the relatively sparse seismicity. We are confident that the gridding methodology is robust because the S_{Hmax} orientations in adjacent boxes are very similar despite each focal mechanism inversion calculation being performed independently of those surrounding it (see Section 5.3 for comparison of these results with other stress indicators).

In general, S_{Hmax} trends slightly east of north and is oriented at a high angle to the fault strike of each major fault strand illustrated. Figure 4.5 illustrates the near-field stress

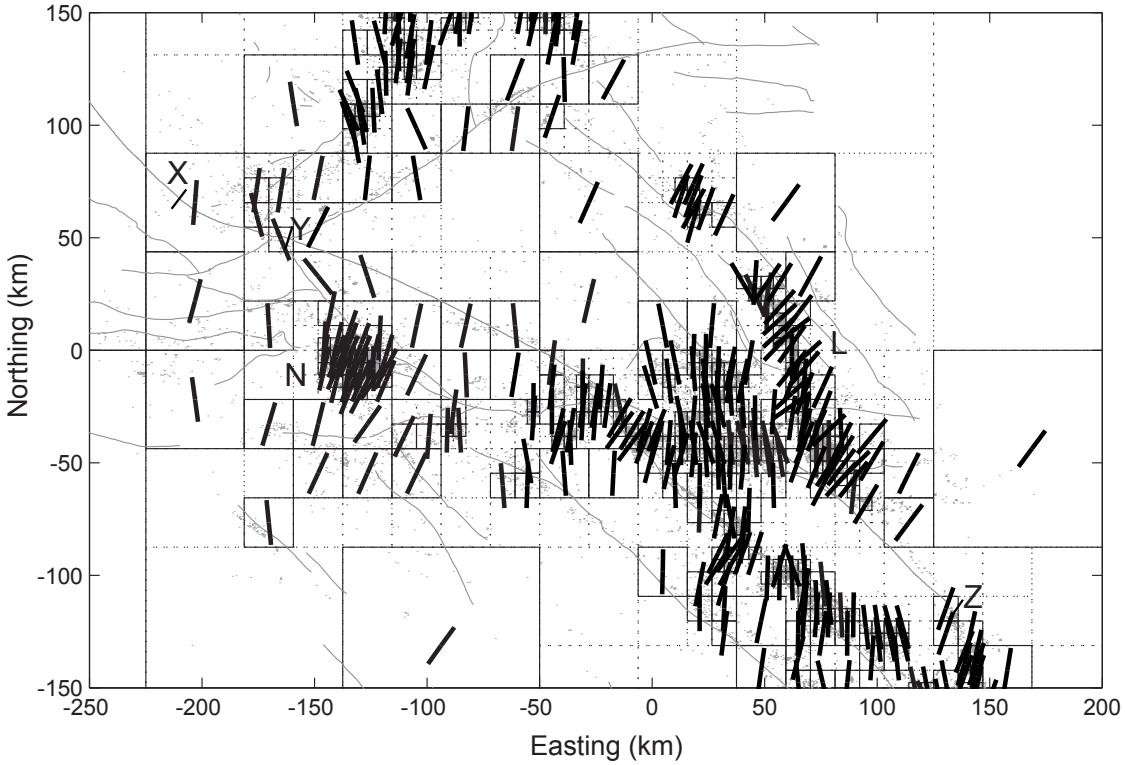

Figure 4.4: (a) S_{Hmax} orientation results obtained using the quadtree gridding algorithm and the Michael (1984, 1987) stress inversion routine. Boxes containing fewer than 30 focal mechanisms are dashed, and no inversion was made at those locations. L, N — areas of seismicity associated with the 1992 Landers and 1994 Northridge earthquakes respectively. X, Y, Z — trace of the San Andreas fault profile illustrated in Figure 4.5.

orientation data — those data points closer than 5 km to the fault trace — along the San Andreas fault. The mean and standard deviation of the angle between S_{Hmax} and the local fault strike are 64° and 14° respectively, indicating that the near-field angle is significantly different at the 95% level of confidence from that suggested by Hardebeck and Hauksson (1999) for some of their profiles and later utilized by Scholz (2000) to argue for a strong San Andreas fault. This result agrees, however, with that of Jones (1988), who found that the mean angle exceeded 60°. Contrary to Hardebeck and Hauksson (1999), we do not observe a consistent pattern of stress rotation close to either the SAF or the other major faults.

We have also investigated the effect of the 1992 Landers earthquake on the local stress

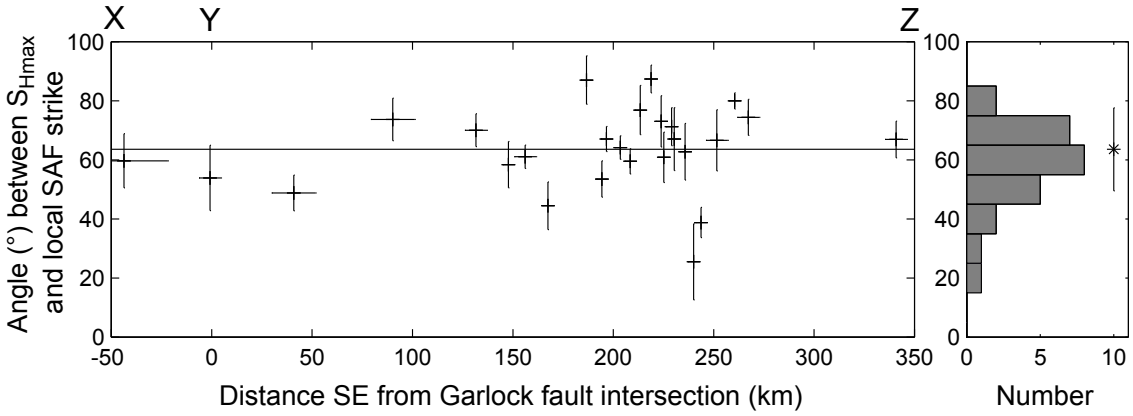

Figure 4.5: Along-fault profile (X–Y–Z, Figure 4.4) and corresponding histogram of the angle between near-field S_{Hmax} estimates (lying within 5 km of the San Andreas fault trace) and the local fault strike. The horizontal error bars indicate the width of the box used for each inversion, and the vertical error bars indicate the 95% confidence bounds estimated by bootstrap analysis. The mean of all estimates (64°) is indicated by the solid horizontal line. The mean and standard deviation (14°) are indicated in the histogram by the star and vertical error bars respectively.

field. Using a relatively simple approach, we have inverted the focal mechanisms before and after the event separately to determine whether or not any appreciable stress rotation is evident (Figure 4.6a). The nature of the quadtree algorithm means that the grids corresponding to different data sets are not necessarily the same, implying that the pre- and post-earthquake stress inversions are made at different locations. Thus, we have only compared the two data sets at locations less than 5 km apart. The comparisons were made separately inside and outside the zones of pronounced aftershock activity (defined by areas of aftershock activity occurring within 30 days of the main shock). This distinction is made on the presumption that the occurrence of aftershocks (the "aftershock zone") implies a possibly significant stress perturbation, whereas a lack of aftershock activity implies no significant earthquake-induced change. Thus, the latter case constitutes a control zone in which we expect to observe no rotation if the methodology is appropriate.

It is qualitatively apparent from Figure 4.6a that there is little systematic difference in the pre- and post-Landers stress orientations. This observation is substantiated in Figures 4.6b and 4.6c, which compare the differences in orientation in the control zone (mean,

-0.8°; standard deviation, 12.2°; 46 observations) and aftershock zone (mean 1.4°; standard deviation, 12.7°; 19 observations). Neither of these samples is significantly different from zero at the 95% level of confidence. Both standard deviations are similar to those obtained for the southern California data set as a whole, and suggest that small earthquake-induced rotations are unlikely to be observed given the stress uncertainties.

4.5 Discussion

The data from both the San Francisco Bay area and southern California reveal high angles between the local fault strike and the direction of maximum horizontal compression. Indeed, this observation applies both to the SAF and to the adjacent major faults, and suggests that weakness is characteristic of these portions of the North America–Pacific plate boundary.

The discrepancies between our southern California results and those of Hardebeck and Hauksson (1999) presumably stem from the different gridding methodologies used, as the data set and focal mechanism inversion procedures were the same. By using an iterative gridding algorithm that incorporates spatial variations in seismicity, it has been possible to obtain a high-resolution image of near-fault stress orientations — where justified by the data — without needlessly compromising the assumption of local stress homogeneity. Our results are incompatible with Scholz's (2000) model, which predicts symmetric rotation about the SAF over lateral distances of ± 20 km. We have particularly strong reservations about the applicability of a two-dimensional plane-strain model to a segment of the SAF that is clearly curved and, moreover, intersects another large fault. It is noteworthy that the only data presented by Hardebeck and Hauksson (1999) that are satisfactorily fit by the Scholz model are those from the complex "Big Bend" area.

The significance of our results is that any postulated stress rotation must occur within a zone no more than several kilometers wide, centered on the fault zone, or otherwise it would be detectable. Any such zone must be narrow, on theoretical grounds, or the fluid pressure would overcome the least principal stress and hydrofracture the surrounding crust (Rice, 1992). As pointed out by Scholz (2000), Hardebeck and Hauksson's (1999) 20–30 km-wide zone of stress rotation is inconsistent with the Rice (1992) model of a high-pressure

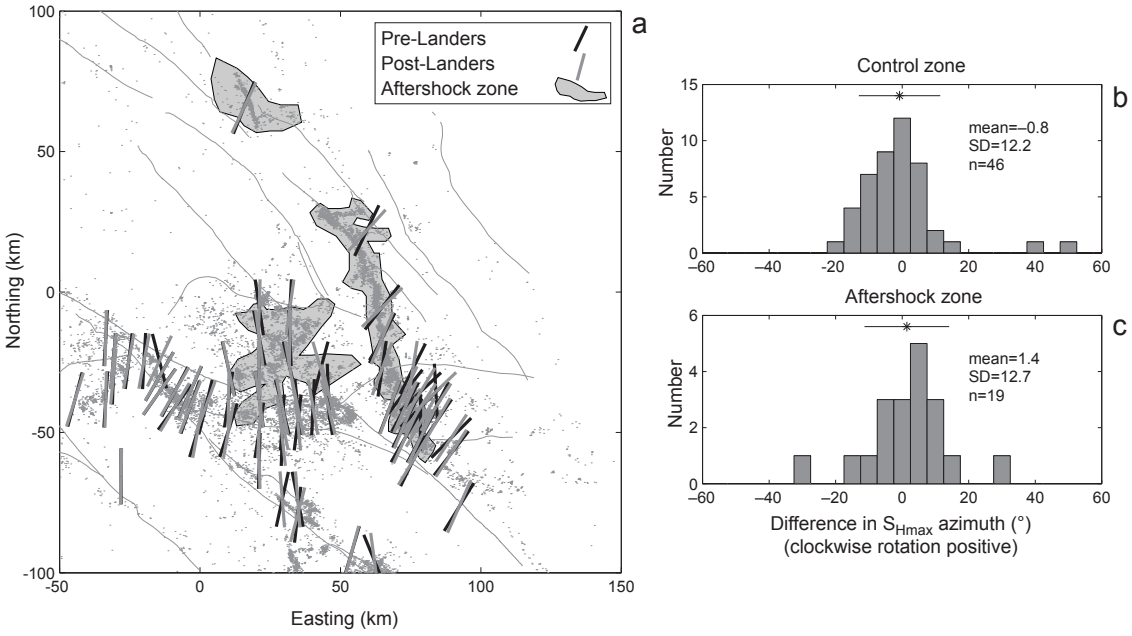

Figure 4.6: (a) S_{Hmax} orientations before (black) and after (grey) the Landers 1992 earthquake. The light grey shaded regions indicate regions of aftershocks. (b) Histogram of differences in pre- and post-Landers stress orientations outside the zones of aftershock activity. The values plotted are the post-Landers orientation minus the pre-Landers orientation; clockwise rotations are positive. The mean (–0.8°) and standard deviation (12.2°) of the 46 data points are illustrated by the star and horizontal error bar respectively. (c) Histogram of stress orientation differences within the aftershock zone.

fault core. While our data do not possess sufficient resolution to observe stress rotations on the scale of $\sim$1 km, it is clear that S_{Hmax} is oriented at a much higher angle to the fault strike within $\pm$5 km of the SAF than is consistent with conventional Coulomb faulting and hydrostatic Byerlee's law. In other words, these data clearly illustrate that the fault has low frictional strength.

4.6 Conclusions

We have compiled stress orientation data in the San Francisco Bay area and reanalyzed stress orientations in southern California using focal mechanism data. In the San Francisco Bay area, focal mechanism stress inversions indicate that the maximum horizontal

compressive stress is oriented almost orthogonally to the strikes of the San Andreas and Calaveras fault. Using the same data set and inversion methodology as Hardebeck and Hauksson (1999) we have demonstrated that their postulated near-fault stress rotation may be an artifact of combining widely separated focal mechanisms into single inversions. Using a geologically reasonable and mathematically more sophisticated gridding algorithm which takes into account the spatial clustering of seismicity, we have been able to obtain stress orientations while justifying to the extent the data warrant the assumption of stress homogeneity within contiguous crustal blocks. Furthermore, applying this technique to the 1992 Landers earthquake reveals no consistent differences in stress orientation before and after the main shock.

Overall, available stress orientation results from the San Francisco Bay area and southern California strongly indicate low levels of shear stress on planes parallel to the San Andreas fault. In the San Francisco Bay area, several data are available within ± 5 km of the main fault zone that indicate a direction of maximum horizontal compression nearly orthogonal to the San Andreas and Calaveras faults, and the fault which produced the Loma Prieta earthquake. In southern California, the direction of maximum horizontal stress near the San Andreas is generally at a high angle to the fault (averaging more than 60°), similarly indicating that the fault has low frictional strength.

Acknowledgments

We are grateful to D. Schaff and G. Beroza for making their Calaveras fault earthquake relocation data available, S. Prejean for valuable suggestions, M. L. Zoback for the San Francisco Peninsula seismicity data, and to D. Cowan and P. Sammonds for considerate reviews. Supported by the National Science Foundation (award 96-14267) and an Arco Stanford Graduate Fellowship.

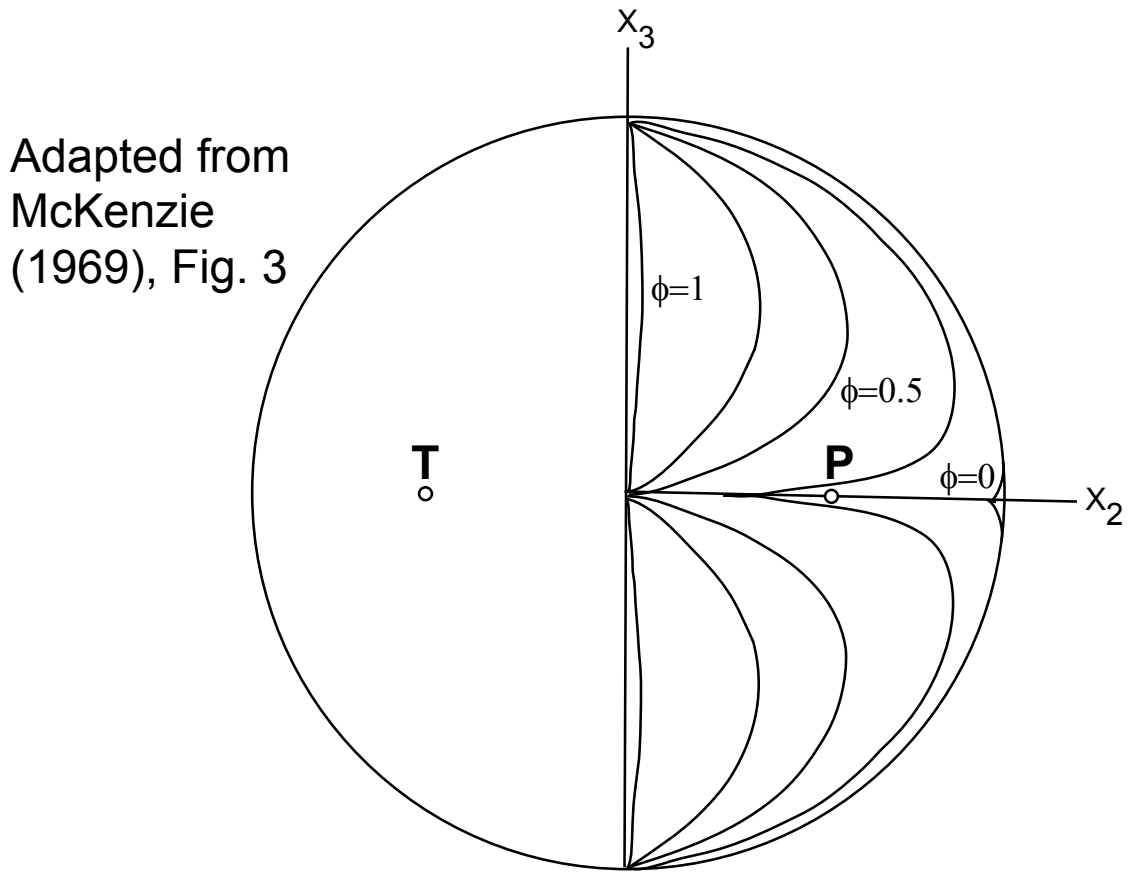

Figure 4.7: Single focal mechanism constraints on the stress tensor; (after McKenzie, 1969). S_1 may lie anywhere to the right of the labelled curves, depending on the stress ratio $\phi = (S_2 - S_3)/(S_1 - S_3)$. If $\phi = 1$, the only constraint imposed by this focal mechanism on the causative stress tensor is that S_1 lie within the dilatational quadrant; conversely, if $\phi = 0$, then S_1 must lie along the axis labelled x_2.

4.7 Appendix: Focal Mechanisms and Stress Inversion

McKenzie (1969) demonstrated that a single focal mechanism imposes only minimal constraints on the orientation of the causative stress tensor. Specifically, in the absence of any prior information about the relative magnitudes of the principal stresses, all that can be said based on a single focal mechanism is that the axis of greatest compressive stress (S_1) lies within the dilatational (P) quadrant (Figure 4.7). The issue of focal mechanism diversity is expected to become more acute the closer one focuses on a major fault such as the SAF,

where on-fault earthquakes tend to exhibit very similar focal mechanisms and the information about stress directions contained in a suite of focal mechanisms may differ little from that implied by a single mechanism. In such circumstances, both the Gephart and Forsyth (1984) and Michael (1984, 1987) stress inversion algorithms tend to return the average P axis of the focal mechanisms as S_1 with very small confidence intervals (Figure 4.8). Consequently, when focal mechanism diversity is very low, the estimate of the stress tensor's orientation obtained with either of these algorithms may appear to be reliable but in fact be completely misleading.

This issue is particularly problematic when fault strength and, specifically, the orientation of the crustal stress tensor with respect to a major fault are being considered. Provost and Houston (2001) found that S_{Hmax} was oriented almost perpendicularly to the SAF in central California except within 1 km of the fault's surface trace, where it was found to lie at β=45°. This result, which implies very localized stress rotation, should be interpreted carefully in light of the fact that β=45° is the expected result when low focal mechanism diversity causes the stress inversion algorithm to return a degenerate solution. Although 45° *might* be the correct answer, it is also the expected wrong answer.

Figure 4.9 shows P and T axis data and the corresponding S_{Hmax} results at 20 randomly selected locations in southern California. The level of focal mechanism diversity revealed by variations in the P and T axes is qualitatively similar close to and far from the SAF. The high degree of consistency between stress orientations determined from focal mechanisms and those determined using borehole data (as illustrated, for example, in Figures 4.2 and 5.1–5.3, below, and more generally by Figure 1.1) suggests that, in general, adequate diversity exists in the focal mechanism data used here to produce reliable, repeatable stress orientation results. This conclusion is reinforced by the fact that we observe a much higher angle (68°) between S_{Hmax} and the local strike of the SAF than the 45° expected if low focal mechanism diversity were causing problems with the inversion algorithm of the sort illustrated in Figure 4.8.

While we have not yet developed a satisfactorily objective method of identifying unacceptably low focal mechanism diversity, or of incorporating this factor in the stress axis uncertainties more rigorously, we have investigated one possible approach and applied it to stress orientations along the San Jacinto fault in southern California (Figure 4.10). In this

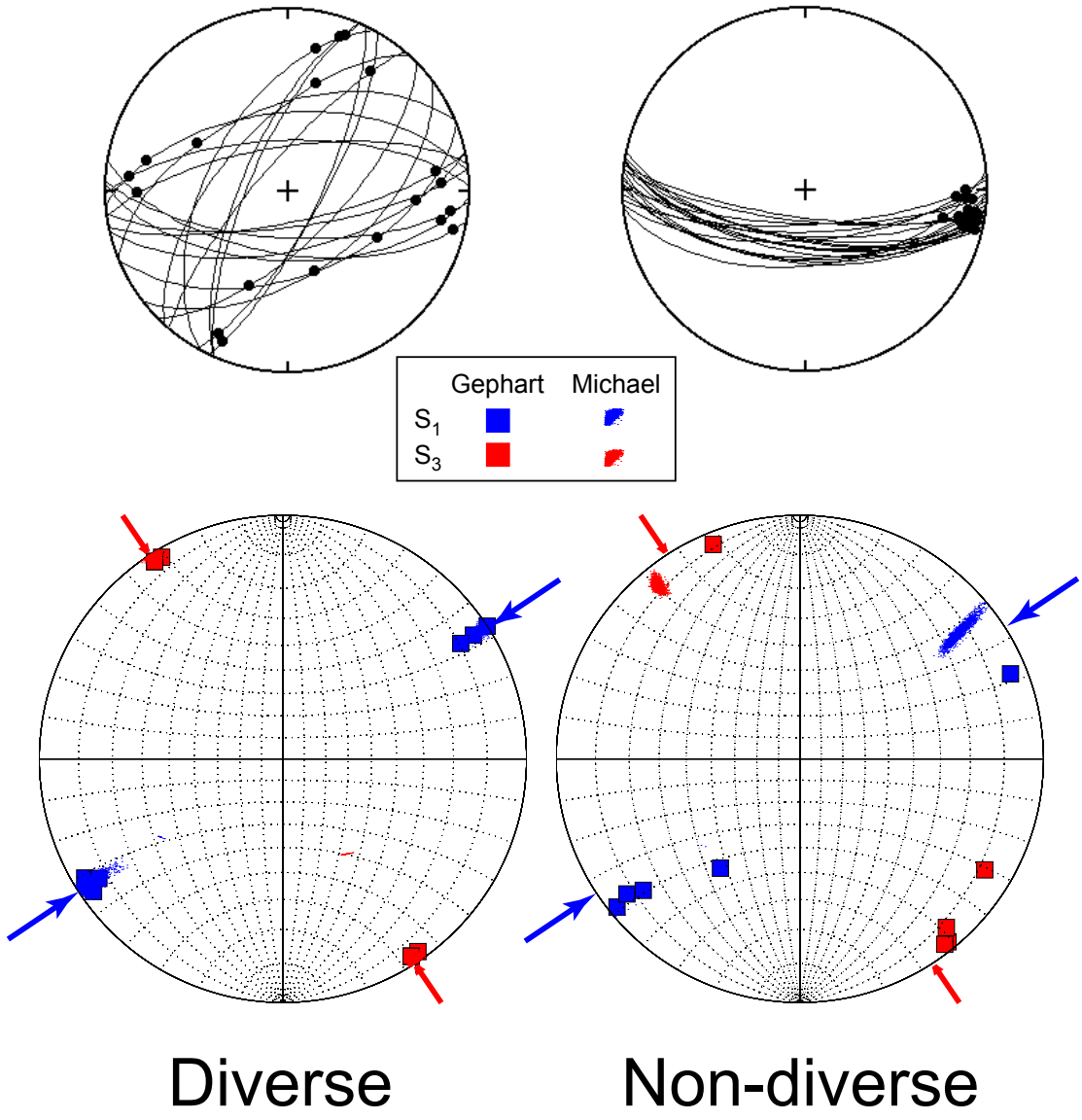

Figure 4.8: Effects of diversity on stress inversion results. The two synthetic focal mechanism data sets have similar average P and T axes, despite containing different fault populations. Inverting the diverse (left-hand) suite of mechanisms yields a well-constrained solution. Figure 4.7 suggests that an inversion of the non-diverse (right-hand) data should yield a broad, symmetric distribution of suitable S_1 orientations throughout the dilatational quadrant. Instead, both the Gephart and Forsyth (1984) and Michael (1984, 1987) inversion algorithms return a tightly constrained S_1 axis that does not reflect the physical constraints imposed by the data.

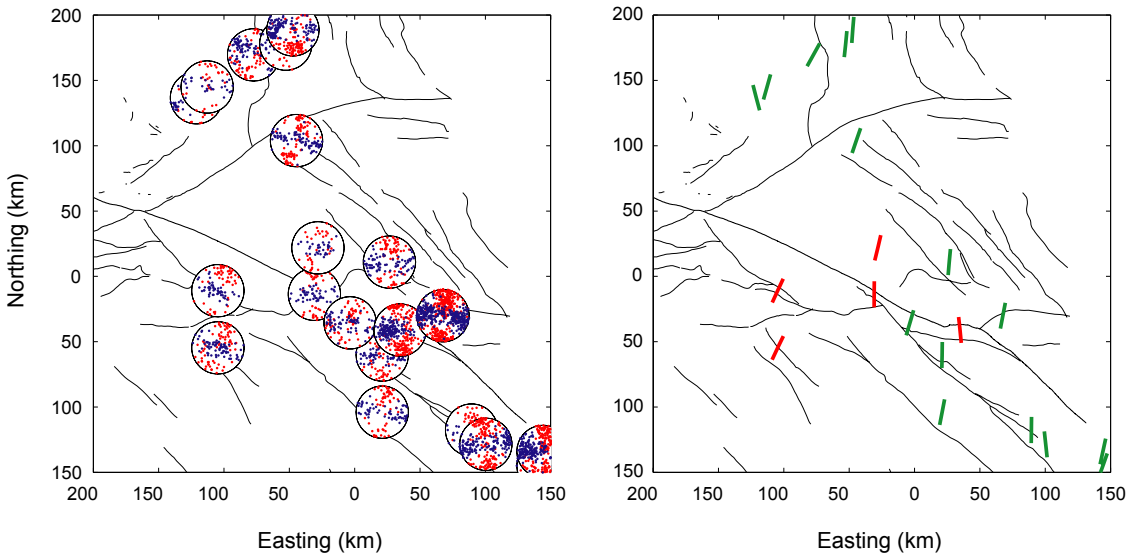

Figure 4.9: Representative P–T plots (left) and S_{Hmax} directions (right) at 20 randomly selected locations in southern California. The P and T axes are indicated on stereonets by red and blue dots respectively; the corresponding S_{Hmax} axes are illustrated as either red (reverse) or green vectors (strike-slip).

area, S_{Hmax} is generally oriented at a high angle to the fault's surface trace ($\beta \sim 60^{\circ}$), but exhibits a clear rotation to values as low as 40° within a region of low seismicity known as the Anza Gap (Thatcher et al., 1975). Variations in β appear similar to those observed in a profile of fault-parallel shearing moment (M_{FPS}), suggesting that higher fault strength within the Anza Gap is related to a surfeit of seismicity.

Based on the comments above, it is clear that this signal might simply be an artifact caused by lower focal mechanism diversity within the low-seismicity region. To address this issue quantitatively, we have calculated an unbiased estimate of focal mechanism diversity, given by

$$D = \sum_{n=1}^{N} \left(M_{ij}^{n} - \bar{M}_{ij}\right)\left(M_{ij}^{n} - \bar{M}_{ij}\right)/N \tag{4.1}$$

where M_{ij}^{n} is the unit moment tensor corresponding to the nth focal mechanism and $\bar{M}_{ij}$ is the average moment tensor of the N events. This diversity parameter is somewhat similar to the variance of a sample, being the sum of squared differences about a common mean;

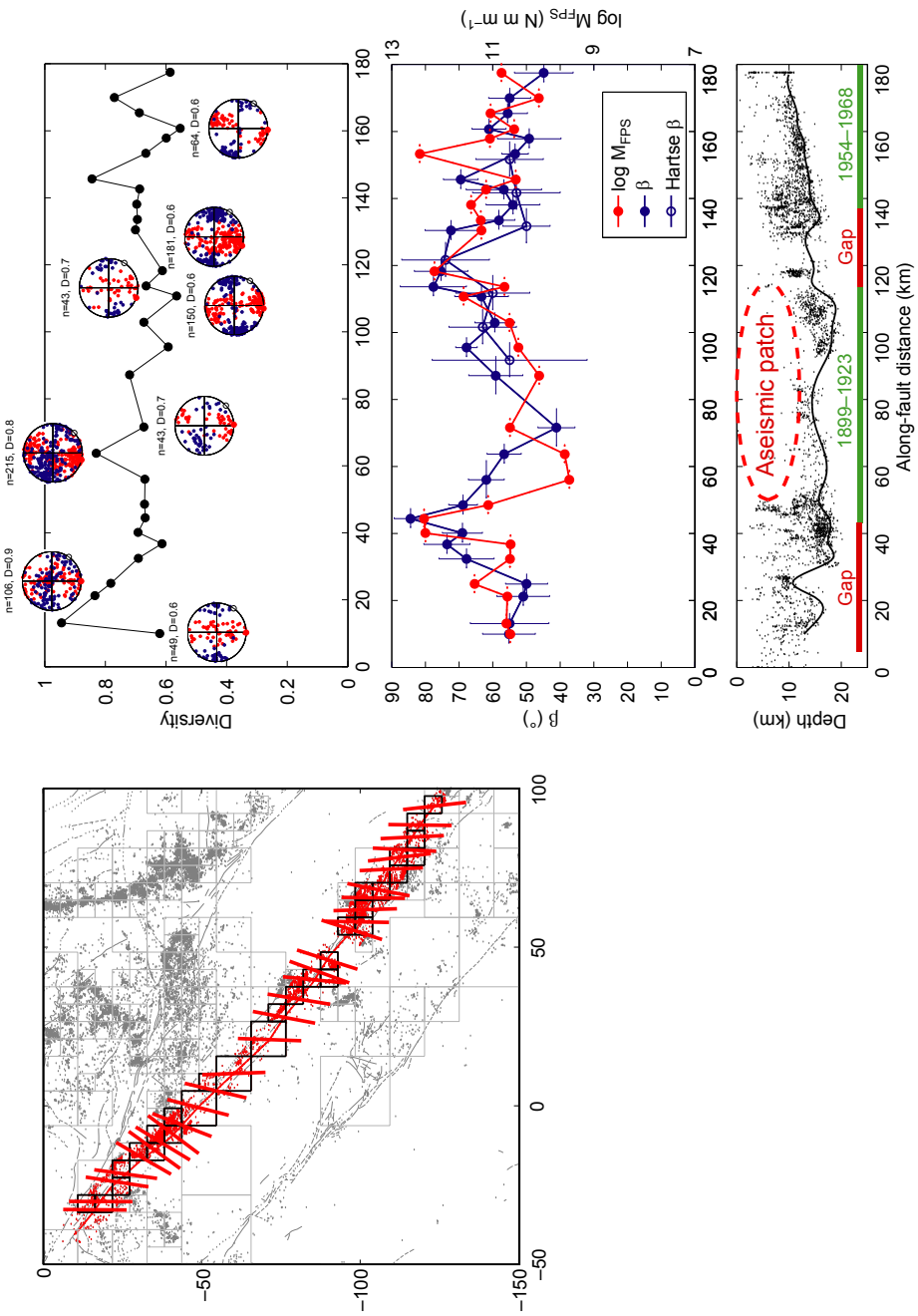

Figure 4.10: Stress, seismic moment, and focal mechanism diversity along the San Jacinto fault. The map illustrates near-field stress orientations along the San Jacinto fault in southern California near the Anza Gap (Thatcher et al., 1975). The stereonets in the top right-hand panel illustrate representative P (red) and T axes (blue). See text for further details. "Hartse β" — S_{Hmax} data obtained by Hartse et al. (1994) by focal mechanism inversion.

D varies between 0 (when each focal mechanism is the same) and 1 (for *N* randomly distributed mechanisms). No clear variations in diversity are observed near the Anza Gap, suggesting that the low value of β is not a simple consequence of lower focal mechanism information. Further work is required to substantiate this result, however, and to determine what value of *D* corresponds to an acceptable level of focal mechanism diversity.

We conclude that problems related to low focal mechanism diversity have not arisen in this study; however, it is clear that a better method of incorporating the weak constraint imposed by each focal mechanism on the stress tensor into reliable estimates of stress axis uncertainties is required.

Chapter 5

Crustal Dynamics of the San Andreas Fault System[1]

San Andreas Fault
moved its fingers
through the ground
earth divided
plates collided
such an awful sound

Natalie Merchant
SAN ANDREAS FAULT

5.1 Abstract

Throughout central and southern California, the relatively uniform NNE–SSW compressive stress field described in Chapter 4 is remarkably consistent with the superposition of stresses arising from lateral variations in lithospheric buoyancy in the western United States, and far-field Pacific–North America plate interaction. At regional scales, the tectonic stress field is not affected by the San Andreas fault (SAF). Thus, while GPS data

[1] Sections 5.5 and 5.6 previously published in part by Zoback et al. (2002).

reveal that crustal velocities adjacent to the SAF are consistent with localized plate kinematics, crustal stresses seem to be controlled by relatively far-field processes. Near the SAF ($\pm$10 km), however, the regional stress field is slightly perturbed and we observe an approximately constant angle between the fault and the maximum horizontal stress direction. Along $\sim$400 km of the SAF in southern California, this angle is $68\pm7^\circ$, indicating that the fault has low frictional strength. In central California, the corresponding angle is as much as 85°, implying extremely low fault strength.

We interpret these observations in terms of the simple conceptual model described in Chapter 3, in which the entire lithosphere is in steady-state failure equilibrium — brittle failure in the upper crust and ductile creep in the lower crust and upper mantle — in response to finite, buoyancy-related plate tectonic forces. Because regions of higher heat flow are characterized by low effective viscosity in the lower crust and upper mantle, the available plate-driving forces are sufficient to cause faster creep at depth (and higher seismicity rates in the overlying brittle crust) than in regions of lower heat flow. We suggest that the current debate over whether intraplate deformation is best viewed in terms of a deforming continuum or as rigid crustal blocks separated by relatively narrow fault zones may be a false dichotomy. We illustrate this for the Coast Ranges and Central Valley of western California. In the Coast Ranges, a region of high heat flow, high deformation rates are expected because of correspondingly high temperatures in the lower crust and upper mantle. The adjacent Central Valley is characterized by very low heat flow and deforms at such a slow rate that it appears to behave as a rigid block.

5.2 Introduction

The state of stress within the crust arises from distinct sources acting at a variety of scales (Zoback and Zoback, 1991; Zoback, 1992). The observed long-range (1000–5000 km) uniformity of stress orientations and relative magnitudes in intraplate regions suggests that plate-driving forces provide the largest component of the total stress field (Zoback et al., 1989; Zoback, 1992, Figure 1.1). In some areas, including the western United States, stresses caused by lateral variations in crustal buoyancy appear to provide a large component of the horizontal stress field (Fleitout and Froidevaux, 1982; Jones et al., 1996).

It has been realized for some time that stress orientations along the SAF (Mount and Suppe, 1987; Zoback et al., 1987; Jones, 1988; Townend and Zoback, 2001) and the lack of a distinct heat flow anomaly at the trace of the fault (Brune et al., 1969; Lachenbruch and Sass, 1980, 1992; Lachenbruch and McGarr, 1990) indicate average shear tractions less than 20–25 MPa in the seismogenic upper crust (Lachenbruch and Sass, 1992). These observations are difficult to reconcile with typical frictional coefficients of common rock types (μ=0.6–1.0) such as are determined in laboratory settings (Byerlee, 1978) or inferred from deep borehole stress measurements (Townend and Zoback, 2000), which suggest shear tractions approximately five times as large (see Chapter 2). High frictional coefficients (commonly referred to as "Byerlee friction") imply an angle (β) between the axis of greatest horizontal compression, S_{Hmax}, and the strike of a vertical strike-slip fault such as the San Andreas of 30–35°. Instead, what has been typically observed throughout California (Chapter 4) is a much larger angle that indicates near fault-normal compression in some places, observations that are especially noteworthy when the data come from crustal volumes immediately adjacent to the SAF (Jones, 1988; Oppenheimer et al., 1988; Zoback and Beroza, 1993; Townend and Zoback, 2001).

5.3 Stress and Crustal Velocity Data

5.3.1 Southern California

Individual earthquakes provide only limited information on the crustal stress field (McKenzie, 1969), but under appropriate conditions, a suite of focal mechanisms may be used to determine the best-fitting orientations of the principal stress axes (Michael, 1984; Gephart and Forsyth, 1984). As described in Chapter 4, we have used a recursive gridding scheme to group earthquakes and determine stress orientations with spatial resolution as high as the local density of seismicity warrants (Townend and Zoback, 2001).

A map of southern California stress orientations that incorporates data from a variety of sources is shown in Figure 5.1. The plain black arrows indicate the direction of greatest horizontal compression (S_{Hmax}) determined using the gridding scheme mentioned above (Townend and Zoback, 2001), whereas the black symbols indicate S_{Hmax} orientations in

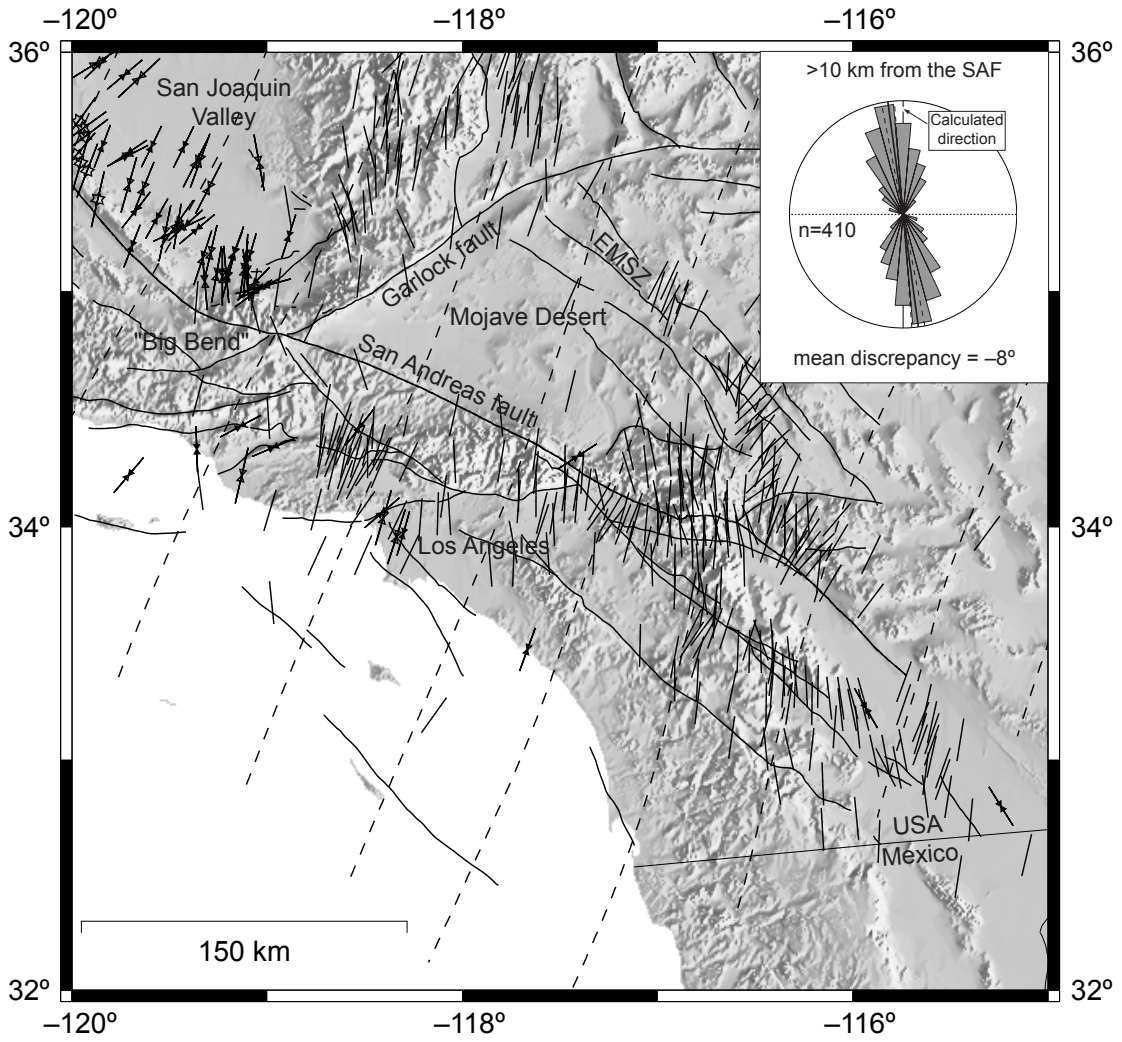

Figure 5.1: Orientation of the axis of greatest horizontal compression (S_{Hmax}) in southern California. The black symbols show S_{Hmax} directions determined from borehole breakouts (inward-pointing arrows), hydraulic fracturing experiments (stars), and earthquake focal mechanism inversions (plain lines, Fuchs and Müller, 2001; Townend and Zoback, 2001). The dashed trajectories show calculated regional S_{Hmax} directions from a model of lithospheric buoyancy and plate interaction (Flesch et al., 2000). The rose diagram summarizes the discrepancy between the observed and calculated stress orientations. See text for further details. EMSZ — Eastern Mojave shear zone.

the World Stress Map Database obtained from borehole breakouts and hydraulic fracturing experiments (Fuchs and Müller, 2001). As referred to in Chapter 4 and discussed in more

detail below, no significant stress rotations near the SAF are apparent. An independent study that incorporates focal mechanism uncertainties more rigorously (Abers and Gephart, 2001) substantiates this, and a similar finding of no major stress rotations near the SAF has also been reached by workers studying earthquakes in central and northern California (Provost and Houston, 2001; Schaff et al., 2002).

The dashed trajectories in Figure 5.1 are interpolations of S_{Hmax} directions calculated by Flesch et al. (2000) using a variational technique to estimate the minimum deviatoric horizontal stress field resulting from lateral variations in gravitational potential energy (also referred to as lithospheric buoyancy, and associated principally with the thermally elevated Basin and Range Province) and distributed deformation due to interaction between the North American and Pacific plates. The plate interaction stress field was calculated assuming an isotropic relationship between the principal stress and principal strain directions and ignoring strain data from within a 100 km-wide swath centered on the San Andreas fault where this assumption might be inappropriate. No in situ stress data were used in these model calculations.

Four important features of this map deserve specific mention: first, individual data sets produce remarkably consistent S_{Hmax} estimates at relatively fine scales, as demonstrated particularly well by the cluster of near-parallel stress orientations obtained by focal mechanism stress inversion of seismicity that occurred after the 1994 Northridge earthquake (-118.6°E, 34.3°N), in the southern Sierra Nevada (-117.8°E, 35.9°N), and eastern Mojave Desert (-117°E, 35.0°N). The clusters of borehole breakout and hydrofracture results in the southern San Joaquin Valley also demonstrate the consistency of nearby stress determinations. Second, the results obtained using different techniques generally agree very well, as demonstrated for the southern California region as a whole but particularly in the southern San Joaquin Valley and near Los Angeles (-118.4°E, 34.0°N). Third, at regional scales throughout southern California, S_{Hmax} exhibits a relatively uniform NNE–SSW orientation that is at approximately 60–70° to the direction of relative plate motion ($\sim$N40°W at this latitude). Finally, as indicated by the inset rose diagram, there is a remarkably good agreement between the observed regional stress field and that independently modeled by Flesch et al. (2000) using gravitational and far-field stress traction boundary conditions.

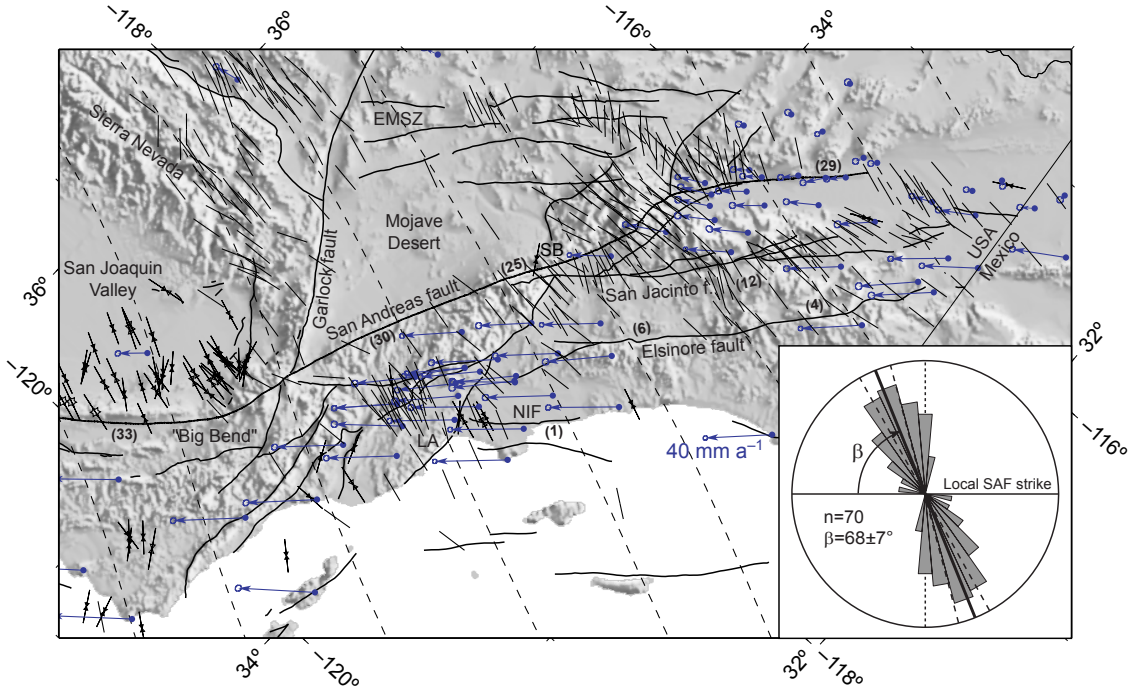

Figure 5.2: S_{Hmax} (black arrows), crustal velocity relative to stable North America (blue arrows), and average Quaternary fault slip rate data (parentheses, Petersen and Wesnousky, 1994) in an oblique Mercator projection about a pole similar to the North America–Pacific Euler pole (Argus and Gordon, 1991). See Figure 5.1 for an explanation of the different stress symbols. Inset: β values within 10 km of the SAF. See text for further details. LA — Los Angeles; NIF — Newport–Inglewood fault; SB — San Bernadino.

The rose diagram excludes data closer than 10 km to the SAF, which might exhibit a fault-related rotation with respect to the far-field S_{Hmax} direction and are considered separately below. For southern California as a whole, the calculations are systematically rotated by approximately 8° in a clockwise sense with respect to the observed stress directions.

In their modeling of the contributions of lithospheric buoyancy and internal plate deformation to the horizontal deviatoric stress field, Flesch et al. (2000) made no attempt to match in situ stress data, but the agreement between their computational results and the observed stress directions at regional scales is very good throughout most of California. Given that the frictional character of the SAF is neglected in the model — that is, there is no frictional interface in the model that corresponds to the SAF and imposes a constraint

on the local tractions — this concordance indicates that any such fault-related stress perturbation is relatively small in magnitude. We investigate below (Section 5.4) whether the presence of the SAF has a discernible effect on local stress orientations; in other words, whether the tectonic stress field adjacent to the SAF exhibits a fault-related component of stress superimposed on the two components included in Flesch et al.'s model.

The data shown in Figure 5.1 are presented in Figure 5.2 in an oblique Mercator projection about a pole similar to the North America–Pacific Euler pole (Argus and Gordon, 1991). At this latitude, the SAF strikes 4° counterclockwise of the predicted transform direction (DeMets et al., 1990). For the purposes of illustrating the geometrical relationship between the crustal stress field and the SAF, we have used a pole slightly different from the long-term Euler pole so that the SAF is drawn approximately parallel to the top and bottom edges of the figure. In this projection, the Pacific plate is moving straight to the left with respect to North America. The blue vectors illustrate crustal motions with respect to stable North America obtained between 1986 and 1997 by various groups under the auspices of the Southern California Earthquake Center (SCEC). Only those velocity vectors with a 95% confidence circle radius of $\leq$2 mm are plotted.

It is striking that the SAF is the principal locus of deformation despite undergoing a bend of $\sim$23° as it skirts the Mojave Desert. The Elsinore and Newport–Inglewood faults, and those comprising the eastern Mojave shear zone, do not accommodate such substantial components of plate motion, even though they are nearly parallel to the relative plate motion direction and apparently oriented at similar angles with respect to S_{Hmax} as the SAF. Some of the seismically active faults in the Landers region ($-$116.5,34.5) are also poorly oriented with respect to S_{Hmax}.

Figure 5.2 reveals clearly the high angle between the North America–Pacific relative plate motion vectors and the axis of greatest horizontal compression. To illustrate stress directions in the vicinity of the San Andreas fault, the rose diagram inset in Figure 5.2 summarizes estimates of β determined at 70 locations within 10 km of the SAF surface trace. The mean angle between S_{Hmax} and the local fault trace is 68$\pm$7°. S_{Hmax} is oriented at a relatively consistent angle to the SAF throughout southern California, a result also noted on the basis of a smaller data set by Jones (1988), suggesting that the stress field and fault geometry have evolved in a self-organized manner (see Section 5.4). If only the data

within 5 km of the fault trace are considered (34 data points), the corresponding orientation is essentially the same ($63\pm10^\circ$); a similar observation was made using only the 26 focal mechanism stress inversion results in Figure 4.5. Such high β angles are not compatible with Andersonian faulting theory incorporating Byerlee friction and hydrostatic fluid pressures; rather, they support the contention that the SAF is subject to a significant component of fault-normal compression and therefore slips at low shear/normal stress ratios.

In southern California, specifically along the section of the SAF that ruptured in the 1857 **M**8+ Fort Tejon earthquake, some authors (e.g., Hardebeck and Hauksson, 1999) have argued that S_{Hmax} rotates by 40° within ±20 km of the SAF. Based on a single profile across the SAF near the Big Bend, it has been suggested that the SAF might have higher frictional strength than the heat flow data seemingly permit (Scholz, 2000). However, it is clear from Figures 5.2 and 5.3 that the angle between S_{Hmax} and the SAF is inconsistent with Coulomb faulting theory and conventional Byerlee friction.

In order to quantify the magnitudes of stresses acting on the San Andreas fault, we assume that the crust adjacent to the SAF is critically stressed, such that differential stress increases with depth at a rate consistent with the failure of optimally oriented faults, hydrostatic fluid pressures and Byerlee friction (Chapter 2). In this case, the average differential stress in the seismogenic crust (evaluated at a depth of 7.5 km) is approximately 125 MPa and the average shear traction on the SAF in southern California is estimated to be 53–31 MPa (β=61–75°). The corresponding effective normal traction and shear/normal ratio are 158–180 MPa and 0.17–0.33 respectively.

It should be noted that there are several areas where the discrepancy between the observed (borehole or earthquake data) and calculated stress orientations is particularly marked. The majority of the locations with high discrepancies are in one of three distinct clusters: the Big Bend region near (-119.0°E, 34.8°N), north of the Garlock fault at (-118.5°E, 35.4°N), and near San Bernadino at (-117.7°E, 34.2°N). The Big Bend and San Bernadino "knots" both coincide with appreciable, localized bends in the strike of the SAF's surface trace; the San Bernadino cluster also corresponds to the southernmost rupture of the 1857 Fort Tejon earthquake (Jones, 1988). The Garlock cluster is at the east end of the source region of the 1952 Kern County earthquake (**M** 7.8), which Castillo and Zoback (1995) concluded to have substantially affected the local stress field.

5.3.2 Central California

An analogous map to Figure 5.2 for central California and the San Francisco Bay area is presented in Figure 5.3. Once again, borehole breakout data, hydraulic fracture data and focal mechanism stress inversion data reveal highly consistent S_{Hmax} orientations at adjacent locations, a high degree of correlation with the computed S_{Hmax} trajectories (Flesch et al., 2000), and a very high angle between the S_{Hmax} direction and the SAF ($\beta \sim 85^{\circ}$) along the San Francisco Peninsula and Calaveras fault. It is noteworthy that whereas the San Andreas fault accommodates most of the present-day strike-slip motion in central and southern California, in the San Francisco Bay area (and farther north) this motion is also taken up on the Hayward, Calaveras and San Gregorio faults, each of which appears to be as poorly oriented with respect to the contemporary stress field as the San Andreas.

This higher β angle of $\sim 85^{\circ}$ observed along the San Francisco Peninsula is particularly interesting because the stress data were obtained from boreholes and focal mechanism stress inversions as close as 1 km to the fault's surface trace (Townend and Zoback, 2001). Consequently, the ratio of shear to normal traction acting on the SAF in this area is very low: a similar conclusion has been reached for the Calaveras fault on the basis of high resolution seismic relocation results by Schaff et al. (2002). Performing an analogous calculation to that for southern California (above), we obtain an average shear traction of as little as 11 MPa along the San Francisco Peninsula (β=85°), an average normal traction of 187 MPa, and hence a shear/normal ratio of only 0.06.

5.4 The Mechanical Effect of the San Andreas Fault

The stress data reveal that strike-slip displacement along the San Andreas fault and subsidiary structures occurs at an angle of approximately 68° to the axis of greatest horizontal compression in southern California, and as high as 85° in central California. Moreover, in situ stress data and dynamical modeling results from southern and central California exhibit very good agreement in terms of the directions of the principal tectonic stresses. The data suggest, therefore, that the tectonic stress field does not "see" the San Andreas fault, in the sense that no major deflection of crustal stress trajectories in the vicinity of the fault

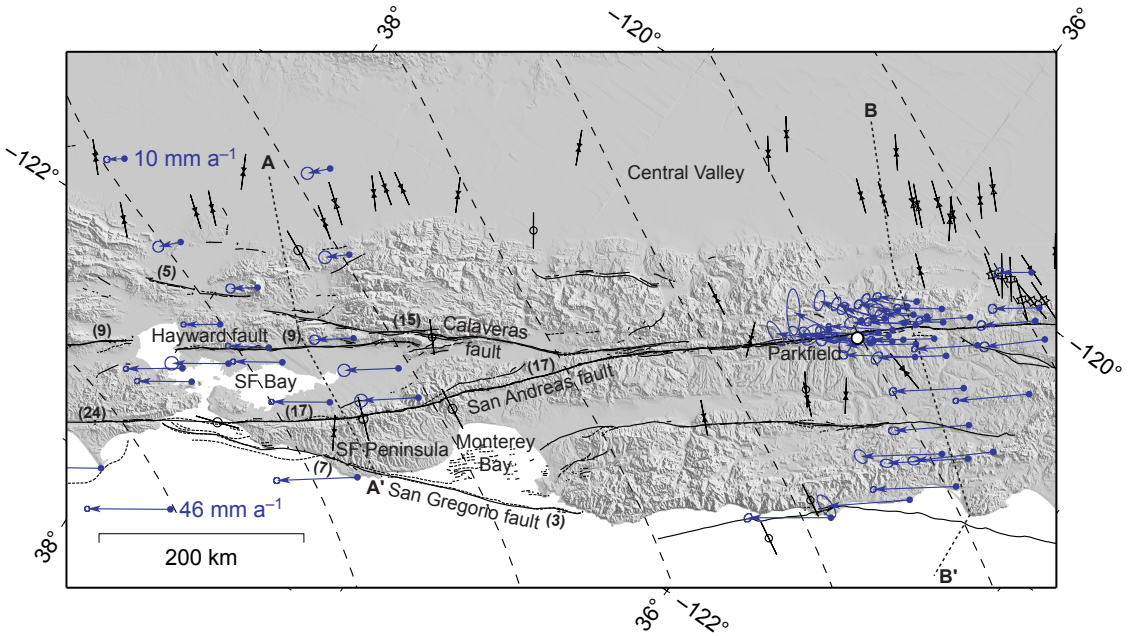

Figure 5.3: S_{Hmax} (black arrows) and geodetically determined crustal velocity data (blue arrows) from central California shown in an oblique Mercator projection about the North America–Pacific Euler pole (DeMets et al., 1990). The split circle symbols indicate World Stress Map earthquake focal mechanism inversions; all other symbols and the dashed trajectories are the same as in Figure 5.1. The numbers in parentheses are Quaternary fault slip rates (Working Group on Earthquake Probabilities, 1999). Cross-sections A–A' and B–B' are illustrated in Figure 5.6. SF — San Francisco.

is clearly discernible.

However, the fact that the angle between S_{Hmax} and the SAF remains approximately constant over a 400 km distance in southern California (Figures 4.5 and 5.2, inset), despite pronounced changes in the fault's strike, indicates a degree of interaction and self-organization. By this we mean that the fault's geometry exerts some influence on the nearby stress field, despite its weakness. If this were not the case, then the relatively uniform orientation of the regional stress field would result in β varying systematically with the fault strike.

An alternative method of demonstrating that the frictional characteristics of the SAF do affect nearby stress orientations is to compare average discrepancies between the observed and calculated stress orientations, close to and far from the SAF. The rationale here is

based on the diagrammatic equation shown in Figure 1.2. The Flesch et al. (2000) model contains only two sources of stress, gravitational potential energy variations, and far-field tractions necessary to account for distributed intraplate strain. In contrast, the observed stress field in the vicinity of the SAF may contain a third component related to the constraint imposed on the principal stress directions by friction. Therefore, if it can be demonstrated that the calculations adequately represent the observations away from the fault, where the contribution of the third term is expected to be minimal, then any additional discrepancy between the observations and calculations near the fault can be ascribed to the presence of the fault itself.

As indicated by the left-hand rose diagram in Figure 5.4 (which is also the inset in Figure 5.1), the average discrepancy between the observed and calculated S_{Hmax} directions further than 10 km from the San Andreas fault is approximately 8°, with the model exhibiting a systematic clockwise bias. However, within 10 km of the fault, the average discrepancy is 15°. We infer the slightly greater discrepancy adjacent to the fault to represent the fault's contribution to the total tectonic stress field, which is apparently manifest as a 7° anticlockwise rotation of the horizontal stress field. Given that the technique used to estimate the rotation is somewhat ad hoc and reliant on the presumed veracity of the model calculations, we do not place great emphasis on the significance of this 7° value. Rather, we suggest that by comparing observations with a plausible long-wavelength reference we have determined an approximate upper bound on near-field stress rotations. It is clear that improved estimates of the near-field stress rotation will require a better representation of the true stress direction uncertainties (cf. Section 4.7).

To summarize this section, the relationship of the San Andreas to the tectonic stress field in southern California is elucidated by three observations. First, the high average value of β ($68\pm7^\circ$) over a substantial distance ($\sim$400 km) indicates that the fault sustains low shear tractions and is weak. Second, because β exhibits no systematic variations with position along the fault, despite gradual variations in the far-field (regional) stress orientation and the local fault strike, the geometry of the fault and the geometry of the near-field horizontal stress field must be coupled; that is, the fault, though weak, does influence the stress directions locally. Third, a comparison of the near- and far-field discrepancies between the observed and calculated stress directions suggests that the SAF's mechanical influence is

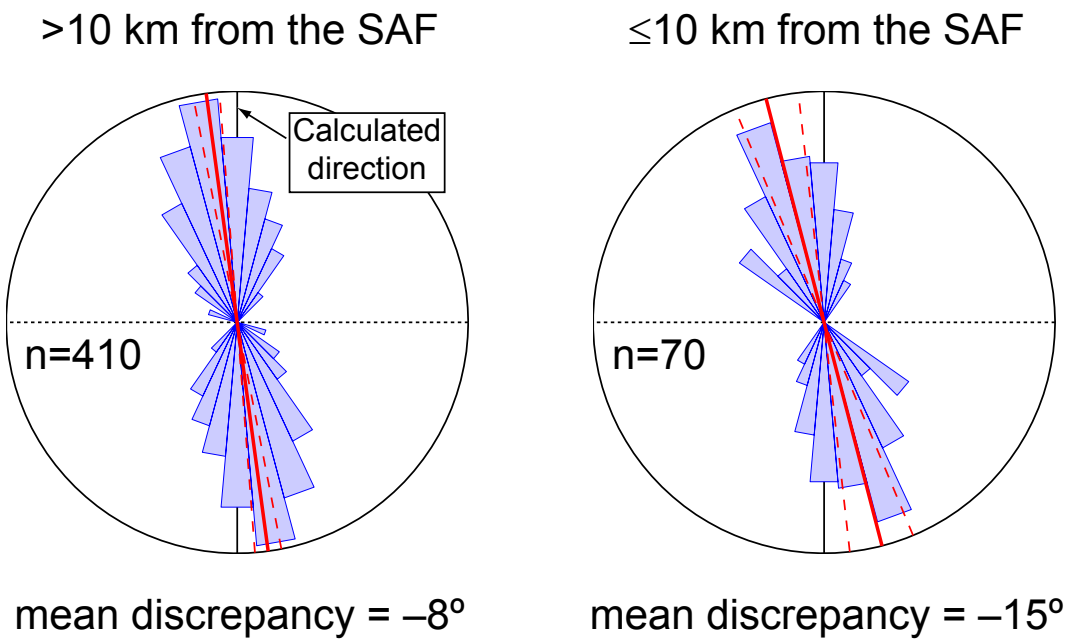

Figure 5.4: Near- and far-field discrepancies between the observed S_{Hmax} directions and the calculated directions of Flesch et al. (2000). In each rose diagram, the calculated stress direction is vertically upwards on the page.

equivalent to a small anticlockwise rotation of the nearby stress field, which the present data suggest is no larger than $\sim 7^{\circ}$.

5.5 Force-Limited Plate Tectonics

In the remainder of this chapter, we investigate faulting patterns and stress directions in central and southern California in terms of the mechanical framework for interpreting the deformation of intraplate lithosphere described in Chapter 3. Zoback et al. (2002) discussed the generalization of the intraplate model to consideration of more rapidly deforming areas, and coined the term "force-limited plate tectonics". Of particular relevance here is the question of whether the force-limited plate tectonic model, which is formulated in terms of stress and force, can be used to investigate the localization of strain.

5.5.1 Key Observations

The force-limited plate tectonic framework is based on a simple steady-state structural model of the lithosphere, illustrated in Figure 3.3. This model is in turn based on the key observations, which we recapitulate below, of (i) the existence of a frictionally controlled upper crustal stress guide, (ii) the finite magnitude of buoyancy-related plate tectonic driving forces and intraplate strain rates, and (iii) strain localization in response to the strong dependence on temperature of the rheology of the ductile lower crust and upper mantle.

As described in Chapter 2, in situ stress, permeability and fluid pressure measurements strongly suggest that a distinct population of fractures, namely those that are critically stressed, are responsible for maintaining both the strength and the hydraulic conductivity of the brittle upper crust. Briefly, the existence of such fractures implies that the crust is in a state of failure equilibrium in a manner analogous to a pile of sand. This inference, reached by interpreting direct measurements in terms of Coulomb frictional failure theory, is supported by the independent observation that very small increases in fluid pressure — in response to direct injection (Healy et al., 1968; Pine et al., 1983; Zoback and Harjes, 1997) or reservoir impoundment (Simpson et al., 1988; Roeloffs, 1996) — and coseismic stress changes (Stein et al., 1992, 1997) are sufficient to induce seismicity. Moreover, this state of friction-limited in situ stress has been observed almost everywhere that in situ data have been collected from depths of several kilometers in continental crust, and has been found without exception to be consistent with coefficients of friction of 0.6–1.0, such as are measured in laboratory experiments (Byerlee, 1978).

The frictional failure envelope provides an upper bound on allowable stress states. However, the fact that stress levels are similar and close to this bound in locations deforming at different strain rates suggests that assuming the brittle crust to be critically stressed provides a much better reference state of stress than achieved by assuming an isotropic "lithostatic state of stress" (in which all three principal stresses are equal to the weight of the overburden; McGarr, 1988), the "bilateral constraint" (in which the two horizontal stresses are equal and estimated based on an unreasonable assumption of purely elastic behavior; see Zoback and Zoback, 2002, for a critique), or by omitting ambient tectonic stress altogether from tectonophysical models.

One manifestation of high crustal strength is the efficient transmission of tectonic stress over distances of thousands of kilometers in intraplate regions, via what is in effect an upper-crustal stress guide. This was first observed in the conterminous United States and North America (Zoback and Zoback, 1980, 1989, 1991, Figure 1.1) and later on a global basis (Zoback, 1992). East of the western Cordillera, the direction of maximum horizontal stress measured throughout North America is remarkably consistent with the orientation of the plate-driving forces associated with the ridge-push force (Zoback and Zoback, 1991).

It has been generally concluded that the forces responsible for plate motions (and intraplate stress fields) are fundamentally associated with gradients in the density and thickness of the lithosphere (e.g., Forsyth and Uyeda, 1975; Jones et al., 1996; Flesch et al., 2000, 2001). What is key to the model described below is that the total force available to cause intraplate strain is limited to that provided by tectonic processes, rather than having an arbitrary value that depends on the chosen strain rate. As described in Chapter 3, several authors have estimated the total force available to cause relative plate motions at $1–5\times10^{12}$ N m^{-1} from considerations of tectonic driving forces (slab pull and ridge push), thrust-zone topography, and elastic plate deformation (Forsyth and Uyeda, 1975; Turcotte and Schubert, 1982; Bott and Kusznir, 1984; Kusznir, 1991).

At mid-crustal depths, temperatures are inferred to be sufficiently high that ductile failure mechanisms operate at lower differential stress levels than required for brittle faulting (Sibson, 1983; Chen and Molnar, 1983; Kohlstedt et al., 1995). It is probable that a transitional, semi-brittle mode of deformation occurs at mid-crustal depths; however, as will be seen below, we are interested in the overall size of the strength envelope as a function of depth, rather than its exact shape. Experimental data and thermodynamic considerations suggest that the appropriate constitutive relation for rocks in the ductile lithosphere is a power law of the form $\dot{\varepsilon} \propto \Delta\sigma^n$, where $\dot{\varepsilon}$ and σ are the strain rate and deviatoric stress, respectively, and n is a positive exponent (equation 3.14; see Chapter 3 for further details). If equation 3.14 is an appropriate relationship for describing the ductile lithosphere, as we are assuming it to be, then $\dot{\varepsilon}$ is nonzero for any nonzero differential stress; that is, the lower crust and lithospheric mantle fail, albeit perhaps at an extremely low rate, in response to any non-hydrostatic load.

5.5.2 Lithospheric Failure Equilibrium

If it is assumed that the brittle and ductile portions of the lithosphere are mechanically coupled, then one consequence of the brittle crust being critically stressed and the ductile lithosphere deforming in response to any applied differential stress is that the entire lithosphere is in a state of failure equilibrium. This does not mean that the lithosphere has zero strength; on the contrary, if it is both failing and sustaining plate tectonic loads, then the lithosphere's strength is equal to the magnitude of those loads. This is the crux of the force-limited plate tectonic model.

Our approach presumes that the net force exerted on the lithosphere is the same on all cross-sections through a plate, and neglects basal tractions. The general absence of large lateral gradients in either stress magnitudes or stress orientations in intraplate regions (Figure 1.1; Zoback, 1992) and lack of evidence for "residual stress" associated with past tectonic events (Zoback and Zoback, 2002) suggest that basal tractions are relatively small and further that the lithosphere does not contain marked variations in cross-sectional strength. We further simplify the model by only considering one-dimensional profiles.

By invoking the constraint that there is a finite force available to cause deformation (i.e. $\sim 3 \times 10^{12}$ N m^{-1}) and assuming that the upper crust, lower crust and lithospheric mantle are fully coupled, an average strain rate for the whole lithosphere can be estimated (Liu and Zoback, 1997). As discussed in Chapter 3, a large fraction of the net force applied to a plate is expended deforming the upper crust through faulting, and the remaining force is available to cause ductile deformation of the lower crust and upper mantle. Hence, stress levels in the upper crust are controlled by its frictional strength, and lithospheric strain rates are controlled by the remaining force and the rheological parameters of the ductile lithosphere.

Since the brittle crust's rheology is virtually independent of lithology, and because we are employing a single set of ductile flow parameters in this modeling, the key extrinsic parameter governing the distribution of lithospheric strength with depth is heat flow. By simply varying the amount of heat flowing through an idealized lithospheric section, the bulk strain rate required to satisfy the total strength constraint is found to vary greatly.

Figure 5.5 illustrates temperature and differential stress profiles for two end-member intraplate regions (which differ only in terms of their average surface heat flow) as well as the corresponding cumulative strength profiles and strain rates.

The red curves in Figure 5.5 correspond to moderately high heat flow (67 mW m^{-2}), and the blue curves to heat flow typical of a cold shield area (41 mW m^{-2}). In the former case, high temperatures in the lower crust and upper mantle mean that relatively little force is required to cause deformation there. In this case, most of the total tectonic force is carried by the strong brittle crust. In contrast, the low heat flow example illustrated here requires that much of the strength of the lithosphere be provided by the lower crust and upper mantle, which deform at the minuscule strain rate of $\sim 10^{-29}$ s^{-1}. This is a negligible rate (even over billions of years!) and thus consistent with a rigid plate assumption.

Although the sharp "nose" in the strength profiles at mid-crustal depths is rather nonphysical in light of likely semi-brittle deformation processes, as long as these processes do not dramatically alter crustal strength, the cumulative area under the curve will not be altered significantly. The model predicts that the brittle–ductile transformation occurs at a shallower depth in the colder example, although at a minuscule strain rate. The brittle-ductile transition is controlled by temperature in both cases, as in standard models of the seismogenic zone (e.g., Chen and Molnar, 1983; Sibson, 1983), but the strain rates at which the ductile yield stress is calculated differ and hence the depth of the transition varies too. In practice, this effect is unlikely to be observed in terms of maximum seismogenic depths, since the strain rate effects are likely to be overwhelmed by variations in crustal structure and regions as cold as modeled here would be expected to be completely aseismic. Moreover, the more complicated lithospheric structure in California than presumed in our intraplate-based, one-dimensional model means that the heat flow vs. strain rate trade-off must be interpreted qualitatively at this point.

5.6 Diffuse Deformation Along a Plate Boundary

In the previous section we considered average intraplate deformation rates. Here we consider an example of how these arguments can be used to help interpret the broad zone of

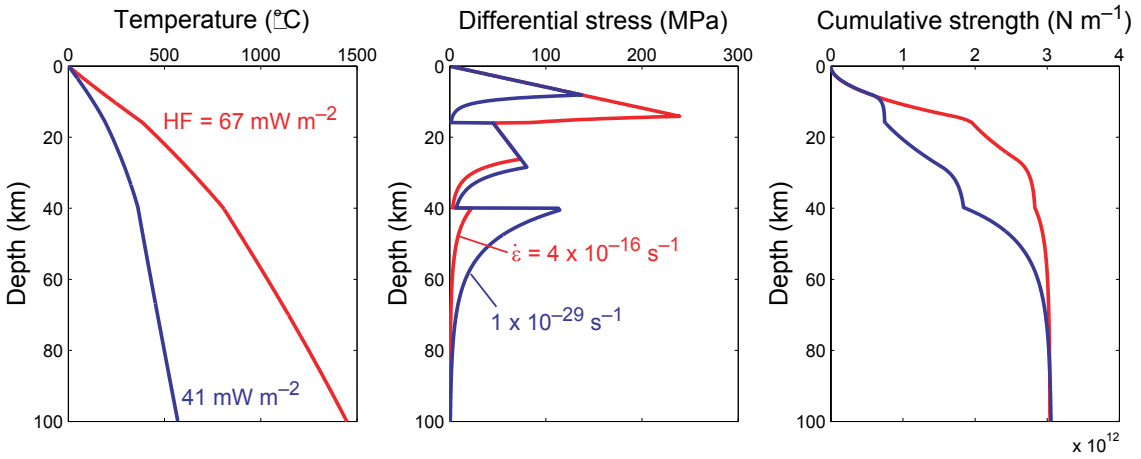

Figure 5.5: A comparison of theoretical temperature, differential stress and cumulative strength profiles for two representative intraplate regions, an area of moderate heat flow (67 mW m^{-2}, red curves) and a shield area with very low heat flow (41 mW m^{-2}, blue curves). See text for details.

distributed deformation along the Pacific/North America plate boundary in western California.

As pointed out by Page et al. (1998), deformation along the San Andreas system is transpressional; in addition to the right-lateral shear accommodating relative motion between the Pacific and North American plates, appreciable convergence has been occurring since 3.5 Ma. This convergence has resulted in uplift, folding and reverse faulting in the Coast Ranges, as illustrated by both the topographic relief (Figure 5.3) and the currently active geologic structures, many of which accommodate shortening perpendicular to the San Andreas fault (Figure 5.6, modified from Page et al., 1998). The locations of the two cross-sections in Figure 5.6 are indicated in Figure 5.3. Note that the transpressional deformation is accommodated over a broad region approximately $>$100 km in width.

This type of distributed deformation might be categorized as a diffuse plate boundary (e.g., Gordon, 1998), but it is interesting to consider more specifically why the transpressional deformation is distributed so broadly, and why there is such an abrupt cessation of this deformation at the boundary between the Coast Ranges and the Great Valley (Figure 5.3). The sharpness of this transition is particularly distinctive given that the entire region is subject to a relatively uniform compressive stress field acting at a high angle to the San

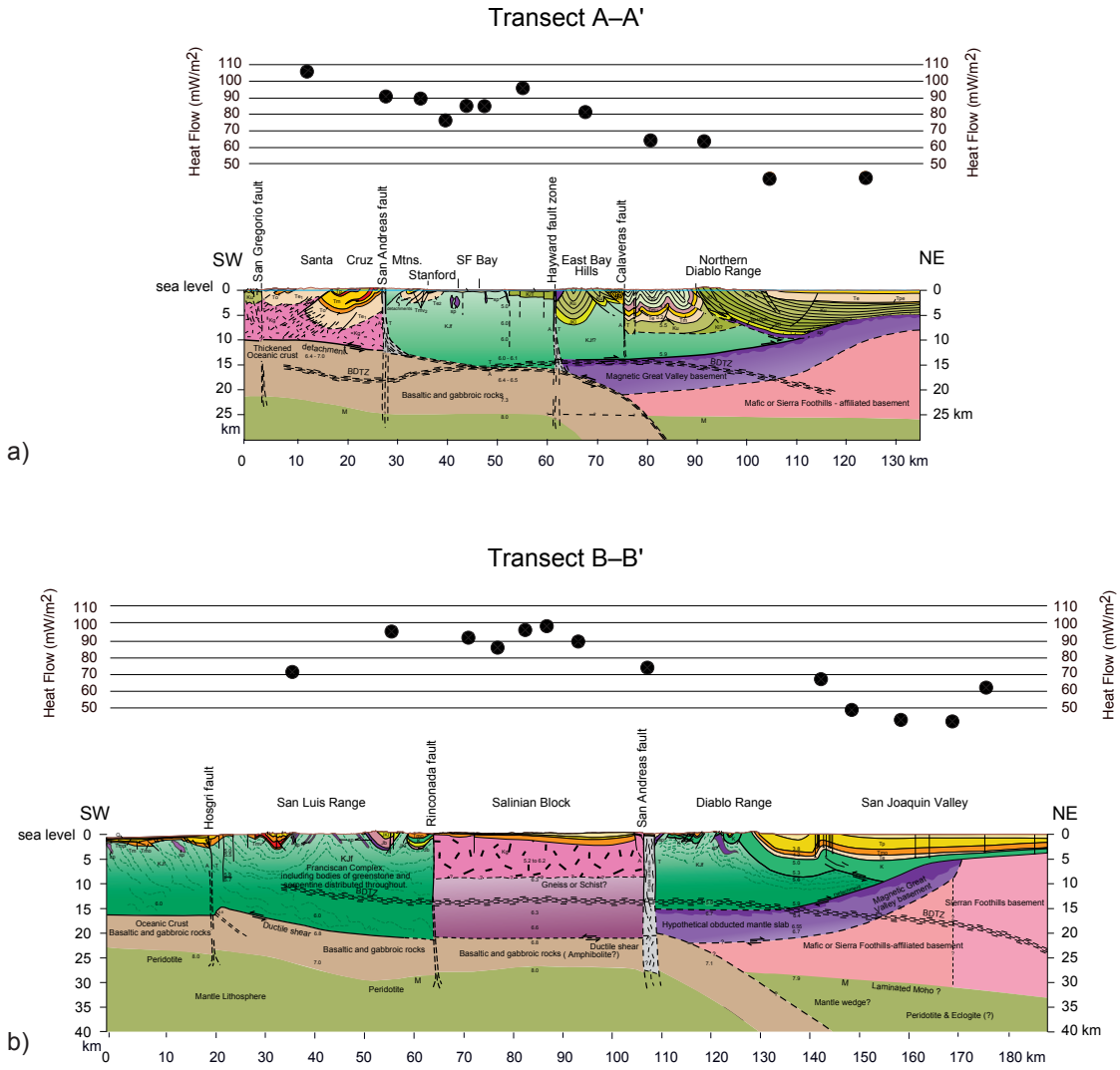

Figure 5.6: Geologic cross-sections and heat flow data across the Coast Ranges and San Andreas fault system in (a) Transect A–A' (shown in Figure 5.3) through the Santa Cruz Mountains and the San Francisco Bay area and (b) Transect B–B' through central California near San Luis Obispo and Kettleman Hills (simplified from Page et al., 1998).

Andreas fault and sub-parallel strike-slip faults (Townend and Zoback, 2001, Figure 5.3). This high angle implies that the San Andreas fault (and perhaps other plate boundaries) have low frictional strength, in marked contrast to the high frictional strength exhibited by intraplate faults and in fact the adjacent crust (briefly summarized by Zoback, 2000).

Moreover, compressive deformation in the Coast Ranges ends abruptly at the Coast Range/Great Valley boundary, even though highly compressive stresses associated with reverse faulting are pervasive along the eastern edge of the Coast Ranges (Wentworth and Zoback, 1989).

To explain this abrupt change in the rate of deformation at the boundary between the Coast Ranges and Great Valley in terms of the principles discussed above, it is important to note that the edge of the transpressive deformation coincides with a marked decrease in heat flow (Figure 5.6), and therefore with lower-crustal and upper-mantle temperatures. In other words, the rate of deformation is high throughout the Coast Ranges because temperatures in the lower crust and upper mantle are high. In contrast, heat flow in the Great Valley is extremely low (comparable to that of shield areas), hence the available force is insufficient to cause deformation at appreciable rates. In fact, as revealed by undeformed seismic reflectors corresponding to formations as old as Cretaceous in age, it is remarkable how little deformation has occurred in the Great Valley during the Cenozoic (e.g., Wentworth and Zoback, 1989).

More generally, we can investigate the regional correspondence of the SAF with areas of high heat flow; a map of heat flow data overlain on topography is shown in Figure 5.7. In central California, the coincidence of the SAF with a zone of high heat flow appears to be a result of crustal heating in the wake of the northward-migrating Mendocino Triple Junction. In this sense, the plate boundary system's evolution creates the necessary thermal conditions for strain localization in a self-organizing manner (N. Sleep, pers. comm. to J. Townend, 2002). The high heat flow Salton Sea region of southern California likewise surrounds the SAF, suggesting that here too the fault's position may be thermally controlled. Recent modeling results (Chéry et al., 2001) suggest that localization of plate boundary slip on the SAF may be related to lateral heat flow gradients, rather than simply the absolute heat flow. Interestingly, in both southern and central California, the SAF tends to be located on the periphery of high heat flow zones, rather than in the middle of these zones. One interesting implication of the model described here is that the "Big Bend" of the SAF might be acting as a large step-over linking weaker lithosphere to the northwest and southeast.

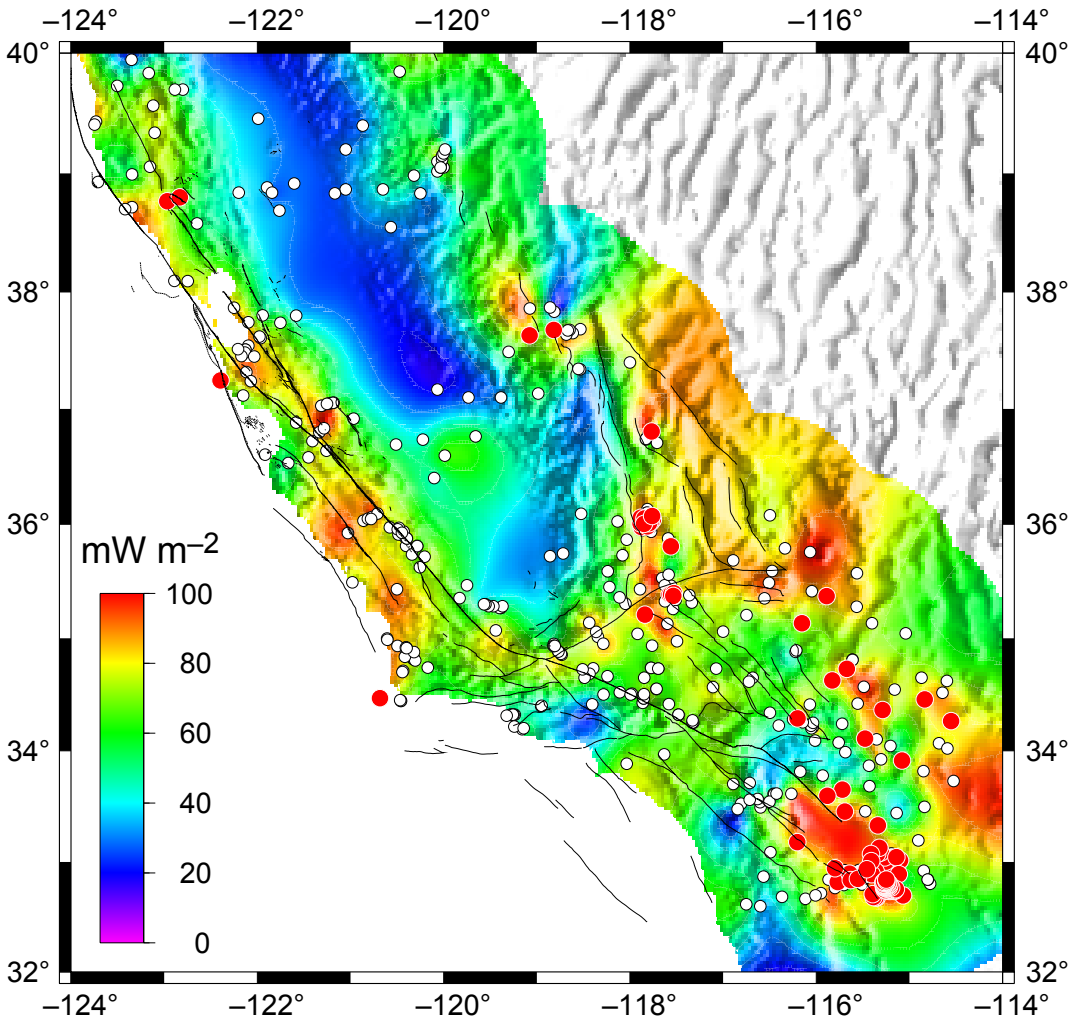

Figure 5.7: A map of crustal heat flow in California. The circles indicate locations at which heat flow measurements have been made: white dots — $\leq$100 mW m^{-2}; red dots — $>$100 mW m^{-2}. Only those data with values of $\leq$100 mW m^{-2} have been interpolated. Data obtained from the USGS Heat Flow Database for California, compiled from numerous published sources (C. Williams, pers. comm. to J. Townend, 2002).

5.7 Conclusions

Overall, it is striking that the observed regional state of stress in southern and central California is so consistent over such a large area, although both the borehole stress measurements and inversions of independent sets of earthquake focal mechanisms reveal relatively

gradual stress variations throughout the region. In general, the observed stress field is very similar to calculations of buoyancy-derived stresses associated with the thermally uplifted Basin and Range province and far-field shear related to Pacific/North America relative plate motion. Thus, while the GPS data show that motions of the crustal blocks adjacent to the plate boundary are consistent with plate kinematics, the forces acting within the crust seem to be controlled by relatively far-field processes. The consistently high angle between S_{Hmax} and the SAF observed along a 400 km-long section of the fault in southern California and the even higher angles seen further north demonstrate that the SAF's frictional resistance to slip — though low in both absolute and relative senses — affects the tectonic stress orientations in the crust immediately adjacent to the fault.

Although the SAF is observed to be weak, it nevertheless appears to interact with the tectonic stress field to the extent that the relative angle between the fault and S_{Hmax} is independent of the fault's strike. A first-order attempt at estimating the effect of the fault's presence suggests that S_{Hmax} rotates anticlockwise by no more than $\sim 7^{\circ}$ within 10 km of the SAF in response to the traction boundary condition it imposes.

We have also demonstrated how the force-limited plate tectonic model can be used to interpret the localization of relative plate motion within a relatively uniform tectonic stress field. As illustrated for the Coast Ranges and Central Valley of western California, in the area of presumed high temperatures in the lower crust and upper mantle (the Coast Ranges), the strong temperature-dependence of the effective viscosity of the lower crust and upper mantle results in high deformation rates. In the adjacent Central Valley, where we expect low temperatures in the lower crust and upper mantle, it is observed, as anticipated, to deform at an extremely slow rate. These results suggest that in the context of the steady-state failure equilibrium model, the debate over whether intraplate deformation is best-viewed in terms of a deforming continuum or rigid crustal blocks separated by relatively weak fault zones may be a false dichotomy because both types of behavior are to be expected.

Acknowledgments

We are very grateful to Lucy Flesch and Bill Holt (State University of New York at Stony Brook) for their model results and enthusiastic encouragement, and to Greg Beroza, Björn

Lund, Norm Sleep and George Thompson for thought-provoking suggestions. Some sections of this chapter were presented at a symposium honoring the career and contributions of George A. Thompson held at Stanford University on the 8th and 9th of December 2001. This work was supported by a Lieberman Fellowship from Stanford University.

Chapter 6

The Contemporary Tectonic Stress Field in Japan

6.1 Abstract

Japan's complex tectonic setting provides a challenging study area for investigating the relationship of the tectonic stress field to large-scale processes of subduction and crustal collision. By amalgamating travel time and first motion data recorded throughout Japan by the Japan Meteorological Agency (JMA) and the Japanese University Network (JUNEC) consortium, and in central Japan by the National Research Institute for Earth Science and Disaster Prevention (NIED), we have obtained a consolidated focal mechanism catalog with which to investigate tectonic stress directions.

The benefits of merging independent seismicity catalogs are most clearly demonstrated in central Japan, where ∼25,000 unique focal mechanisms have been calculated for the period 1985–1996: approximately 25% of these solutions could not be determined using any one of the three original catalogs alone. The improved station geometry achieved with the merged data also results in smaller hypocentral errors and strike, dip, and rake confidence intervals.

Using the consolidated catalog, we have estimated crustal stress directions throughout most of Japan, as well as along vertical cross-sections through the shallow parts of the subduction zones. Our results reveal approximately trench-parallel and trench-perpendicular

orientations of the axis of maximum horizontal compressive stress, S_{Hmax}, in southwestern Japan and northeastern Honshu, respectively, and a radial pattern of S_{Hmax} directions in central Japan. We compare these crustal stress results with independent estimates of horizontal strain in central and southwestern Japan. The orientation of S_{Hmax} is found to agree well with the axis of greatest contractional strain once the effects of interseismic strain accumulation have been removed from the observed deformation field according to an elastic model of subduction thrust locking. This residual deformation, or apparent inelastic strain field, is inferred to reflect collision of the Amurian plate with northern Japan, and is presumed to be independent of the deformation associated with strain accumulation and release in the subduction zone earthquake cycle. We conclude that the state of crustal stress in central Japan is related more to collision within the upper plate of the Nankai Trough and Japan Trench subduction zones than to locking of the subjacent subduction thrusts.

6.2 Japan's Tectonic and Kinematic Framework

6.2.1 Tectonic Configuration

Convergence of the Philippine Sea and Pacific plates with Japan occurs along two principal subduction zones, the Nankai Trough and the Japan Trench (Figure 6.1). The four main islands of Japan, which together form the upper plate of the two subduction zones, are composed of the Amurian plate, the North American or Okhotsk plate, and several microplates that behave as coherent tectonic units but whose boundaries and velocities with respect to one another remain equivocal (e.g., Heki et al., 1999; Sagiya et al., 2000; Mazzotti et al., 2001; Miyazaki and Heki, 2001). Internal deformation of the Japanese arc itself is well resolved by a nationwide global positioning satellite (GPS) array, which comprises approximately 1000 receivers spaced an average of 35 km apart (Sagiya et al., 2000).

In southwestern Japan, the Philippine Sea plate (PHS) is being subducted beneath the Amurian plate (AMU) along the Nankai Trough at a rate of 63–68 mm a^{-1} towards 305° (Miyazaki and Heki, 2001). In central Japan, the Zenisu and Izu–Bonin ridges collide with the Kanto region; microseismicity (Ishida, 1992) and geodetic data (Mazzotti et al., 1999)

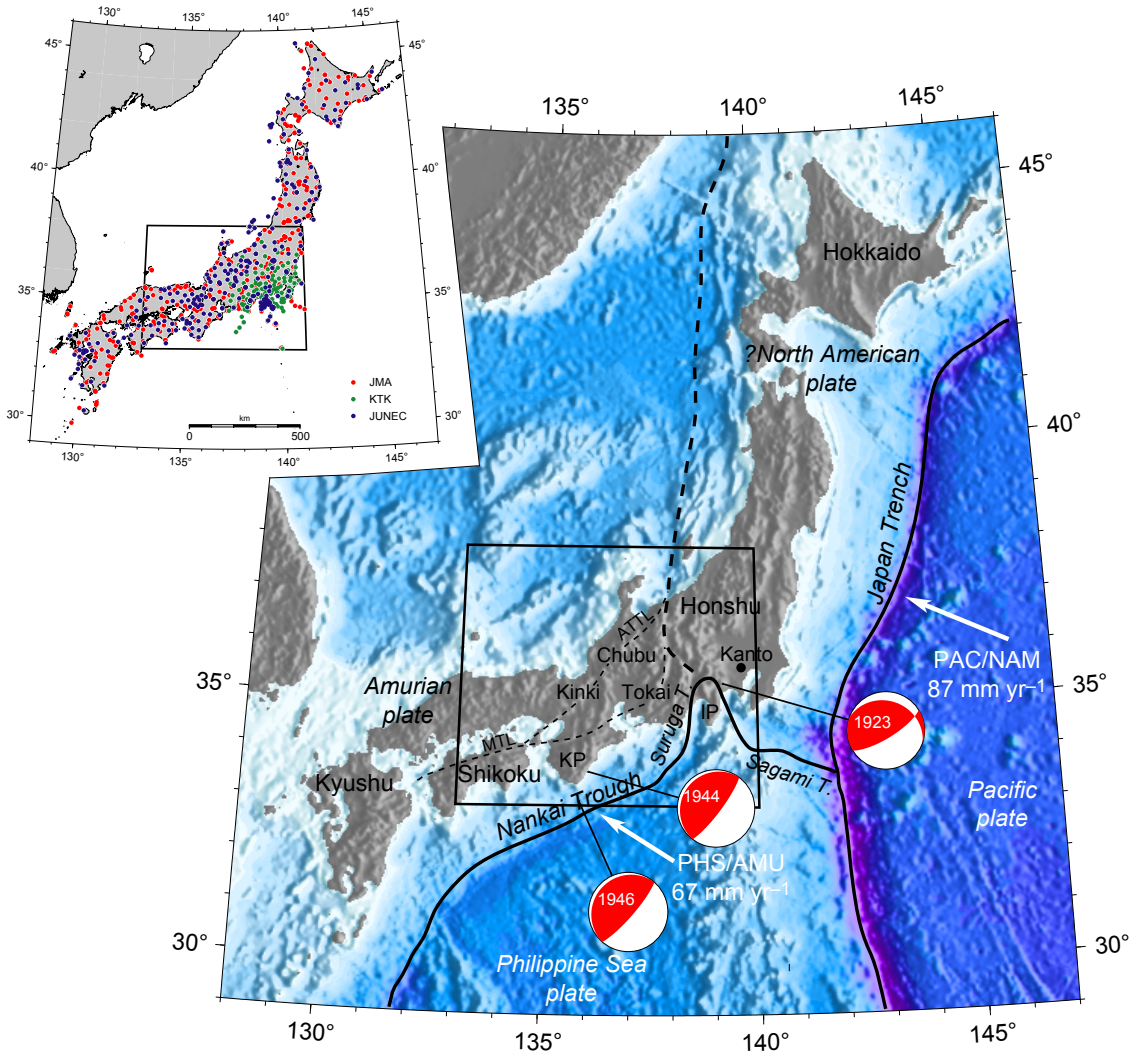

Figure 6.1: Maps of Japan showing the main tectonic elements, their relative motions, and three significant twentieth century earthquakes (main map) and the locations of the seismometers constituting the three networks referred to in this chapter (inset). The box in each map indicates the area shown in Figure 6.9. ATTL — Arima–Takatsuki Tectonic Line; IP — Izu Peninsula; KP — Kii Peninsula; MTL — Median Tectonic Line. Faults and plate boundaries after Heki et al. (1999) and Miyazaki and Heki (2001).

suggest that the subducting Philippine Sea Plate is torn or at least strongly bent beneath Kanto, due to the complexity of subduction along the Sagami and Suruga Troughs. Both the Tokai and Kanto forearc regions exhibit significant motion with respect to the Amurian

plate (Mazzotti et al., 2001).

The subduction geometry along the northeastern coast of Honshu is somewhat simpler than that in central and southwestern Japan, although the relationship of the upper plate to either the Amurian plate or the North American/Okhotsk plate is unclear (Mazzotti et al., 2001). The Pacific plate (PAC) is subducting beneath the northeastern Honshu arc at a velocity similar to the NUVEL-1A Pacific–North America (NAM) prediction of 91 mm a^{-1} towards 290° (Mazzotti et al., 2000; DeMets et al., 1994).

6.2.2 Seismicity and Interseismic Strain

Japan experiences major earthquakes regularly, many of the most devastating of which have occurred in the central and eastern Nankai Trough. Ando (1975) used deformation data and historical accounts to construct a paleoseismic record of large earthquakes along the Nankai Trough since the year 684. During this 1,300 year period, 13 major earthquakes have occurred, exhibiting a systematic pattern of cyclicity along the margin. In particular, Ando identified four distinct fault segments along the trough and demonstrated that individual earthquakes tended to rupture pairs of these fault segments. Only one earthquake, in 887 A.D., ruptured all four segments at once. Four instances in which the two easternmost segments ruptured a few years prior to the two westernmost have also been recognized. These patterns imply not only persistent segmentation of the plate margin, but also a characteristic seismic behavior. Ando (1975) noted the absence of expected slip during the 1944 Tonankai earthquake on the westernmost fault segment beneath the Tokai region — the "Tokai gap" — and estimated that moment equivalent to a **M** 8 earthquake had accumulated since 1854, when the segment last ruptured. This observation, although later revised by other authors (e.g., Ishibashi, 1981), led to Japan's concerted earthquake prediction efforts because of the huge societal implications of a large earthquake beneath the Tokai region (reviewed recently by Ishibashi and Satake, 1998).

The last two major earthquakes to occur in the Nankai Trough were the 1944 **M** 8.1 Tonankai and 1946 **M** 8.3 Nankaido events, which geodetic and tsunami data suggest ruptured distinct patches on either side of a $\sim$50 km-wide slip gap southwest of the Kii Peninsula

(Sagiya and Thatcher, 1999; Cummins and Kaneda, 2000). This gap has been noted by several other authors (e.g., Ando, 1975; Satake, 1993; Yoshioka et al., 1993) and postulated to correspond to a break or tear in the Philippine Sea plate; it appears to also coincide with a seamount being subducted beneath the arc (Park et al., 1999).

Long-term interseismic deformation following the 1944 Tonankai and 1946 Nankaido earthquakes has also been thoroughly investigated. Savage (1983, 1995) and Savage and Thatcher (1992) used a variety of strain data to analyze locking of the Tonankai/Nankaido subduction interface. The models satisfactorily reflected the gross interseismic behavior of the margin, but did not completely quantitatively explain local uplift behavior. Mazzotti et al. (2000) used horizontal displacement GPS data to calculate the interplate coupling ratio — the ratio of interseismic relative normal slip ("back slip") on the locked patch to the overall subduction velocity — in the central Nankai Trough and northeastern Japan Trench. The inversion results showed almost complete locking between 8 km and 25 km depth throughout the central Nankai Trough, and along the Japan Trench as well; in this and several other studies, the up- and down-dip limits of the locked section are generally presumed to be, or found to coincide with, those estimated using a thermo-rheological model with limits controlled by the smectite–illite transition and the onset of ductile deformation (Hyndman et al., 1995, 1997).

The Mazzotti et al. (2000) results are intriguing because the homogeneous interseismic locking implied by the geodetic data does not reflect the known along-strike variation in subduction geometry or the region's characteristic seismogenic behavior. In particular, no discontinuity or variation is noticed in the vicinity of the Kii Peninsula, and nor can any correspondence to the seismic segmentation implied by Ando's (1975) paleoseismic results be straightforwardly recognized. Hence, a picture of uniform interseismic locking has emerged that is at odds with the localized and heterogeneous coseismic slip distributions.

6.2.3 Relative Crustal Motions and Apparent Inelastic Strain

The task of first delineating the plates, microplates, or crustal blocks interacting in Japan, and then determining their relative velocities, is complicated by the much larger strain rates associated with interseismic loading than with secular plate motions (e.g., Wang, 2000;

Mazzotti et al., 2001; Miyazaki and Heki, 2001). Since the interseismic strain rates are associated with stresses that are smaller than the intraplate tectonic stresses on which they are superimposed, it is important to distinguish deformation associated with interseismic strain accumulation and the earthquake cycle from any irrecoverable deformation associated with relative plate motions in order to compare tectonic stress and strain patterns.

Mazzotti et al. (2001) and Miyazaki and Heki (2001) recently estimated the effects of contemporary subduction interface locking and subtracted these from the total (observed) deformation field in central and southwestern Japan, respectively, to obtain a residual ("corrected"; Mazzotti et al., 2001) deformation field, interpreted in both cases to correspond to long-term inelastic deformation.

In the first of these studies, Mazzotti et al. (2001) made use of estimates of interseismic strain accumulation on the eastern Nankai, Suruga, and Sagami subduction zones calculated with an inverse modeling technique by Henry et al. (2001). Those results were obtained using a back-slip dislocation model (Savage, 1983), in which localized interseismic locking is represented by the superposition of a normal-faulting slip vector on the otherwise uniform reverse-faulting slip vector corresponding to the long-term subduction velocity (Figure 6.2). The geometry of each subduction thrust was determined from seismicity profiles, and each thrust was assumed to be uniformly locked between up-dip and down-dip transition zones (Hyndman et al., 1995) in which coupling was linearly tapered (Mazzotti et al., 2000). The residual deformation field obtained after subtracting the crustal velocities associated with Henry et al.'s (2001) best-fitting interseismic locking model from the original measured velocities was demonstrated to correspond well with that expected on geological grounds for the collision in central Japan of the Amurian plate with northeastern Japan. In particular, the localization of high strain rates (100–200$\times 10^{-9}$ yr^{-1}) within a 100 km-wide zone extending across the Kinki region from the Median Tectonic Line along the Arima–Takatsuki Tectonic Line (Figure 6.1) to the northern Japanese Alps is consistent with the geographic distribution of faults thought to have been active during the Quaternary, paleoseismic estimates of Quaternary strain rates, and independent triangulation estimates (Mazzotti et al., 2001). Moreover, the residual strain rate data exhibit a distinct region of low strain rates in southwesternmost Honshu, which is thought to deform little internally (Heki et al., 1999).

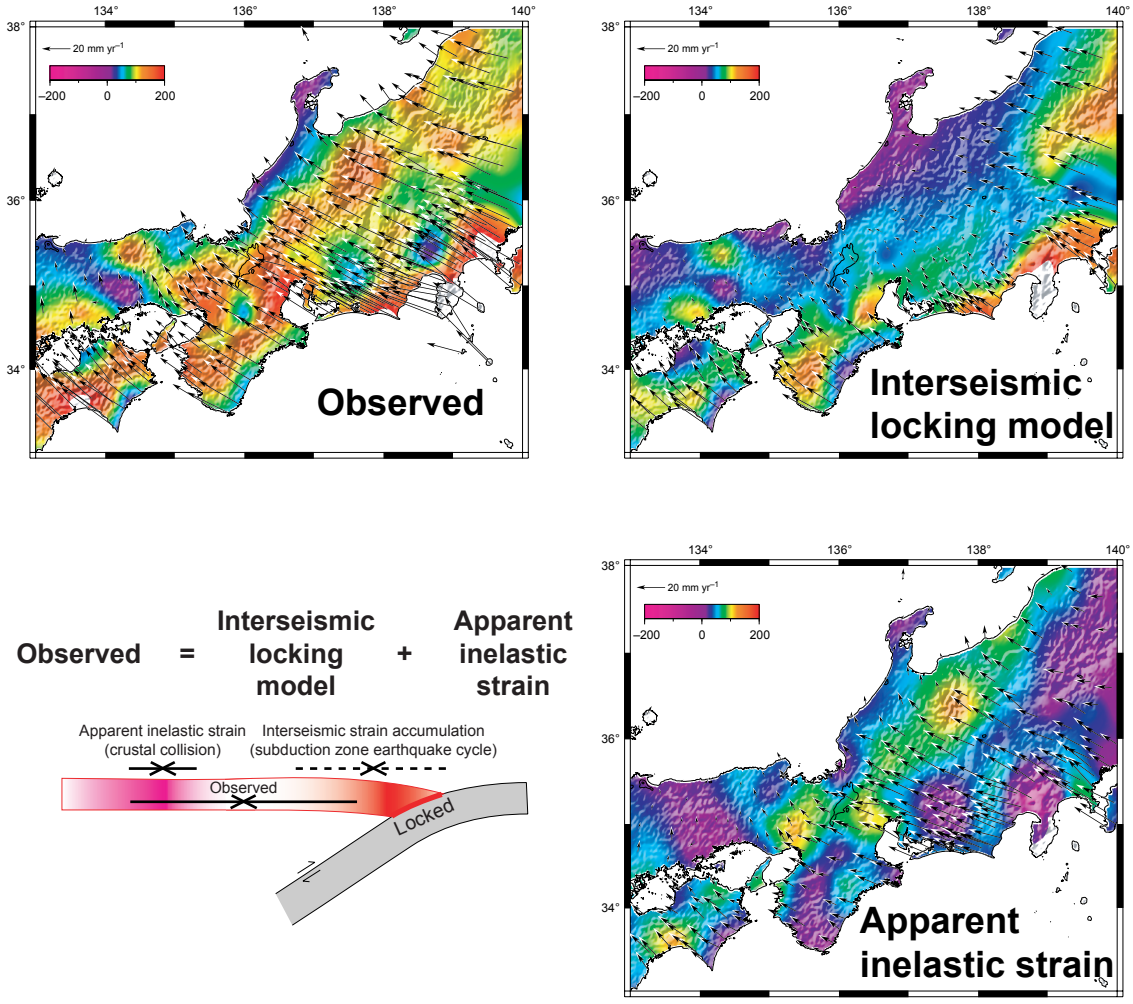

Figure 6.2: Schematic illustration (lower left) and results of decomposing the observed horizontal deformation field in central Japan (upper left) into a component related to interseismic locking of the Nankai Trough and Japan Trench subduction interfaces ("interseismic locking model", upper right) and a residual field presumed to represent inelastic strain ("apparent inelastic strain", lower right; S. Mazzotti, pers. comm. to J. Townend, 2002, after Mazzotti et al., 2001). The vectors and shading indicate horizontal velocities with respect to the Amurian plate, and dilatational strain rates (10^{-9} s^{-1}) respectively.

In contrast to the inverse modeling approach adopted by Henry et al. (2001), Miyazaki and Heki (2001) used a forward model of interseismic locking to calculate the associated horizontal deformation field, on the grounds that this technique avoids contamination of

the locking estimate by any observations affected by processes other than locking alone. Notwithstanding this important difference, Miyazaki and Heki's (2001) results are consistent with those of Mazzotti et al. (2001) in revealing abrupt residual velocity gradients (equivalent to high rates of inelastic E–W contraction accommodated on conjugate strike-slip faults) in the Kinki and Chubu regions (cf. Thatcher and Matsuda, 1981) and very low residual velocities relative to the Amurian plate throughout southwestern Honshu. Miyazaki and Heki (2001) interpreted these results to indicate that inelastic deformation in central Japan is predominantly due to the collision of the Amurian plate with northeast Honshu, and accommodated by the lateral extrusion of microplates in a manner similar to that associated with the collision of India and Eurasia.

It is important to reiterate that in both the Mazzotti et al. (2001) and Miyazaki and Heki (2001) studies, the residual deformation field depends directly on the particular elastic model of interseismic locking being employed (cf. Lewis et al., 2003). Consequently, some discretion must be used in interpreting the residual component of deformation as anything other than mis-modeling. However, while any residual strain could be ascribed solely to an inappropriate locking model, the similarities between the two studies' results in spite of the different methodologies employed, and their mutual concordance with (1) the observed distribution of Quaternary faulting in central Japan, (2) independent estimates of Quaternary strain rates, and (3) the predicted motion of the Amurian plate with respect to northeastern Japan, suggest that the residual strain is not a straightforward artifact of unrealistic locking estimates.

Moreover, as it will be seen below, the principal axes of Mazzotti et al.'s (2001) residual strain rate field exhibit striking similarities with the principal stress axes determined from earthquake focal mechanism inversions. For the purposes of this work, therefore, we treat the deformation field obtained by subtracting a model of interseismic locking from the observed deformation measurements as representative of inelastic strain related to secular crustal motions in central and southwestern Japan and refer to it as the "apparent inelastic strain".

6.2.4 Previous Stress Orientation Studies

In studies by Shiono et al. (1980), Tsukahara and Kobayashi (1991), and Tsukahara and Ikeda (1991), the orientation of the axis of greatest horizontal compression, S_{Hmax}, was estimated using average focal mechanism P axes throughout central and western Honshu. Unfortunately, the data on which these estimates are based have never been systematically compiled (H. Tsukahara, pers. comm. to M. D. Zoback). Moreover, the procedure used to estimate S_{Hmax} in these studies is an ad hoc method based on a frictional failure criterion applied to individual earthquakes: the errors in stress orientation ($\pm 30^\circ$) are not appreciably less than those that would arise from simply treating the P axis as S_1 ($\pm 45^\circ$). Nevertheless, these and other authors (e.g., Kurogi, 1999) have commented on a general pattern of SW–NE-trending S_{Hmax} in southern Honshu and Kyushu, and an approximately NW–SE orientation in northern Honshu.

The average P axis orientation of horizontal earthquakes in southwestern Japan has proven difficult to reconcile with the SE–NW direction of convergence between the Philippine Sea plate and the overlying arc. Several researchers have investigated stress states within the upper plate using numerical models (e.g., Hassani et al., 1997; Wang and He, 1999; Zhao and Takemoto, 2000; Baba et al., 2001). In each of these models, the effective coefficient of friction on the main subduction thrust plays an important role in controlling stresses in the forearc. However, these models have hitherto not been constrained by direct measurements of in situ subduction zone stresses, and have generally (cf. Wang and He, 1999) used quasi-kinematic (slip rate) boundary conditions.

Nakamura and Uyeda (1980) summarized stress fields within the Japanese arc and elsewhere in terms of a model in which the vertical stress changes from being S_3 in the forearc (corresponding to reverse faulting), S_2 in the volcanic arc (strike-slip faulting), and S_1 in the backarc (normal faulting). The model has implications for the mechanisms by which stress is transmitted across the arc but has not been subsequently addressed in detail using stress orientation data obtained from earthquake focal mechanisms. Seno (1999) nevertheless undertook to account for the presumed stress orientations (P and T axes) throughout Japan using a highly simplified model of the regional plate configuration and driving forces. With

	Region	Results
Magee & Zoback (1993)	NE Honshu	S_1 along strike, S_2 down dip, fault-normal S_3
Delouis et al. (1996)	N Chile	fault-normal S_1, S_2 along strike, S_3 down dip
Lu et al. (1997)	Alaska	S_1 along strike, fault-normal S_2, S_3 down dip
McGinty et al. (2000)	Hikurangi	fault-normal S_1, S_2 along strike, S_3 down dip

Table 6.1: Recent studies of stress orientations in subduction zones.

the exception of Kyushu and Hokkaido, the Japanese stress field was concluded to be adequately explained via long-range ridge push and slab pull forces on which are juxtaposed the effects of variable cross-arc topography and crustal thickness. Seno invoked viscous drag forces to explain the Kyushu stress field, but the paucity and nature of the data used make this interpretation rather speculative.

The state of stress adjacent to either of the two Japanese subduction thrusts has likewise been studied very little. Elsewhere, however, a number of studies, of which the most recent and reliable are summarized in Table 6.1, have used earthquake focal mechanisms to investigate stress orientations within the seismogenic portions of subduction zones. These studies have yielded the consistent result that the main subduction thrust is subject to low ratios of shear to normal traction, and is inherently very weak. Magee and Zoback (1993) investigated whether this weakness stems from very low friction or the existence of suprahydrostatic fluid pressures, and concluded that the latter factor was more straightforwardly justified on the basis of abundant evidence for dehydration and fluid expulsion along the subduction décollement.

6.3 An Integrated Seismicity Catalogue for Central Japan

6.3.1 Merging Procedure

We are fortunate in having been able to acquire three independently recorded earthquake phase data catalogs (arrival times and first motion polarities): the Japan Meteorological Agency (JMA) catalog, the Japan University Network Earthquake Catalog (JUNEC), and the National Research Institute for Earth Science and Disaster Prevention's Kanto–Tokai

Network Catalog (KTK). The first two catalogs include data recorded by a national array of seismometers, whereas the KTK network is concentrated primarily in central Japan between latitudes 33.5°N and 36.5°N and longitudes 135°E and 142°E.

Merging the different data sets is complicated by the fact that they not only contain different numbers of earthquakes, but also contain slightly different hypocentral parameters for those earthquakes that they do in fact share in common. A two-step merging process, listed below, appears to give good results: we first merge the JMA and JUNEC catalogs, and then merge the result with the KTK data to produce the final consolidated catalog. In each of the two steps, an event in one catalog is presumed to be represented in the other if it occurred within a given time (10 s), horizontal distance (0.65°), and vertical distance (60 km) of an event. In practice, the timing constraint alone is sufficient to match most earthquakes, and the average origin time difference is generally $<$1 s.

1. (Hypocenters) Merge the JUNEC and JMA phase data
2. Merge (JUNEC+JMA) and KTK phase data
3. Compute hypocenters from the consolidated (JUNEC+JMA+KTK) P and S phase data using HYPOINVERSE2000 ($\geq$8 arrivals, 0.1 s standard timing error, standard distance and residual weighting parameters; Klein, 2002) and the Ukawa et al. (1984) Kanto–Tokai velocity model
4. (Focal mechanisms) Compute focal mechanisms with FPFIT using tolerant quality parameters ($\geq$8 first motions, 500 km maximum epicentral distance, all magnitudes, default error rates; Reasenberg and Oppenheimer, 1985)
5. Extract single, stable (numerically convergent) focal mechanisms ($\leq$10% solution misfit, $\leq$135° maximum azimuthal gap, $\leq$10° maximum half-width of strike, dip, and rake 90% confidence ranges, $\leq$10 km standard horizontal error, $\leq$20 km standard vertical error)
6. Compute supplementary solutions using JUNEC, JMA, and KTK stations alone
7. Incorporate supplementary solutions into final focal mechanism catalog if the consolidated phase data did not produce a single, convergent solution

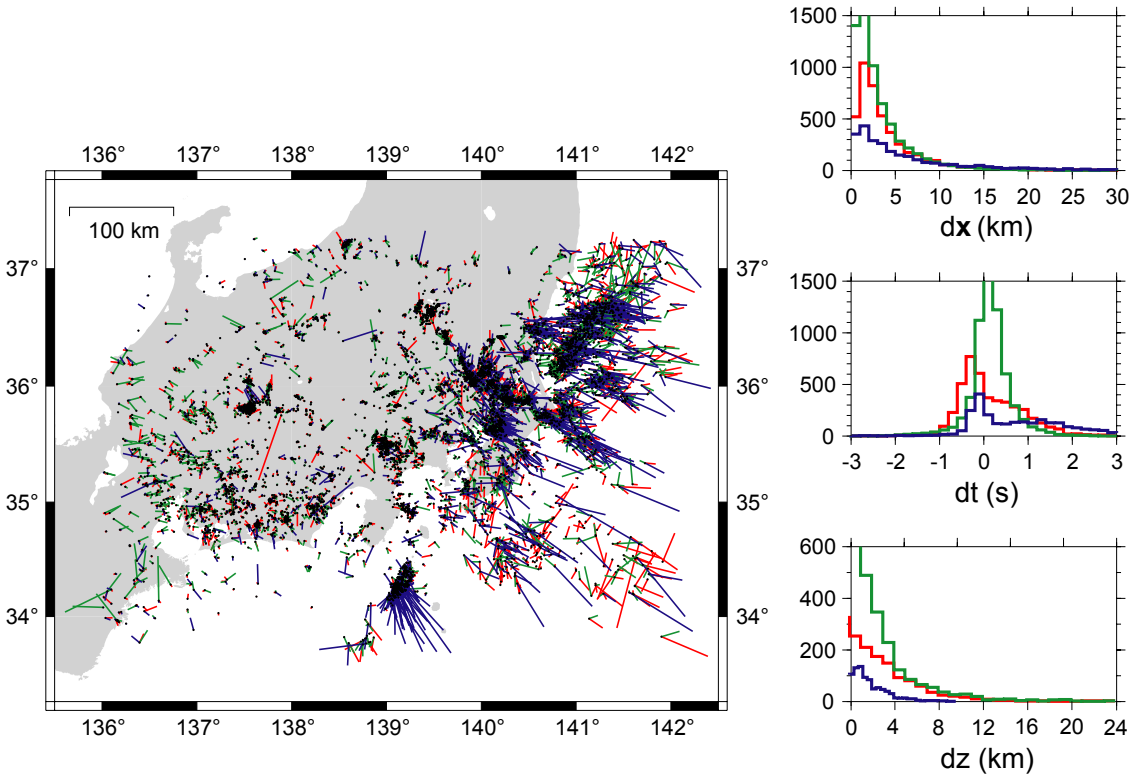

Figure 6.3: Results of merging the 1992 seismicity in central Japan. Map: Colored vectors link the epicenter determined using the amalgamated arrival data with the original JMA (red), KTK (green), and JUNEC (blue) epicenters. Histograms: Differences in horizontal position (d**x**, top), time (dt, middle), and depth (dz, bottom) between the final epicenter and each of the original epicenters. The color scheme is the same as in the main map.

6.3.2 Hypocentral and Focal Mechanism Parameters

In Figures 6.3–6.6 we illustrate the effects of merging separate phase data for the region in central Japan between (135.5°E,33.25°N) and (142.5°E,37.75°N), which is spanned by all three networks. The KTK network does not extend much beyond this area, and so throughout the rest of Japan only the JUNEC and JMA catalogs can be merged.

Figure 6.3 illustrates the results of merging one year's data from central Japan. For each event, the epicenter determined by a relocation of the combined arrival data is shown and linked to the original epicenters by a line whose color denotes the original catalog. Note

	All events				Common events			
	Joint	KTK	JUNEC	JMA	Joint	KTK	JUNEC	JMA
n	**116,027**	102,120	35,372	34,420		(15,559)		
RMS (s)	0.24	**0.23**	0.25	0.37	**0.30**	0.33	0.27	0.42
STH (km)	**0.72**	0.83	1.10	1.35	**0.52**	0.77	1.12	1.31
STV (km)	**1.18**	1.25	1.87	2.29	**0.92**	1.20	1.92	2.34
nPS	**26**	20	20	17	**102**	54	25	21
nvP	**20**	16	16	13	**59**	38	19	17
nvS	**7**	7	3	5	**21**	16	3	6
nfm	3	3	**6**	1	**18**	8	8	1
azm (°)	**136**	160	142	145	**73**	122	135	125

Table 6.2: Median hypocentral quality parameters for each complete catalog (left-hand columns) and the 15,559 events common to all three original data sets (right-hand columns). n — number of events; RMS — root mean square time residual; STH, STV — standard horizontal and vertical errors; nPS — total number of P and S arrivals; nvP, nvS — number of P and S arrivals with nonzero weights; nfm — number of first motions; azm — maximum azimuthal gap. The bold entry in each row indicates the catalog with the optimum median value.

that because many earthquakes were not recorded by all three networks, the number of line segments radiating from each joint epicenter is commonly less than three. The Ukawa et al. (1984) velocity model used here is the same as that used by NIED for routine earthquake locations in central Japan, but differs from the models employed in either the JUNEC or JMA locations.

Figure 6.4 shows cumulative histograms of eight location quality parameters (see caption) for each of the three original catalogs and the final consolidated catalog; the corresponding data are summarized in Table 6.2 (“All events”). Merging the catalogs produces a larger and generally better-constrained data set than any of the three contributing catalogs, but the KTK network’s contribution clearly overwhelms those of the JUNEC and JMA networks. This is because the KTK network sits directly above central Japan and records many more low-magnitude (**M**<2) events than either of the other two networks.

The benefits of merging are more apparent when only those events common to all three original catalogs are compared (Figure 6.5 and Table 6.2, “Common events”). Specifically, the greater number of P and S arrival data and improved station geometry (in terms of maximum azimuthal gap) in the merged seismicity catalog reduce travel time residuals and

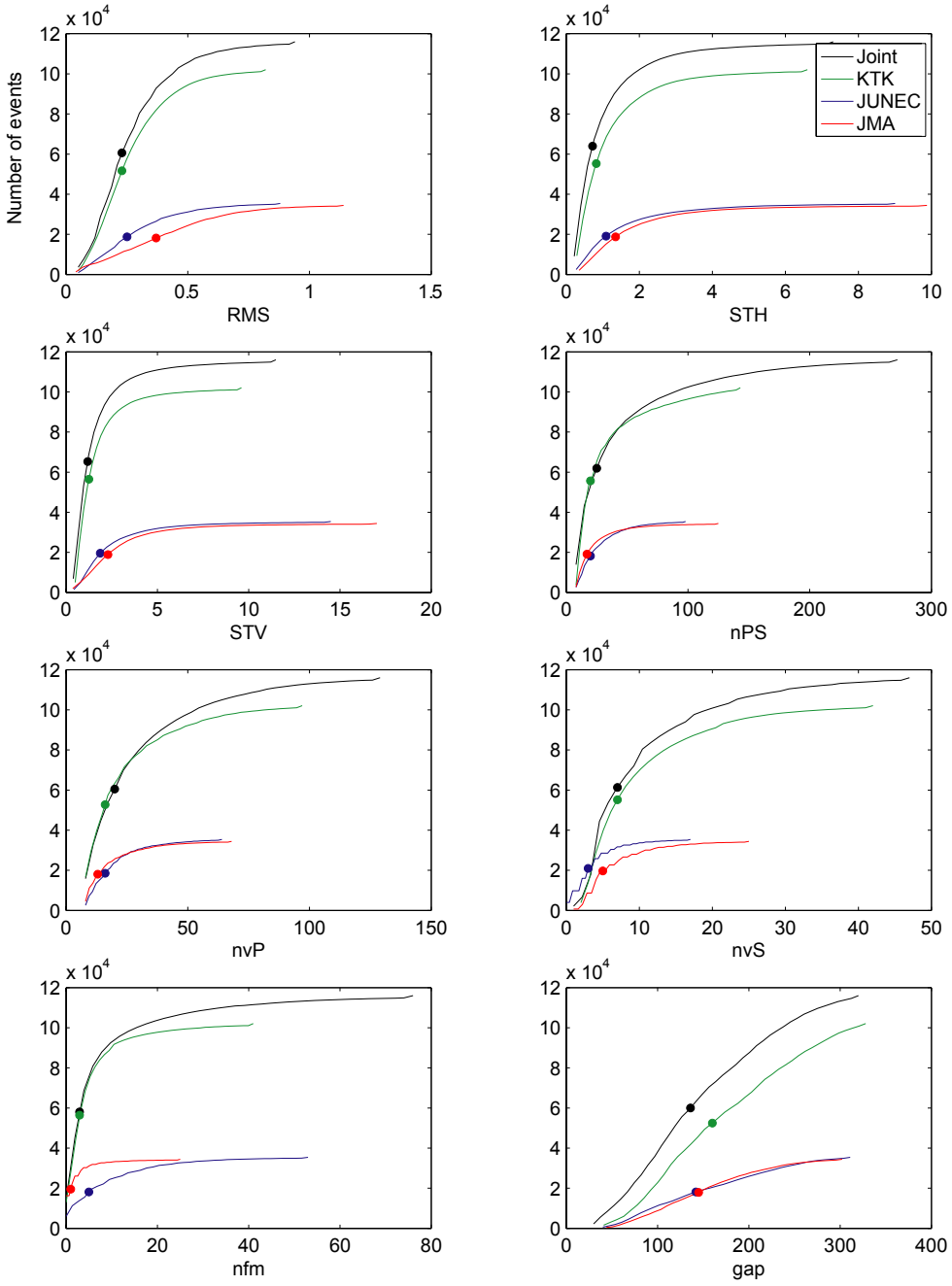

Figure 6.4: Cumulative histograms (lines) and median values (dots) of the hypocentral quality parameters for each complete catalog. RMS — root mean square time residual; STH, STV — standard horizontal and vertical errors; nPS — total number of P and S arrivals; nvP, nvS — number of P and S arrivals with nonzero weights; nfm — number of first motions; azm — maximum azimuthal gap.

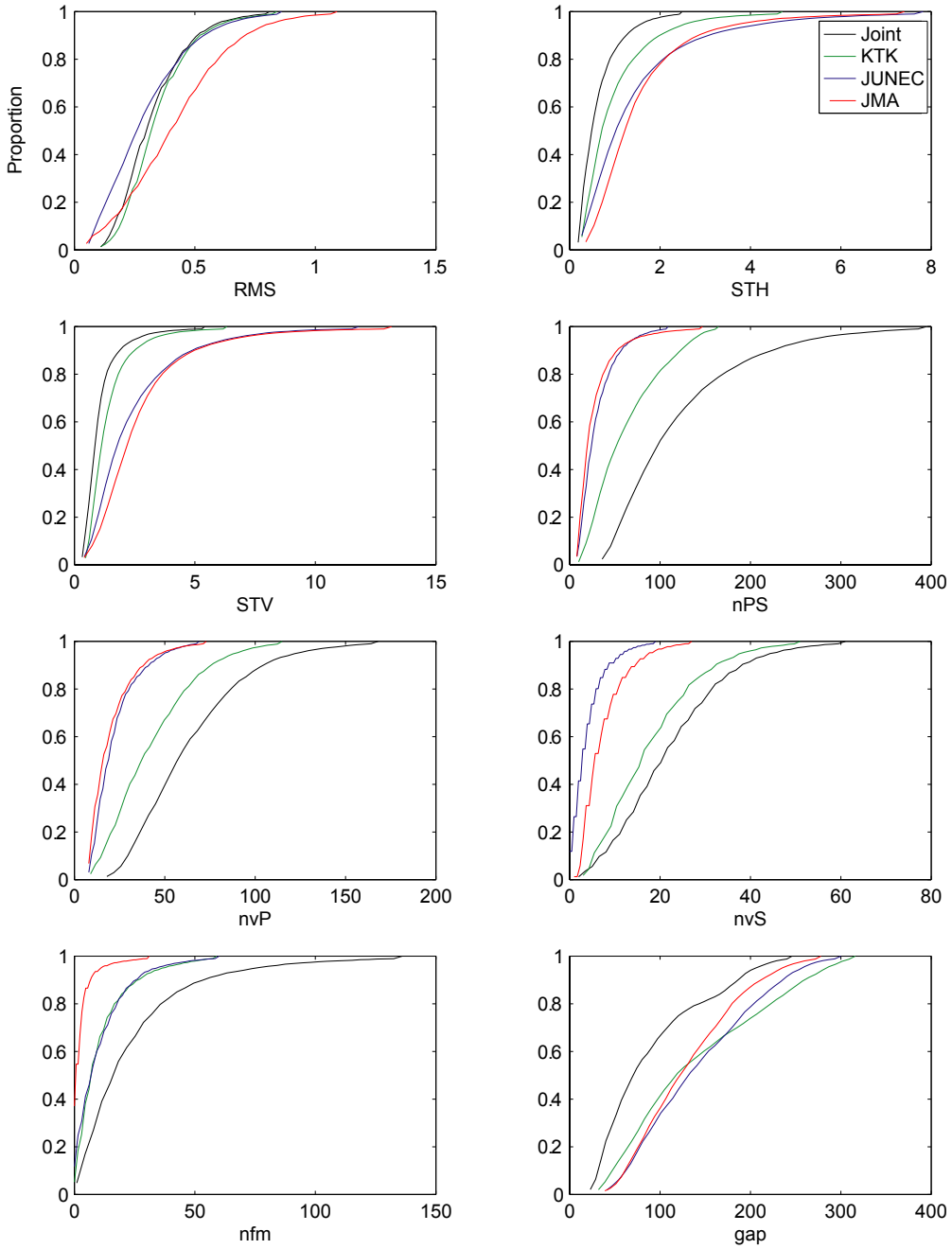

Figure 6.5: Normalized cumulative histograms of the hypocentral quality parameters for the 15,559 events common to all three original data sets. RMS — root mean square time residual; STH, STV — standard horizontal and vertical errors; nPS — total number of P and S arrivals; nvP, nvS — number of P and S arrivals with nonzero weights; nfm — number of first motions; azm — maximum azimuthal gap.

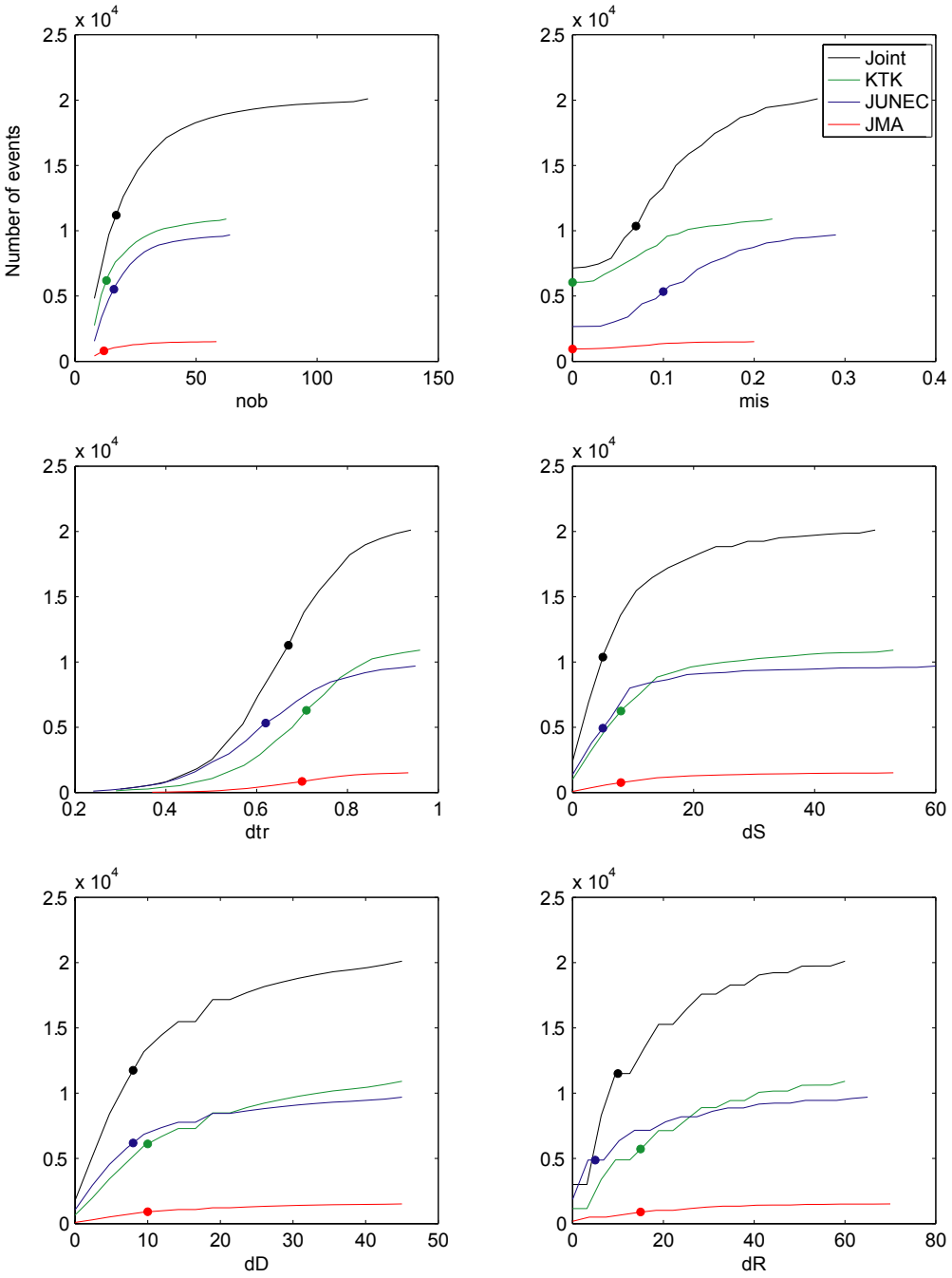

Figure 6.6: Cumulative histograms (lines) and median values (dots) of the focal mechanism quality parameters for the events that gave single, convergent focal mechanism solutions. nob — number of first motion observations; mis — misfit; dtr — station distribution ratio; dS, dD, dR — estimated uncertainty in strike, dip, and rake, respectively.

	All events				Amalgamated catalog	
	Joint	KTK	JUNEC	JMA	Extra	Joint + Extra
n	20,103 (6,809)	10,903	9,687	1,508	5,215	25,318
nob	17 (12)	13	16	12	15	16
mis	0.07 (0.06)	0.00	0.10	0.00	0.06	0.07
dtr	0.67 (0.67)	0.71	0.62	0.70	0.67	0.67
dS	5 (8)	8	5	8	5	5
dD	8 (10)	10	8	10	8	8
dR	10 (10)	15	5	15	10	10

Table 6.3: Median focal mechanism quality parameters for each catalog. The numbers in parentheses give the values for focal mechanisms that could only be computed by merging the data sets (Joint) or by *not* merging the data sets (KTK, JUNEC, JMA). In the latter cases, merging the data sets resulted in multiple or poorly convergent solutions. n — number of events; nob — number of first motion observations; mis — misfit; dtr — station distribution ratio; dS, dD, dR — estimated uncertainty in strike, dip, and rake, respectively.

standard errors with respect to the hypocenters computed using phase information from a single data set alone. As noted above, the velocity model used here is the same as that used for routine KTK locations. Consequently, the improvement in the root mean square time residual and standard horizontal and vertical errors obtained for the KTK events by incorporating JUNEC and JMA data is due to the increased number of data and not simply the result of using a different velocity model.

Computing focal mechanisms with the consolidated catalog results in a substantial increase in the number of convergent solutions and a corresponding decrease in strike, dip and rake uncertainties (Table 6.3 and Figure 6.6). We construct the final focal mechanism catalog (Figure 6.7) hierarchically from (a) all well-behaved (single-solution, numerically convergent) mechanisms using all stations, (b) any other mechanisms calculated using only KTK stations, (c) any other mechanisms calculated using only JUNEC stations, and (d) any other mechanisms calculated using only JMA mechanisms.

6.4 Horizontal Crustal Stresses

Figures 6.8 is a map of Japan showing the orientation of the axis of greatest horizontal compression, S_{Hmax}, calculated using earthquake focal mechanisms from depths of 0–30

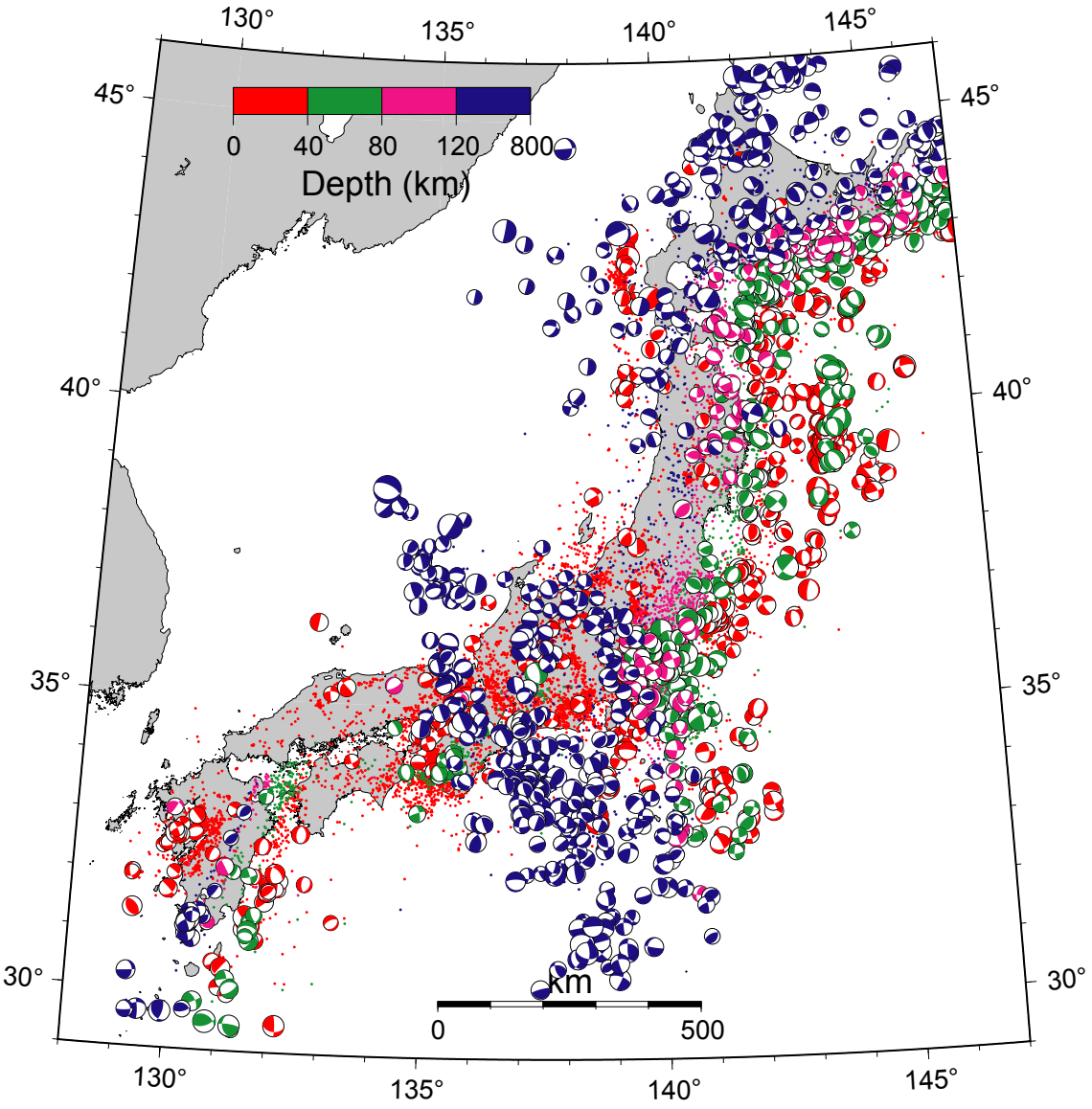

Figure 6.7: Map illustrating the integrated focal mechanism catalog.

km. Only those focal mechanisms with strike, dip, and rake uncertainties of $\leq 10^{\circ}$ have been used to produce these particular results.

Several key points should be noted: (1) S_{Hmax} directions at nearby locations exhibit a high degree of similarity, although S_v is estimated to vary somewhat, generally indicating either normal and strike-slip stress tensor results in close proximity (implying that $S_1 \sim S_2$)

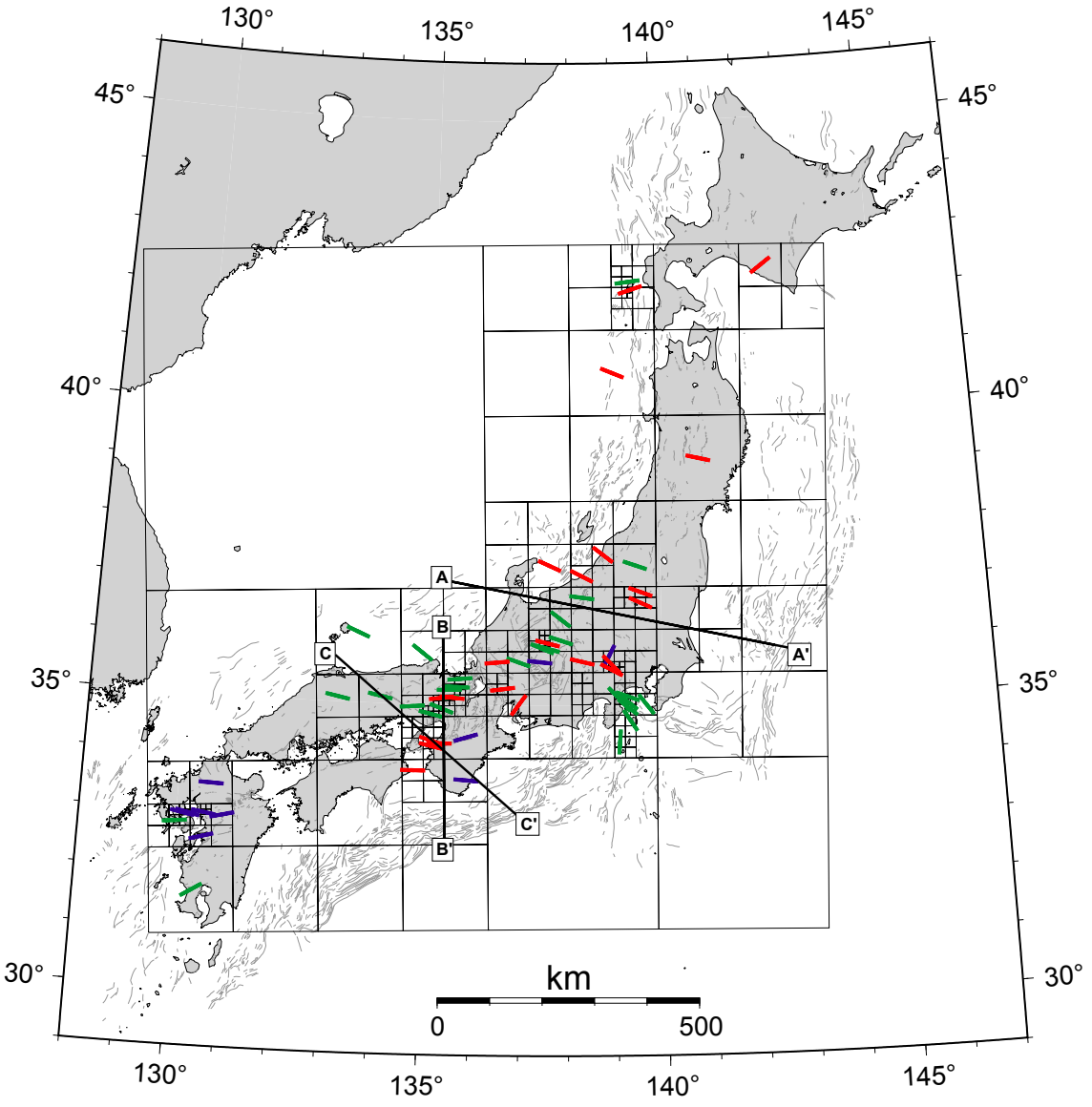

Figure 6.8: Orientations of the axis of greatest horizontal compression (S_{Hmax}) calculated using focal mechanisms with uncertainties in strike, dip, and rake of $\leq 10°$. Red, green, and blue symbols denote reverse, strike-slip, and normal faulting stress tensors respectively.

or alternatively strike-slip and reverse stress tensor results ($S_2 \sim S_3$); (2) northern Honshu and Hokkaido exhibit a systematic SE–NW S_{Hmax} orientation and strike-slip or reverse faulting conditions; (3) S_{Hmax} is oriented approximately ENE–WSW in southwestern Honshu, Shikoku and Kyushu, with strike-slip and reverse faulting predominating in Honshu

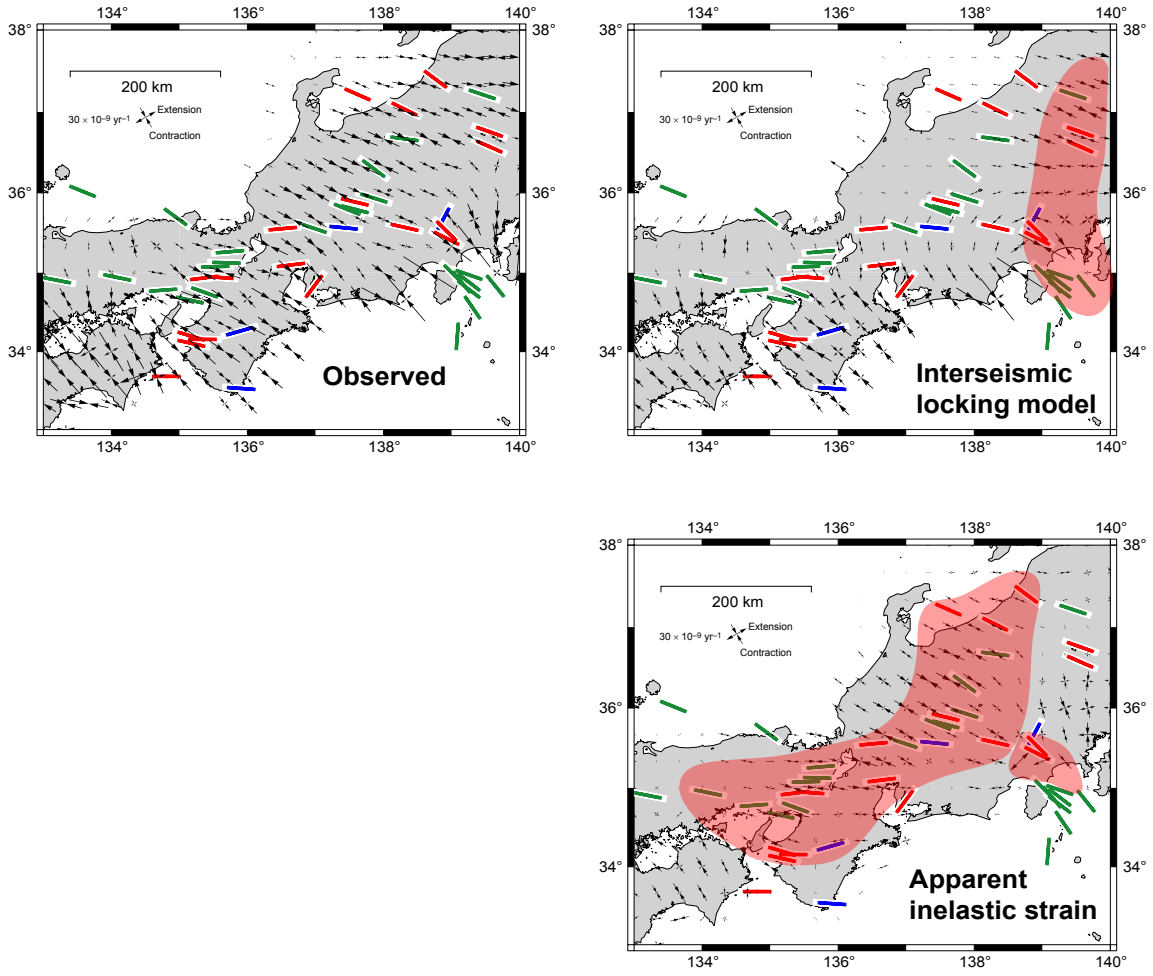

Figure 6.9: S_{Hmax} and strain rate axes (Mazzotti et al., 2001) in central Japan. As in Figure 6.2, the upper left, upper right, and lower right panels correspond to the total observed strain rates, the strain rates associated with the interseismic locking model, and the apparent inelastic (residual) strain rates respectively. Red, green, and blue S_{Hmax} symbols denote reverse, strike-slip, and normal faulting stress tensors respectively. Inward arrows indicate the direction of maximum contraction, and outward arrows the direction of maximum extension. The red shaded patterns demarcate areas of systematic agreement between the axes of greatest compressive stress and greatest contractional strain. IP — Izu Peninsula.

and Shikoku, and strike-slip and normal faulting predominating in Kyushu; (4) S_{Hmax} rotates in central Japan between the orientations characteristic of northern and southwestern Japan, in a fan-shaped pattern emanating from north of the Izu Peninsula.

If the axes of tectonic stress and strain were isotropic at regional scales, we would expect to find that the axes of greatest horizontal compressive stress (S_{Hmax}) and greatest contractional strain were parallel (Figure 6.9). However, visual comparison of the S_{Hmax} results with Mazzotti et al.'s (2001) observed and interseismic locking model strain rate axes reveals a generally poor degree of correspondence between the greatest compressive stress and contractional strain rate directions other than in northern Kanto.

In contrast, a comparison of S_{Hmax} directions with Mazzotti et al.'s (2001) principal axes of apparent inelastic strain reveals a high degree of correlation throughout much of central Japan. Specifically, the fan-shaped rotation of S_{Hmax} in the Chubu and Kinki regions west of 139° is matched by a similar rotation of the axis of greatest contractional apparent inelastic strain, from approximately SE–NW in the northern Japanese Alps (138°E,37°N) to E–W north of the Kii Peninsula (136°E,35°N). Miyazaki and Heki (2001) suggested that the Kii Peninsula is being expelled southward from central Japan, and the normal faulting stress result seems broadly consistent with this. The agreement between the stress and residual strain rate tensor orientations is less convincing elsewhere, particularly in Shikoku, where the trench-parallel orientation of S_{Hmax} is approximately orthogonal to the maximum horizontal contraction direction. The locking model employed by Mazzotti et al. (2001) systematically underestimates horizontal velocities along the southern coast of Shikoku, and therefore produces trench-perpendicular residual contraction at rates higher than observed by other authors (S. Mazzotti, pers. comm. to J. Townend, 2002; see also Mazzotti et al., 2000). Hence the discrepancy between the residual contraction direction and the axis of greatest compressive stress in Shikoku may stem from problems associated with the locking model in that region.

6.5 Stresses Along Vertical Sections

Figures 6.10 and 6.11 are cross-sections illustrating the lateral and vertical variations in stress tensor orientation adjacent to the Japan Trench and Nankai Trough subduction zones, and the associated P wave velocity structure, seismicity, and apparent inelastic strain rate profiles. The cross-section presented in Figure 6.10 crosses northern Kanto and illustrates subduction of the Pacific plate beneath central Japan. A characteristic feature of the Japan

Trench subduction zone is the existence of two planes of seismicity within the down-going slab. The preponderance of normal-faulting focal mechanisms and dinoflagellate cysts within the lower of these two planes is consistent with intraplate extensional strain associated with bending; bending-related strains are also manifest in the normal-faulting focal mechanisms in the outer rise. In contrast, the upper plane of seismicity above $\sim$100 km tends to exhibit reverse-faulting focal mechanisms, which are inferred to reflect compressional stresses related to the subduction thrust and to mask the otherwise anticipated extensional faulting. At depths below 200 km, the focal mechanisms indicate predominantly down-dip tension, which is presumably related to the weight of the slab.

Seismicity landward of the trench (540 km) is relatively sparse, and no stress results have been obtained in this zone. Onshore, however, abundant seismicity indicates the existence of a mixed strike-slip/reverse stress state. Along this cross-section, the transition between reverse and strike-slip stresses anticipated on the basis of Nakamura and Uyeda's (1980) stress gradient model is not clearly resolved. It corresponds, however to a distinctive minimum in the along-profile $\dot{e}_{xx}$ component of residual strain rate, implying along-profile shortening.

Figure 6.11 illustrates the shallow subduction of the Philippine Sea plate beneath central Japan along two sections, one oriented north–south (B–B') and the other parallel to the velocity of the Philippine Sea plate with respect to the Amurian plate (C–C'). The slab-bending effects observed in the Pacific plate in Figure 6.10 are not seen in either of these cross-sections, presumably reflecting the lower angle of subduction. What is noticeable in both profiles, however, is the existence of a reverse stress state in the upper plate above the slab (as defined by seismicity) and a strike-slip stress state further inland. The transition is particularly clear in B–B', which is oriented almost perpendicular to the direction of S_{Hmax} (S_1); the strike-slip stress regime corresponds to a zone of east–west residual contraction (negative $\dot{e}_{yy}$). Section C–C', which is oriented approximately northwest–southeast, does not exhibit such a clear transition between a reverse-faulting stress state close to the trench and a strike-slip stress state further inland. The residual strain rate data along C–C' indicate contraction perpendicular to the trench in Shikoku (negative $\dot{e}_{xx}$), although as noted above the elastic locking model systematically produces higher than expected contraction rates in this direction in Shikoku.

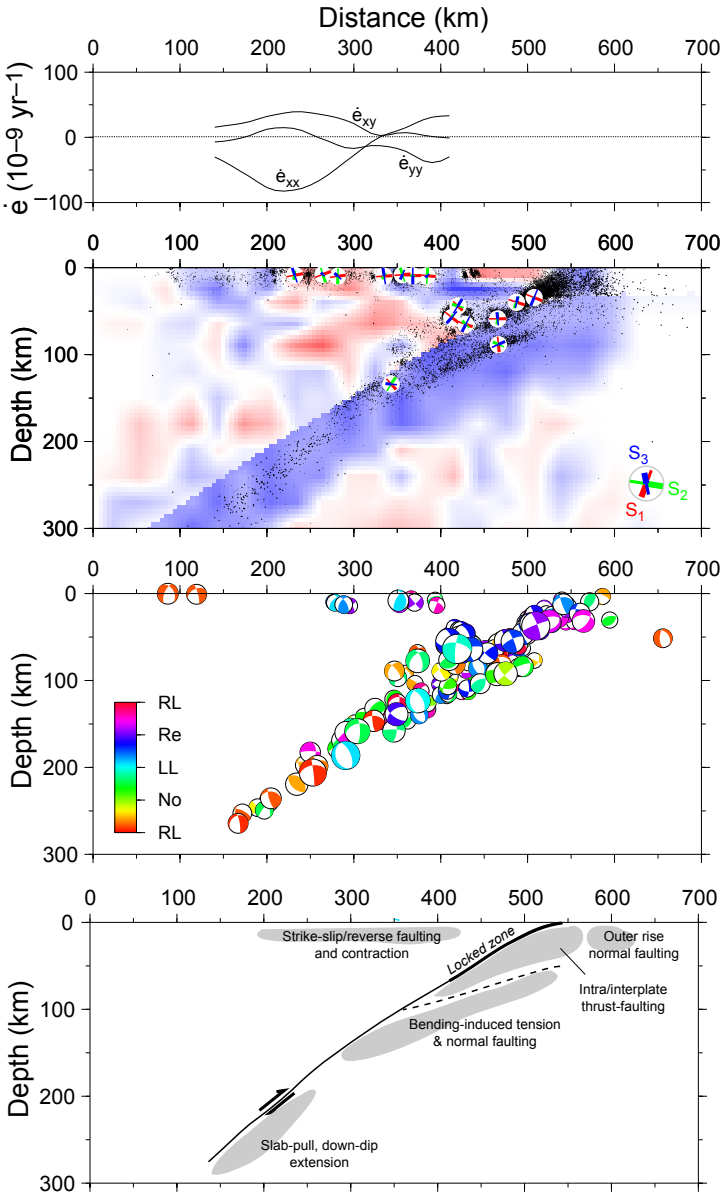

Figure 6.10: Seismicity, apparent inelastic strain rates, and stress tensor orientations along cross-section A–A' (Figure 6.8). From top to bottom: (i) apparent inelastic (residual) strain rate components in coordinates along (x) and perpendicular to (y) the cross-section (Mazzotti et al., 2001); (ii) tomographic P velocity model (blue and red indicate fast and slow, respectively; D. Zhao, pers. comm. to J. Townend, 2002: see Zhao et al., 2002, and references therein), seismicity (merged catalog locations), and stress inversion results; (iii) representative focal mechanisms (**M** 3+), colored by rake, and; (iv) schematic interpretation of the seismicity and stress results.

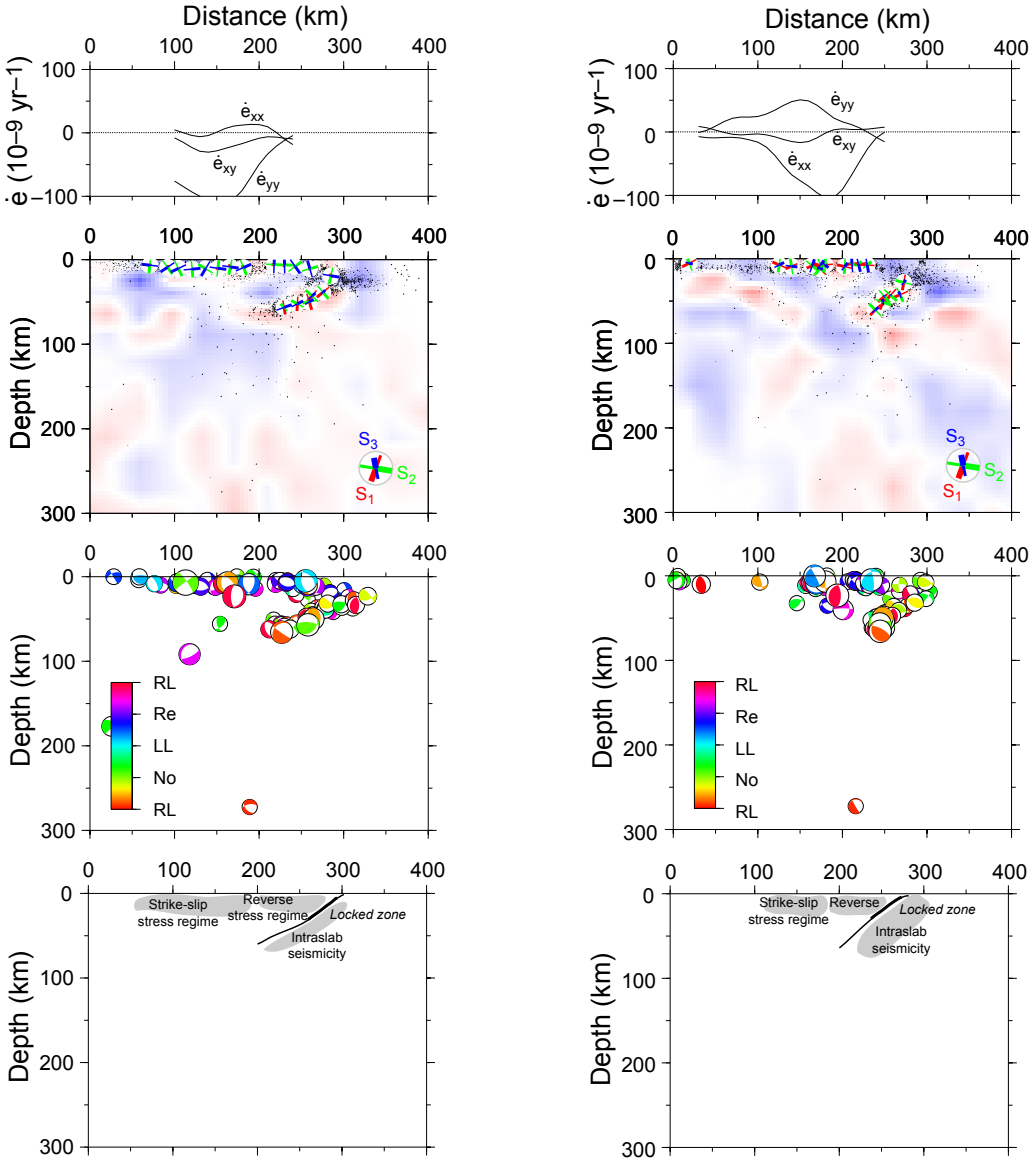

Figure 6.11: Seismicity, apparent inelastic strain rates, and stress tensor orientations along cross-section B–B' (left) and C–C (right; Figure 6.8). C–C' is approximately parallel to the relative plate motion vector of the Philippine Sea plate with respect to the Amurian plate. From top to bottom: (i) apparent inelastic (residual) strain rate components in coordinates along (x) and perpendicular to (y) the cross-section (Mazzotti et al., 2001); (ii) tomographic P velocity model (blue and red indicate fast and slow, respectively; D. Zhao, pers. comm. to J. Townend, 2002: see Zhao et al., 2002, and references therein), seismicity (merged catalog locations), and stress inversion results; (iii) representative focal mechanisms (**M** 3+), colored by rake, and; (iv) schematic interpretation of the seismicity and stress results.

6.6 Summary

In Section 6.2.3 we asserted that the residual strain rate fields obtained by Mazzotti et al. (2001) and Miyazaki and Heki (2001) by subtracting deformation associated with models of interseismic subduction thrust locking from the total observed deformation field were compatible with geological and geomorphic data suggesting that crustal collision occurs between the Amurian plate and northeastern Honshu in central Japan. The horizontal stress results described in Section 6.4 suggest, moreover, that the tectonic stress field manifest in crustal seismicity is oriented such that S_{Hmax} is generally parallel to the axis of greatest contractional apparent inelastic strain rate throughout much of central and southwestern Japan, rather than to the corresponding axis of total strain rate, which incorporates the effects of the interseismic locking.

The correspondence between the axes of greatest horizontal compression and greatest apparent inelastic contraction suggests that the state of crustal stress in central Japan is primarily associated with strain occurring within the upper plate in response to crustal collision rather than with interseismic strain accumulation. Specifically, the collision of the Amurian plate with northeastern Japan, manifest by a zone of high contractional strain rates extending northeastwards from the Kinki region to the northern Japanese Alps, appears to be consistent with the overall pattern of horizontal stress in central Japan.

Shallow angles of subduction ("flat subduction") such as exist in the eastern Nankai Trough, may cause compressional stresses to be transmitted far into the upper plate as a consequence of the force balance on the slab (Wang and He, 1999; Gutscher et al., 2000). To what extent this is an important factor in central and southwestern Japan is unresolved, but further comparisons of the stress and residual strain rate data may elucidate this. It should be emphasized that both the residual strain rate results obtained by Mazzotti et al. (2001) and Miyazaki and Heki (2001) and the stress orientation data illustrated in Figures 6.8 and 6.9 reflect net inelastic deformation. Consequently, two separate mechanisms — crustal collision in the upper plate and stress guide transmission along the shallowly dipping slab beneath — may be responsible for the overall mechanical behavior of central and southwestern Japan, and a more detailed treatment of the kinetic and kinematic data is required to discriminate them.

Notwithstanding the comments of the previous paragraph and Section 6.2.3, stresses associated with seismogenic locking of the subduction interface appear not to be manifest in upper plate seismicity, despite the large strain rates with which they are associated. In contrast, stresses within the upper plane of seismicity extending down the Nankai Trough subduction zone are typically oriented so that the principal subduction thrust is subject to low shear tractions. As concluded by the authors listed in Table 6.1 with respect to subduction zones elsewhere, this indicates that the slab's upper boundary approximates a free surface. The results obtained to date do not reveal systematic down-dip or along-strike variations in the orientation of the stress tensor; future work is planned to investigate whether such variations exist.

Wang (2000) suggested that the subduction interface must be frictionally weak if S_{Hmax} orientations within the forearc deviate from trench-normal. This condition may be necessary for other than trench-normal S_{Hmax} orientations, but it does not appear to be a sufficient condition; that is, subduction interfaces have been found to be weak wherever investigated (see Table 6.1) but in not all cases does S_{Hmax} deviate from an approximately trench-normal orientation. In the case of southwestern Japan, trench-parallel compression may have more to do with crustal collision in central Japan than with forearc stress gradients associated with a weak subduction thrust. Nevertheless, Figure 6.11 does illustrate the expected transition in the central Nankai Trough from a reverse-faulting stress orientation near the trench to strike-slip faulting further inland, and cross-sections through northern Honshu (not shown here) also reveal the reverse/strike-slip transition expected on the basis of Nakamura and Uyeda's (1980) model of horizontal stress gradients.

The work described in this chapter is preliminary, and further research is required to make full use of the newly acquired seismicity catalog. The abundance of geodetic data offers strong possibilities for investigating the relative significance of different sources of crustal stress — flat subduction and intra-arc collision — in a similar way to that described for California in Chapters 4 and 5. Moreover, the improvements in effective station geometry obtained by merging data from separate networks suggest that the integrated seismicity catalog will prove useful for relocations with HYPODD (Waldhauser and Ellsworth, 2000). With refined earthquake locations and focal mechanisms, we intend to compute stress orientations with better spatial resolution than achieved to date, and to look specifically at

the transition within the fore-arc from slab-dominated stress orientations in the subduction zone to the apparently collision-dominated stress orientations characteristic of the upper plate.

Acknowledgments

The scientific and logistical support of the Japan Marine Science and Technology Center (JAMSTEC), and Toshitaka Baba, Phil Cummins (now at Geoscience Australia), Takane Hori, and Yoshiyuki Kaneda in particular, is gratefully acknowledged. We thank Shozo Matsumura (National Research Institute for Earth Science and Disaster Prevention), Hiroshi Tsuruoka (Earthquake Research Institute), and Koichi Uhira (Japan Meteorological Agency) for their assistance in acquiring the seismicity data, Shin'ichi Miyazaki (University of Tokyo) and Stéphane Mazzotti (Geological Survey of Canada) for kindly sharing their residual velocity and strain rate data, and Dapeng Zhao (Ehime University) for the use of his tomographic velocity model. This work was supported in part by a Lieberman Fellowship from Stanford University.

Bibliography

Abers, G. A. and Gephart, J. W. (2001). Direct inversion of earthquake first motions for both the stress tensor and focal mechanisms and application to southern California. *Journal of Geophysical Research*, 106:26523–26540.

Anderson, J. G. (1986). Seismic strain rates in the central and eastern United States. *Bulletin of the Seismological Society of America*, 76:273–290.

Ando, M. (1975). Source mechanisms and tectonic significance of historical earthquakes along the Nankai Trough, Japan. *Tectonophysics*, 27:119–140.

Angelier, J. (1979). Determination of the mean principal directions of stresses for a given fault population. *Tectonophysics*, 56:T17–T26.

Angelier, J. (1984). Tectonic analysis of fault slip data sets. *Journal of Geophysical Research*, 89:5835–5848.

Argus, D. F. and Gordon, R. G. (1991). Current Sierra Nevada–North America motion from very long baseline interferometry: implications for the kinematics of the western United States. *Geology*, 19:1085–1088.

Baba, T., Hori, T., Hirano, S., Cummins, P., Park, J.-O., Kameyama, M., and Kaneda, Y. (2001). Deformation of a seamount subducting beneath an accretionary prism: constraints from numerical simulation. *Geophysical Research Letters*, 28:1827–1830.

Barton, C. A., Hickman, S. H., Morin, R., and Zoback, M. D. (1995). Fluid flow along potentially active faults in crystalline rock. *Geology*, 23:683–686.

Barton, C. A., Hickman, S. H., Morin, R., Zoback, M. D., and Benoit, D. (1998). Reservoir-scale fracture permeability in the Dixie Valley, Nevada, geothermal field. In *Abstract Volume*, pages 315–322, Trondheim. Society of Petroleum Engineers.

Barton, C. A., Zoback, M. D., and Burns, K. L. (1988). In situ stress orientation and magnitude at the Fenton Hill geothermal site, New Mexico, determined from wellbore breakouts. *Geophysical Research Letters*, 15:467–470.

Batchelor, A. S. and Pine, R. J. (1986). The results of in situ stress determinations by seven methods to depths of 2500 m in the Carnmenellis granite. In *International Symposium on Rock Stress and Rock Stress Measurements*, pages 467–478, Stockholm.

Baumgärtner, J., Gérard, A., Baria, R., Jung, R., Tran-Viet, T., Gandy, T., Aquilina, L., and Garnish, J. (1998). Circulating the HDR reservoir at Soultz: maintaining production and injection flow in complete balance, initial results of the 1997 circulation experiment. In *Twenty-Third Workshop on Geothermal Reservoir Engineering*, pages 11–20, Stanford.

Borevsky, L. V., Vartanyan, G. S., and Kulikov, T. B. (1987). Hydrogeological essay. In Kozlovsky, Y. A., editor, *The Superdeep Well of the Kola Peninsula*, pages 271–287. Springer, New York.

Bott, M. H. P. and Kusznir, N. J. (1984). The origin of tectonic stress in the lithosphere. *Tectonophysics*, 105:1–13.

Brace, W. F. (1980). Permeability of crystalline and argillaceous rocks. *International Journal of Rock Mechanics and Mining Sciences*, 17:241–251.

Brace, W. F. and Kohlstedt, D. (1980). Limits on lithospheric stress imposed by laboratory measurements. *Journal of Geophysical Research*, 74:6248–6252.

Brudy, M., Zoback, M. D., Fuchs, K., Rummel, F., and Baumgärtner, J. (1997). Estimation of the complete stress tensor to 8 km depth in the KTB scientific drill holes: implications for crustal strength. *Journal of Geophysical Research*, 102:18453–18475.

Brune, J. N., Henyey, T. L., and Roy, R. F. (1969). Heat flow, stress, and rate of slip along the San Andreas fault, California. *Journal of Geophysical Research*, 74:3821–3827.

Byerlee, J. D. (1978). Friction of rocks. *Pure and Applied Geophysics*, 116:615–626.

Carter, N. L. and Tsenn, M. C. (1987). Flow properties of continental lithosphere. *Tectonophysics*, 136:27–63.

Castillo, D. A. and Zoback, M. D. (1995). Systematic stress variations in the southern San Joaquin Valley and along the White Wolf fault: implications for the rupture mechanics of the 1952 M_S 7.8 Kern County earthquake and contemporary seismicity. *Journal of Geophysical Research*, 100:6249–6264.

Chapman, D. S. and Furlong, K. P. (1992). Thermal state of the continental lower crust. In Fountain, D. M., Arculus, R., and Kay, R. W., editors, *Continental Lower Crust*, pages 179–199. Elsevier, Amsterdam.

Chen, W.-P. and Molnar, P. (1983). Focal depths of intracontinental and intraplate earthquakes and their implications for the thermal and mechanical properties of the lithosphere. *Journal of Geophysical Research*, 88:4183–4214.

Chéry, J., Zoback, M. D., and Hassani, R. (2001). An integrated mechanical model of the San Andreas fault in central and northern California. *Journal of Geophysical Research*, 106:22051–22066.

Christensen, N. I. and Mooney, W. D. (1995). Seismic velocity structure and composition of the continental crust: a global view. *Journal of Geophysical Research*, 100:9761–9788.

Clauser, C. (1991). Permeabilität kristalliner Gesteine. Report 107776, Niedersächsisches Landesamt für Bodenforschung (NLfB), Hannover. In German.

Coyle, B. J. and Zoback, M. D. (1988). In situ permeability and fluid pressure measurements at $\sim$2 km depth in the Cajon Pass research well. *Geophysical Research Letters*, 15:1029–1032.

Cummins, P. and Kaneda, Y. (2000). Possible splay fault slip during the 1946 Nankai earthquake. *Geophysical Research Letters*, 27:2725–2728.

Delouis, B., Cisternas, A., Dorbath, L., Rivera, L., and Kausel, E. (1996). The Andean subduction zone between 22°s and 24°s (northern Chile): precise geometry and state of stress. *Tectonophysics*, 259:81–100.

DeMets, C., Gordon, R., Argus, D., and Stein, S. (1994). Effect of recent revisions to the geomagnetic reversal time scale on estimates of current plate motions. *Geophysical Research Letters*, 21:2191–2194.

DeMets, C., Gordon, R. G., Argus, D. F., and Stein, S. (1990). Current plate motions. *Geophysical Journal International*, 101:425–478.

England, P. C. and Houseman, G. A. (1986). Finite strain calculations of continental deformation. 2. Comparison with the India–Aasia collision zone. *Journal of Geophysical Research*, 91:3664–3676.

Fleitout, L. and Froidevaux, C. (1982). Tectonics and topography for a lithosphere containing density heterogeneities. *Tectonics*, 1:21–56.

Flesch, L. M., Haines, A. J., and Holt, W. E. (2001). Dynamics of the India–Eurasia collision zone. *Journal of Geophysical Research*, 106:16435–16460.

Flesch, L. M., Holt, W. E., Haines, A. J., and Shen-Tu, B. (2000). Dynamics of the Pacific–North American plate boundary in the western United States. *Science*, 287:834–836.

Forsyth, D. W. and Uyeda, S. (1975). On the relative importance of the driving forces of plate motion. *Geophysical Journal of the Royal Astronomical Society*, 43:163–200.

Fuchs, K. and Müller, B. (2001). World Stress Map of the Earth: a key to tectonic processes and technological applications. *Naturwissenschaften*, 88:357–371.

Gephart, J. W. (1990a). FMSI: Fortran program for inverting fault/slickenside and earthquake focal mechanism data to obtain the regional stress tensor. *Computers and Geosciences*, 16:953–989.

Gephart, J. W. (1990b). Stress and the direction of slip on fault planes. *Tectonics*, 9:845–858.

Gephart, J. W. and Forsyth, D. W. (1984). An improved method for determining the regional stress tensor using earthquake focal mechanism data: application to the San Fernando earthquake sequence. *Journal of Geophysical Research*, 89:9305–9320.

Gordon, R. G. (1998). The plate tectonic approximation: plate nonrigidity, diffuse plate boundaries, and global plate reconstructions. *Annual Review of Earth and Planetary Sciences*, 26:615–642.

Gutscher, M., Spakman, W., Bijwaard, H., and Engdahl, E. R. (2000). Geodynamics of flat subduction: seismicity and tomographic constraints from the Andean margin. *Tectonics*, 19:814–833.

Hardebeck, J. L. and Hauksson, E. (1999). Role of fluids in faulting inferred from stress field signatures. *Science*, 285:236–239.

Hartse, H. E., Fehler, M. C., Aster, R. C., Scott, J. S., and Vernon, F. L. (1994). Small-scale stress heterogeneity in the Anza seismic gap, southern California. *Journal of Geophysical Research*, 99:6801–6818.

Hassani, R., Jongmans, D., and Chéry, J. (1997). Study of plate deformation and stress in subduction zone processes using two-dimensional numerical models. *Journal of Geophysical Research*, 108:17951–17965.

Hauksson, E. (2000). Crustal structure and seismicity distributions adjacent to the Pacific and North America plate boundary in southern California. *Journal of Geophysical Research*, 105:13875–13903.

Healy, J. H., Rubey, W. W., Griggs, D. T., and Raleigh, C. B. (1968). The Denver earthquakes. *Science*, 161:1301–1310.

Heki, K., Miyazaki, S., Takahashi, H., Kasahara, M., Kimata, F., Miura, S., Vasilenko, N., Ivashchenko, A., and An, K. (1999). The Amurian plate motion and current plate kinematics in eastern Asia. *Journal of Geophysical Research*, 104:29147–29155.

Henry, P., Mazzotti, S., and Le Pichon, X. (2001). Transient and permanent deformation of central Japan estimated by GPS: 1. Interseismic loading and subduction kinematics. *Earth and Planetary Science Letters*, 184:443–453.

Hickman, S. H., Barton, C. A., Zoback, M. D., Morin, R., Sass, J., and Benoit, R. (1997). In situ stress and fracture permeability along the Stillwater fault zone, Dixie Valley, Nevada. *International Journal of Rock Mechanics and Mining Sciences*, 34:414.

Houseman, G. A. and England, P. C. (1996). Finite strain calculations of continental deformation. 1. Method and general results for convergent zones. *Journal of Geophysical Research*, 91:3651–3663.

Hubbert, M. K. and Rubey, W. W. (1959). Role of fluid pressure in the mechanics of overthrust faulting. *Geological Society of America Bulletin*, 70:115–205.

Huenges, E., Erzinger, J., Kück, J., Engeser, B., and Kessels, W. (1997). The permeable crust: geohydraulic properties down to 9101 m depth. *Journal of Geophysical Research*, 102:18255–18265.

Hyndman, R., Wang, K., and Yamano, M. (1995). Thermal constraints on the seismogenic portion of the southwestern Japan subduction thrust. *Journal of Geophysical Research*, 100:15373–15392.

Hyndman, R., Yamano, M., and Oleskevich, D. (1997). The seismogenic zone of subduction thrust faults. *The Island Arc*, 6:244–260.

Ishibashi, K. (1981). Specification of a soon-to-occur seismic faulting in the Tokai district, central Japan, based upon seismotectonics. In Simpson, D. and Richards, P., editors, *Earthquake prediction: an international review*, number 4 in Maurice Ewing Series, pages 297–332. American Geophysical Union, Washington D.C.

Ishibashi, K. and Satake, K. (1998). Problems on forecasting great earthquakes in the subduction zones around Japan by means of paleoseismology. *Zisin*, 50:1–21. In Japanese.

Ishida, M. (1992). Geometry and relative motion of the Philippine Sea plate and Pacific plate beneath the Kanto–Tokai district, Japan. *Journal of Geophysical Research*, 97:489–513.

Ito, T. and Zoback, M. D. (2000). Fracture permeability and in situ stress to 7 km depth in the KTB scientific drillhole. *Geophysical Research Letters*, 27:1045–1048.

Jaeger, J. C. and Cook, N. G. W. (1979). *Fundamentals of Rock Mechanics*. Chapman and Hall, London.

Jaupart, C., Mareschal, J. C., Guillou-Frottier, L., and Davaille, A. (1998). Heat flow and thickness of the lithosphere in the Canadian shield. *Journal of Geophysical Research*, 103:15629–15286.

Jones, C. H., Sonder, L. J., and Unruh, J. R. (1996). The role of gravitational potential energy in active deformation in the southwestern United States. *Nature*, 381:37–41.

Jones, L. M. (1988). Focal mechanisms and the state of stress on the San Andreas fault in Southern California. *Journal of Geophysical Research*, 93:8869–8891.

Kanamori, H. and Anderson, D. L. (1975). Theoretical basis of some empirical relations in seismology. *Bulletin of the Seismological Society of America*, 65:1073–1095.

Karato, S. and Wu, P. (1993). Rheology of the upper mantle: a synthesis. *Science*, 260:771–778.

Klein, F. (2002). User's guide to HYPOINVERSE-2000, a Fortran program to solve for earthquake locations and magnitudes. Open File Report 02-171, United States Geological Survey. Version 1.0.

Kohlstedt, D. L., Evans, B., and Mackwell, S. J. (1995). Strength of the lithosphere: constraints imposed by laboratory experiments. *Journal of Geophysical Research*, 100:17587–17602.

Kukkonen, I. T. and Clauser, C. (1994). Simulation of heat transfer at the Kola deep-hole site: implications for advection, heat refraction, and paleoclimatic effects. *Geophysical Journal International*, 116:409–420.

Kurogi, A. (1999). Chuubu chihouka no ouryokuba ni kan suru kenkyuu. Graduation research report, Ehime University. In Japanese.

Kusznir, N. J. (1991). The distribution of stress with depth in the lithosphere: thermo-rheological and geodynamic constraints. In Whitmarsh, R. B., editor, *Tectonic Stress in the Lithosphere*, pages 95–107. Royal Society, London.

Lachenbruch, A. H. and McGarr, A. (1990). Stress and heat flow. *United States Geological Survey Professional Paper*, 1515:261–277.

Lachenbruch, A. H. and Sass, J. H. (1980). Heat flow and energetics of the San Andreas fault zone. *Journal of Geophysical Research*, 85:6185–6223.

Lachenbruch, A. H. and Sass, J. H. (1992). Heat flow from Cajon Pass, fault strength, and tectonic implications. *Journal of Geophysical Research*, 97:4995–5015.

Lewis, J. C., Unruh, J. R., and Twiss, R. J. (2003). Seismogenic strain and motion of the Oregon coast block. *Geology*, 31:183–186.

Liu, L. and Zoback, M. D. (1997). Lithospheric strength and intraplate seismicity in the New Madrid seismic zone. *Tectonics*, 16:585–595.

Lockner, D. A., Hickman, S. H., Kuksenko, V. S., Ponomarev, A. V., Sidorin, A., Byerlee, J. D., and Khakaev, B. (1991). Laboratory-determined permeability of cores from the Kola superdeep well. *Geophysical Research Letters*, 18:881–884.

Lu, Z., Wyss, M., and Pulpan, H. (1997). Details of stress directions in the Alaska subduction zone from fault plane solutions. *Journal of Geophysical Research*, 102:5385–5402.

Lund, B. and Zoback, M. D. (1999). Orientation and magnitude of in situ stress to 6.5 km depth in the Baltic Shield. *International Journal of Rock Mechanics and Mining Sciences*, 36:169–190.

Magee, M. and Zoback, M. (1993). Evidence for a weak interplate thrust fault along the northern Japan subduction zone and implications for the mechanics of thrust faulting and fluid expulsion. *Geology*, 21:809–812.

Manning, C. E. and Ingebritsen, S. E. (1999). Permeability of the continental crust: implications of geothermal data and metamorphic systems. *Reviews of Geophysics*, 37:127–150.

Mazzotti, S., Henry, P., and Le Pichon, X. (2001). Transient and permanent deformation of central Japan estimated by GPS: 2. strain partitioning and arc-arc collision. *Earth and Planetary Science Letters*, 184:455–469.

Mazzotti, S., Henry, P., Le Pichon, X., and Sagiya, T. (1999). Strain partitioning in the zone of transition from Nankai subduction to IzuBonin collision (central Japan): implications for an extensional tear within the subducting slab. *Earth and Planetary Science Letters*, 172:1–10.

Mazzotti, S., Le Pichon, X., Henry, P., and Miyazaki, S. (2000). Full interseismic locking of the Nankai and Japan-west Kurile subduction zones: an analysis of uniform elastic strain accumulation in Japan constrained by permanent GPS. *Journal of Geophysical Research*, 105:13159–13177.

McGarr, A. (1988). On the state of lithospheric stress in the absence of applied tectonic forces. *Journal of Geophysical Research*, 93:13609–13617.

McGarr, A. and Gay, N. C. (1978). State of stress in the Earth's crust. *Annual Review of Earth and Planetary Sciences*, 6:405–436.

McGinty, P., Reyners, M., and Robinson, R. (2000). Stress directions in the shallow part of the Hikurangi subduction zone, New Zealand, from the inversion of earthquake first motions. *Geophysical Journal International*, 142:339–350.

McKenzie, D. (1969). The relationship between fault plane solutions for earthquakes and the directions of the principal stresses. *Bulletin of the Seismological Society of America*, 59:591–601.

McNutt, M. K. (1984). Lithospheric flexure and thermal anomalies. *Journal of Geophysical Research*, 89:1180–1194.

Michael, A. J. (1984). Determination of stress from slip data: faults and folds. *Journal of Geophysical Research*, 89:11517–11526.

Michael, A. J. (1987). Use of focal mechanisms to determine stress: a control study. *Journal of Geophysical Research*, 92:357–368.

Miyazaki, S. and Heki, K. (2001). Crustal velocity field of southwest Japan: subduction and arc–arc collision. *Journal of Geophysical Research*, 106:4305–4326.

Morrow, C. A. and Byerlee, J. D. (1988). Permeability of rock samples from Cajon Pass, California. *Geophysical Research Letters*, 15:1033–1036.

Morrow, C. A. and Byerlee, J. D. (1992). Permeability of core samples from Cajon Pass scientific drill hole: results from 2100 to 3500 m depth. *Journal of Geophysical Research*, 97:5145–5151.

Morrow, C. A., Lockner, D. A., Hickman, S. H., Rusanov, M., and Röckel, T. (1994). Effects of lithology and depth on the permeability of core samples from the Kola and KTB drill holes. *Journal of Geophysical Research*, 99:7263–7274.

Mount, V. S. and Suppe, J. (1987). State of stress near the San Andreas fault: implications for wrench tectonics. *Geology*, 15:1143–1146.

Nakamura, K. and Uyeda, S. (1980). Stress gradient in arcback arc regions and plate subduction. *Journal of Geophysical Research*, 85:6419–6428.

Nur, A. and Walder, J. (1990). Time-dependent hydraulics of the Earth's crust. In Bredehoeft, J. D. and Norton, D. L., editors, *The Role of Fluids in Crustal Processes*, pages 113–127. National Academy Press, Washington, D. C.

Oppenheimer, D. H., Reasenberg, P. A., and Simpson, R. W. (1988). Fault plane solutions for the 1984 Morgan Hill, California, earthquake sequence: evidence for the state of stress on the Calaveras fault. *Journal of Geophysical Research*, 93:9007–9026.

Page, B. M., Thompson, G. A., and Coleman, R. G. (1998). Late Cenozoic tectonics of the central and southern Coast Ranges of California. *Geological Society of America Bulletin*, 110:846–876.

Park, J., Tsuru, T., Kaneda, Y., Kono, Y., Kodaira, S., Takahashi, N., and Kinoshita, H. (1999). A subducting seamount beneath the Nankai accretionary prism off Shikoku, southwestern Japan. *Geophysical Research Letters*, 26:931–934.

Petersen, M. D. and Wesnousky, S. G. (1994). Fault slip rates and earthquake histories for active faults in southern California. *Bulletin of the Seismological Society of America*, 84:1608–1649.

Pine, R. J., Ledingham, P., and Merrifield, C. M. (1983). In situ stress in the Carnmenellis Granite. ii. hydrofracture tests at Rosemanowes Quarry to depths of 2000 m. *International Journal of Rock Mechanics and Mining Sciences*, 20:63–72.

Pollack, H. N. and Chapman, D. S. (1977). On the regional variation of heat flow, geotherms, and lithospheric thickness. *Tectonophysics*, 38:279–296.

Pollack, H. N., Hurter, S. J., and Johnson, J. R. (1993). Heat flow from the Earth's interior; analysis of the global data set. *Reviews of Geophysics*, 31:267–280.

Provost, A.-S. and Houston, H. (2001). Orientation of the stress field surrounding the creeping section of the San Andreas fault: evidence for a narrow mechanically weak fault zone. *Journal of Geophysical Research*, 106:11373–11386.

Raleigh, C. B., Healy, J. H., and Bredehoeft, J. D. (1972). Faulting and crustal stress at Rangely, Colorado. *American Geophysical Union Monograph*, 16:275–284.

Ranalli, G. and Murphy, D. C. (1987). Rheological stratification of the lithosphere. *Tectonophysics*, 132:281–295.

Reasenberg, P. A. and Oppenheimer, D. (1985). FPFIT, FPPLOT, and FPPAGE: Fortran computer programs for calculating and displaying earthquake fault-plane solutions. Open File Report 85-739, United States Geological Survey.

Rice, J. R. (1992). Fault stress states, pore pressure distributions, and the weakness of the San Andreas fault. In Evans, B. and Wong, T.-F., editors, *Fault mechanics and transport properties of rocks*, pages 475–503. Academic Press.

Roeloffs, E. (1988). Fault stability changes induced beneath a reservoir with cyclic variations in water level. *Journal of Geophysical Research*, 93:2107–2124.

Roeloffs, E. (1996). Poroelastic techniques in the study of earthquake-related hydrologic phenomena. *Advances in Geophysics*, 37:135–195.

Rudnick, R. L., McDonough, W. F., and O'Connell, R. J. (1998). Thermal structure, thickness, and composition of continental lithosphere. *Chemical Geology*, 145:395–411.

Sagiya, T., Miyazaki, S., and Tada, T. (2000). Continuous GPS array and present-day deformation of Japan. *Pure and Applied Geophysics*, 157:2303–2322.

Sagiya, T. and Thatcher, W. (1999). Coseismic slip resolution along a plate boundary megathrust: the Nankai Trough, southwest Japan. *Journal of Geophysical Research*, 104:1111–1129.

Sasaki, S. (1998). Characteristics of microseismic events induced during hydraulic fracturing experiments at the Hijori hot dry rock geothermal energy site, Yamagata, Japan. *Tectonophysics*, 289:171–188.

Satake, K. (1993). Depth distribution of coseismic slip along the Nankai Trough, Japan, from joint inversion of geodetic and tsunami data. *Journal of Geophysical Research*, 98:4553–4565.

Savage, J. (1983). A dislocation model of strain accumulation and release at a subduction zone. *Journal of Geophysical Research*, 88:4984–4996.

Savage, J. (1995). Interseismic uplift at the Nankai subduction zone, southwest Japan, 19511990. *Journal of Geophysical Research*, 100:6339–6350.

Savage, J. and Thatcher, W. (1992). Interseismic deformation at the Nankai Trough, Japan, subduction zone. *Journal of Geophysical Research*, 97:11117–11135.

Schaff, D. P., Bokelmann, G. H. R., Beroza, G. C., Waldhauser, F., and Ellsworth, W. L. (2002). High resolution image of Calaveras fault seismicity. *Journal of Geophysical Research*, 107(1027, doi: 10.1029/2000WR000112).

Schatz, J. P. and Simmons, G. (1972). Thermal conductivity of earth materials at high temperatures. *Journal of Geophysical Research*, 77:6966–6983.

Scholz, C. H. (2000). Evidence for a strong San Andreas fault. *Geology*, 28:163–166.

Seno, T. (1999). Syntheses of the regional stress fields of the Japanese islands. *The Island Arc*, 8:66–79.

Shapiro, S. A., Audigane, P., and Royer, J.-J. (1999). Large-scale in situ permeability tensor of rocks from induced microseismicity. *Geophysical Journal International*, 137:207–213.

Shapiro, S. A., Huenges, E., and Borm, G. (1997). Estimating the crust permeability from fluid-injection-induced seismic emission at the KTB site. *Geophysical Journal International*, 131:F15–F18.

Shiono, K., Mikumo, T., and Ishikawa, Y. (1980). Tectonics of the KyushuRyukyu arc as evidenced from seismicity and focal mechanisms of shallow to intermediate-depth earthquakes. *Journal of Physics of the Earth*, 28:17–43.

Sibson, R. H. (1974). Frictional constraints on thrust, wrench and normal faults. *Nature*, 249:542–544.

Sibson, R. H. (1983). Continental fault structure and the shallow earthquake source. *Journal of the Geological Society of London*, 5:741–767.

Simpson, D. W., Leith, W. S., and Scholz, C. H. (1988). Two types of reservoir-induced seismicity. *Bulletin of the Seismological Society of America*, 78:2025–2040.

Stein, R. S., Barka, A. A., and Dieterich, J. H. (1997). Progressive failure on the North Anatolian fault since 1939 by earthquake stress triggering. *Geophysical Journal International*, 128:594–604.

Stein, R. S., King, G. C., and Lin, J. (1992). Change in failure stress on the southern San Andreas fault system caused by the 1992 magnitude=7.4 Landers earthquake. *Science*, 258:1328–1332.

Talwani, P., Cobb, J. S., and Schaeffer, M. F. (1999). In situ measurements of hydraulic properties of a shear zone in northwestern South Carolina. *Journal of Geophysical Research*, 104:14993–15003.

Thatcher, W., Hileman, J. A., and Hanks, T. C. (1975). Seismic slip distribution along the San Jacinto fault zone, southern California, and its implications. *Geological Society of America Bulletin*, 86:1140–1146.

Thatcher, W. and Matsuda, T. (1981). Quaternary and geodetically measured crustal movements in the Tokai district, central Honshu, Japan. *Journal of Geophysical Research*, 86:9237–9247.

Townend, J. and Zoback, M. D. (2000). How faulting keeps the crust strong. *Geology*, 28:399–402.

Townend, J. and Zoback, M. D. (2001). Implications of earthquake focal mechanisms for the frictional strength of the San Andreas fault system. In Holdsworth, R. E., Strachan, R. A., Macloughlin, J., and Knipe, R. J., editors, *The Nature and Significance of Fault Zone Weakening*, volume 186, pages 13–21. Geological Society of London Special Publication.

Tsukahara, H. and Ikeda, R. (1991). Crustal stress orientation pattern in the central part of Honshu, Japan: stress provinces and their origins. *Journal of the Geological Society of Japan*, 97:461–474. In Japanese.

Tsukahara, H. and Kobayashi, Y. (1991). Crustal stress in the central and western parts of Honshu, Japan. *Zisin*, 44:221–231. In Japanese.

Turcotte, D. L. and Schubert, G. (1982). *Geodynamics*. John Wiley & Sons, New York, NY.

Ukawa, M., Ishida, M., Matsumura, S., and Kasahara, K. (1984). Hypocenter determination method of the Kanto-Tokai observational network for microearthquakes. Research Notes 53, National Research Center for Disaster Prevention. In Japanese.

Waldhauser, F. and Ellsworth, W. (2000). A double-difference earthquake location algorithm: method and application to the northern Hayward fault, California. *Bulletin of the Seismological Society of America*, 90:1353–1368.

Wang, K. (2000). Stress–strain 'paradox', plate coupling, and forearc seismicity at the Cascadia and Nankai subduction zones. *Tectonophysics*, 319:321–338.

Wang, K. and He, J. (1999). Mechanics of low-stress forearcs: Nankai and Cascadia. *Journal of Geophysical Research*, 104:15191–15205.

Wentworth, C. M. and Zoback, M. D. (1989). The style of late Cenozoic deformation at the eastern front of the California Coast Ranges. *Tectonics*, 182:237–246.

Wilks, K. R. and Carter, N. L. (1990). Rheology of some continental lower crustal rocks. *Tectonophysics*, 182:57–77.

Working Group on Earthquake Probabilities (1999). Earthquake probabilities in the San Francisco Bay region: 2000–2030 — a summary of findings. Open-File Report 99-517, United States Geological Survey.

Yoshioka, S., Yabuki, T., Sagiya, T., Tada, T., and Matsu'ura, M. (1993). Interplate coupling and relative plate motion in the Tokai district, central Japan, deduced from geodetic data inversion using ABIC. *Geophysical Journal International*, 113:607–621.

Zhao, D., Mishra, O., and Sanda, R. (2002). Influence of fluids and magma on earthquakes: seismological evidence. *Physics of the Earth and Planetary Interiors*, 132:249–267.

Zhao, S. and Takemoto, S. (2000). Deformation and stress change associated with plate interaction at subduction zones: a kinematic modelling. *Geophysical Journal International*, 142:300–318.

Zoback, M. D. (2000). Strength of the San Andreas. *Nature*, 405:31–32.

Zoback, M. D. and Beroza, G. C. (1993). Evidence for near-frictionless faulting in the 1989 (M6.9) Loma Prieta, California, earthquake and its aftershocks. *Geology*, 21:181–185.

Zoback, M. D. and Harjes, H.-P. (1997). Injection-induced earthquakes and crustal stress at 9 km depth at the KTB deep drilling site. *Journal of Geophysical Research*, 102:18477–18491.

Zoback, M. D. and Healy, J. H. (1984). Friction, faulting, and in situ stress. *Annales Geophysicae*, 2:689–698.

Zoback, M. D. and Healy, J. H. (1992). In situ stress measurements to 3.5 km in the Cajon Pass scientific research borehole: implications for the mechanics of crustal faulting. *Journal of Geophysical Research*, 97:5039–5057.

Zoback, M. D. and Hickman, S. H. (1982). In situ study of the physical mechanisms controlling induced seismicity at Monticello Reservoir, South Carolina. *Journal of Geophysical Research*, 87:6959–6974.

Zoback, M. D. and Townend, J. (2001). Implications of hydrostatic fluid pressures and high crustal strength for the deformation of intraplate lithosphere. *Tectonophysics*, 336:19–30.

Zoback, M. D., Townend, J., and Grollimund, B. (2002). Steady-state failure equilibrium and deformation of intraplate lithosphere. *International Geology Review*, 44:383–401.

Zoback, M. D. and Zoback, M. L. (1991). Tectonic stress field of North America and relative plate motions. In Slemmons, D. B., Engdahl, E. R., Zoback, M. D., and Blackwell, D. D., editors, *Neotectonics of North America*, pages 339–366. Geological Society of America.

Zoback, M. D. and Zoback, M. L. (2002). State of stress in the earth's lithosphere. In Lee, W. H. K., Kanamori, H., Jennings, P. C., and Kisslinger, C., editors, *International Handbook of Earthquake and Engineering Seismology*, pages 559–568. International Association of Seismology and Physics of the Earth's Interior.

Zoback, M. D., Zoback, M. L., Mount, V. S., Suppe, J., Eaton, J. P., Healy, J. H., Oppenheimer, D., Reasenberg, P., Jones, L., Raleigh, C. B., Wong, I. G., Scotti, O., and Wentworth, C. (1987). New evidence for the state of stress on the San Andreas fault system. *Science*, 238:1105–1111.

Zoback, M. L. (1992). First and second order patterns of stress in the lithosphere: the World Stress Map Project. *Journal of Geophysical Research*, 97:11703–11711.

Zoback, M. L. et al. (1989). Global patterns of tectonic stress. *Nature*, 341:291–298.

Zoback, M. L., Jachens, R. C., and Olson, J. A. (1999). Abrupt along-strike change in tectonic style: San Andreas fault zone, San Francisco Peninsula. *Journal of Geophysical Research*, 104:10719–10742.

Zoback, M. L. and Zoback, M. D. (1980). State of stress in the conterminous United States. *Journal of Geophysical Research*, 85:6113–6156.

Zoback, M. L. and Zoback, M. D. (1989). Tectonic stress field of the conterminous United States. *Geological Society of America Memoir*, 172:523–539.